UNIVERSITY OF CALIFORNIA,
IRVINE

Aqueous Sequestration and Solid-Phase Separation of Actinyl Ions with PAMAM Dendrimers

DISSERTATION

submitted in partial satisfaction of the requirements
for the degree of

DOCTOR OF PHILOSOPHY

in Chemistry

by

Kara Elizabeth Thomas

Dissertation Committee:
Professor Athan J. Shaka, Chair
Associate Professor Mikael Nilsson
Assistant Professor Sarah Finkeldei

2020

DEDICATION

To

Nick, the love of my life and my biggest motivator.

And my family, friends, mentors and colleagues, for their support which has never wavered.

TABLE OF CONTENTS

LIST OF FIGURES

Page

LIST OF TABLES

Page

ACKNOWLEDGEMENTS

I would like to sincerely thank my co-advisors Professor Mikael Nilsson and Professor Athan J. Shaka (also the committee chair), for their time, support, and mentorship throughout the years. The opportunities I was granted as part of your laboratories led to growth I have experienced as a researcher, and skills that I will carry with me for the rest of my life.

I would like to express my gratitude for the third defense committee member, Professor Sarah Finkeldei who has risen beyond the typical role to become a trusted mentor and valued collaborator in this project. Thank you for investing your time in this work and in me.

I would like to thank Dr. Dmitry Fishman from the UC Irvine Laser Lab for training me on several instruments in the Laser Lab and lending his expertise in fluorescence and dynamic light scattering techniques, among others, to this project. Thank you for your invaluable contributions and mentorship.

I would like to thank the past and present UC Irvine reactor facility staff, including Dr. George Miller, Mr. John Keffer, Dr. Tro Babikian, and Mr. Jonathan Wallick for assistance in planning and executing experiments at the reactor.

I would like to thank Dr. David Shuh, Dr. Corwin Booth and Dr. Michael Mara for their generous support in the EXAFS proposal writing, experiment completion and data processing.

I would like to thank Timothy Connor and Jacklynn Unangst for their efforts and assistance in in synthesizing PAMAM dendrimers.

I would like to thank the members of the Nilsson Research group and the Finkeldei Research group who have been amazing colleagues and helped me immensely, personally and professionally.

Finally, I would like to thank the Science, Mathematics, and Research for Transformation (SMART) scholarship program for funding me as a graduate student for five years.

CURRICULUM VITAE

Kara Elizabeth Thomas

2015-2020	Graduate Student Researcher
	University of California, Irvine
2015-2020	SMART Scholar
	Department of Defense
2016-2018	SMART Summer Intern
	Air Force Nuclear Weapons Center
2016	Teaching Assistant
	University of California, Irvine
2015	B.S. in Chemistry, University of California, Irvine
2014, 2015	Student Intern, Contractor
	Sandia National Laboratories – New Mexico
2013-2015	Undergraduate Research Assistant
	The George Washington University
2014	Nuclear Forensics Undergraduate Scholar
	Department of Homeland Security, Domestic Nuclear Detection Office
2013-2014	Learning Assistant
	The George Washington University
2013	Nuclear Forensics Undergraduate Summer Student
	Department of Homeland Security

FIELD OF STUDY

Separation Sciences, Actinide Chemistry, Analytical Chemistry

PUBLICATIONS AND PATENTS

Thomas, K.E., Finkeldei, S.C., Nilsson, M., and Fishman, D.A. “Method for Liquid-to-Solid Phase Separation of Uranium and Uranyl Contaminant from Various Solutions.” U.S. Provisional Pat. Ser. No. 63075588, Filed 08 September 2020.

Carter, K.P., Thomas, K.E., Pope, J.A., Holmberg, R.J., Butcher, R.J., Murugesu, M. and Cahill, C.L. *Inorganic Chemistry*, 55 (5), 6902-6915, **2016**. doi: 10.1021/acs.inorgchem.6b00408.

Armijo, K.M., Johnson, J., Harrison, R.K., Thomas, K.E., Hibbs, M. and Fresquez, *Progress inPhotovoltaics: Research and Applications*, 24 (4) 507-516, **2014**. doi: 10.1002/pip.2561.

Yang, B.B., Armijo, K.M., Harrison, R.K., Thomas, K.E., Johnson, J., Taylor, J.M., Sorensen, N.R. In *2014 IEEE 40th Photovoltaic Specialist Conference (PVSC): Proceedings of the 2014 IEEE 40th Photovoltaic Specialist Conference (PVSC)*, Denver, CO, June 8-13, 2014.doi: 10.1109/PVSC.2014.6924875

ABSTRACT OF THE DISSERTATION

Aqueous Sequestration and Solid-Phase Separation of Actinyl Ions with PAMAM Dendrimers

by

Kara Elizabeth Thomas

Doctor of Philosophy in Chemistry

University of California, Irvine, 2020

Professor Athan J Shaka, Chair

Nuclear energy is a sustainable baseload power source with low life cycle carbon emissions, and no emissions during power plant operations. Research into new separatory schemes and technology to reprocess used nuclear fuel (UNF) can further improve carbon emissions and the efficiency of the nuclear fuel cycle. Improved aqueous separatory and extraction agents have the additional benefit of making the use of radionuclides safer with their ability to carefully segregate selected materials from environments such as natural bodies of water or waste streams. Prior research has focused on liquid-liquid extraction (LLE)/solvent extraction (SX) and solid-phase extraction (SPE)/ion exchange (IE) to reprocess and reclaim nuclear material, particularly the mid- and minor-actinides which contain most of the radiotoxicity of UNF. However, these types of schemes face several challenges, such as generation of secondary waste, selection or design of a ligand to separate the similar lanthanides and actinides, low adsorption and retention capacity of extracting agents, and fouling, degradation or delamination of solid support systems.

This work focuses on utilizing poly(amido amine) (PAMAM) dendrimers for improved aqueous sequestration and solid phase separation of the actinyl ions, which take

the form AnO_2^+/AnO_2^{2+}. Dendrimers are hyperbranched polymers that grow outward in numerous branching arms from a single core rather than linearly. This introduces dendritic effects, which are steric, size and chemical effects that differ from those that would be expected from a monomeric or linear form, and can positively or negatively influence metal ion binding and coordination chemistry of dendrimers. These effects also include solubility and phase variation due to the colloidal nature of PAMAM dendrimers. It is observed that PAMAM dendrimers have an enhanced affinity and capacity for precipitation/solid-phase separation when binding with actinyl ions through a combination of dendritic effects and unique coordination to the actinyl ions due to their open equatorial coordination plane available for multidentate binding. Spectroscopic and analytical techniques such as fluorescence spectroscopy (steady-state and time-resolved), UV-Vis-NIR spectroscopy, neutron activation analysis, dynamic light scattering and x-ray absorption spectroscopy are utilized to examine the coordination chemistry and the separatory efficiency of these dendrimers. Factors such as metal ion:ligand ratio, pH, oxidation state, and absolution concentration of the actinyl ion are explored to improve separatory efficiency if the process were to be scaled up. Efficient aqueous coextraction of the actinyl ions is expected to make the use of radionuclides safer, and help close the nuclear fuel cycle by reusing these actinyl ions for materials such as mixed oxide fuel (MOX).

1. INTRODUCTION

Nuclear Energy and the Nuclear Fuel Cycle

Global energy consumption has steadily increased by an average of 1.1% each year for the past ten years, with a total of 583.9 exajoules consumed in 2019 alone.[1] As the world population increases, global energy demand will increase. Nuclear power plants can provide substantial base load power generation, which is continuous power supplied independent of climate or the time of day, with zero emissions during operation and low life cycle carbon emissions .[2] Despite decommissioning of older reactors, new reactors are still being connected to the grid. In 2018, 5 new reactors were added, for a total of 450 operating reactors and 55 under construction worldwide.[3] Countries needing to reduce pollution while maintaining energy efficient, reliable power generation have revived global interest and discussion about nuclear power. China, for example, had a growth of 22.75% in nuclear energy production in 2019 from 47 total reactors.[4] As of July 2020, China had 51 nuclear reactors projected to be on-line by the end of the year, and 17 more in production to replace high carbon emission coal plants.[5]

However, the generation of used nuclear fuel (UNF) has been a strong deterrent in widespread acceptance of nuclear energy. Since commercial nuclear power plants began operating, 83,978 metric tons of UNF has been produced in the United States alone, with 2,000 to 2,300 additional metric tons being produced each year.[6] Plans for large-scale, permanent nuclear waste geological repositories, such as Yucca Mountain in the United States, have not materialized due to high cost and public/political opposition, including litigation.[7] Without other options, UNF in numerous countries is often stored at the site of

the power plant where the UNF is generated, usually under security in storage pools or in steel/concrete containers, so-called dry cask storage.[8] Environmental and nuclear proliferation concerns from the public about the storage and maintenance of UNF have also restricted the growth and acceptance of nuclear energy. “Closing the fuel cycle” involves a responsible way to either utilize or store UNF, which in turn will increase the efficiency of the cycle, reduce the carbon emissions of parts of the cycle and decrease the environmental and security hazards of UNF.

Reprocessing UNF has great potential for reducing the radiotoxicity of UNF, reducing heat load in UNF repositories, reusing select nuclear material, and significantly reducing the volume of waste that must be permanently stored.[9] In most commercial reactors, a “once-through” fuel cycle is maintained. Fuel is considered “spent” or “used” when it can no longer efficiently maintain the fission chain reaction of uranium-235. The term “spent” is somewhat of a misnomer because 95.5% of UNF, on average is uranium-238 which can be re-enriched or reused in a few ways. The remaining material is composed of plutonium (0.9%), fission products (3%) and minor actinides (0.1%).[9,10]

Limited commercial fuel reprocessing in countries like France, Japan, India, Russia, and the United Kingdom uses solvent extraction to reclaim uranium and plutonium in a well-developed method called plutonium uranium reduction extraction (PUREX).[9] Solvent extraction is an effective technique to separate a solute between two immiscible liquids, often organic and aqueous solvents.[11] In PUREX, an organic solvent containing a lipophilic, organophosphoric compound called tributyl phosphate (TBP) is contacted with uranium or plutonium dissolved in nitric acid. The interaction of TBP with the metal ion forms a more

hydrophobic complex and changes the solubility of the ion to transport it from the aqueous to the organic phase. Uranium and plutonium can be further separated or fabricated into mixed oxide (MOX) fuel, which can be utilized directly in certain types of reactors, such as a pressurized water reactor (PWR) or a fast reactor (FR) to help close the fuel cycle.[12] A process for co-extracting multiple actinides for MOX like PUREX could further increase the macroscopic efficiency of the nuclear fuel cycle, as a large portion of energy consumption in the nuclear fuel cycle takes place during the enrichment of uranium.[12]

In addition to maximizing energy efficiency, minimizing the carbon emissions in the life cycle of the fuel cycle is a major goal. A large portion of carbon emissions come from the mining and milling of terrestrial uranium ore prior to enrichment and fabrication.[12] Although the concentration of uranium in water sources is low (approximately 3.3 ppb), the amount of uranium in the oceans, a total of 4 billion tons, eclipses that of terrestrial sources, such as uranium ore.[13,14] Aqueous sequestration to aggregate and separate the uranium and other actinides, along with other physical collection forms, has been proposed as an alternative to mining as a nearly inexhaustible source of materials for nuclear fuel, considering the energy density.[15,16] Any extracting agent that is efficient in a close-to-neutral environment is also beneficial for environmental remediation in the case of some release of nuclear material into an aqueous environment.

Although nuclear power is already an efficient and low emission energy source, simpler and less energy intensive processes to obtain and reuse the actinides necessary for fuel can improve the energy efficiency and lower carbon emissions in the nuclear fuel cycle (including the potential for a close nuclear fuel cycle) and the improve the safety of UNF. In

addition, effective sequestration of nuclear material in aqueous environments can enable remediation of undesirable lanthanide and/or actinide contamination. A simple, selective, and effective separatory system continues to be pursued in the nuclear field of research for these reasons.

Separatory Techniques

A new extracting agent or extraction system must represent some important improvement in one or more areas compared to prior systems. Solvent extraction (SX), also known as liquid-liquid extraction (LLE), is one of the main methods for uranium separation from lanthanides and other actinides. This technique exploits the solubility of uranium in immiscible solutions, usually an aqueous and organic phase. By the time uranium and other actinides reach a separatory phase, whether it is in mining, reprocessing, or the environment, they typically exist in an acidic aqueous medium in the dioxo-cation actinyl (AnO_2^+ / AnO_2^{2+}) form.[17] In processes like PUREX and other reprocessing or mining flowsheets, ligands are employed that induce hydrophobicity of the uranyl ion, allowing it to be selectively extracted in an organic phase.[18,19] A scrubbing process removes impurities from the organic phase, by utilizing selective ligands and contacting with an aqueous phase, to purify the uranyl ion. Then, the uranium is usually contacted with an aqueous phase to further isolate and reconstitute it in a concentrated form, which is called the stripping process.[20] Alternative methods like the uranium extraction (UREX) process utilize "hold-back" reagents to selectively reduce or otherwise retain neptunium, plutonium and other ions in the aqueous phase for more efficient extraction of uranium, followed by analogous scrubbing and stripping steps for purification.[21]

The challenges of solvent extraction have been well documented despite many improvements in the field. The first is finding an appropriately selective ligand. Hard-Soft Acid-Base theory (HSAB) dictates that all lanthanides and actinides are qualitatively "hard" acids because they typically have reduced atomic radii and high oxidation states. Therefore, selectively isolating the uranyl ion from other lanthanides, actinides, and actinyls relies on small differences in the structure of *4f* and *5f* elements. The "lanthanide contraction" makes the *4f* trivalent lanthanides slightly harder acids than trivalent actinides or actinyls because the *5s* and *5p* orbitals are poorly shielded from the nucleus by the *4f* orbitals, resulting in smaller atomic radii than expected. Therefore, bases like oxygen donors are used as ligands for lanthanides whereas "softer" nitrogen and sulfur donors can be used for actinides and actinyls.[22,23,24] This is still a non-exact science and extracting reagents often coextract similar ions which need to be separated in further steps. The aforementioned extraction, stripping and scrubbing steps can enhance the efficiency of uranium separation by utilizing different solvents, ligands and redox chemistry. However, this can generate nontrivial amounts of secondary hazardous and/or radioactive waste at each step.[25,26] This includes some ligands, especially in the organic phase, that can be toxic and difficult to strip and reuse, especially under the ionizing radiation fields present in nuclear waste from minor actinides and fission products.[27] Finally, although improvements have been made, extractants still have too low of an adsorption and retention capacity to effectively reclaim low concentrations of uranium from the environment or waste streams.[28]

Other uranium separatory processes utilize solid support systems, such as membranes and resins. These solid phase extraction (SPE) techniques usually employ the

principle of ion exchange (IX). IX is a process in which an immobile, solid phase with an attached or adsorbed functional group and dissolved ions are exchanged for other targeted ions in solution. The functional group can be any number of ligands that determine selectivity for uranium, as discussed with solvent extraction, but immobilization on a solid support system can offer advantages. The extractant does not have to be dissolved in the solvent, so solubility issues and generation of hazardous ligand-containing waste are mitigated. SPE can be designed to have multiple functional groups on a given particle of resin or certain surface area of membrane, which can allow for the formation of polyatomic complexes. SPE also has the capacity for reuse because the resin or membrane can usually be regenerated by washing with acid, base, or an ionic solution like sodium chloride for reuse, though this does introduce the same concerns about the generation of secondary waste.[29] Implementing different cycles of waste streams and washing solvents can be an effective substitute for multiple solvent extraction steps. In addition, modifying porosity/pore size, density, bead size, crosslinking, thickness or permeability of the membrane or resin can offer other methods of physical separation in addition to chemical separation.[16,30] The variety of solid supports, including potential modifications, has made scientists believe SPE is the next frontier for radiochemical separations.[30]

These techniques can be effective, but not necessarily selective. Anion resins are typically preferred over cation resins for their uranium selectivity, whereas cationic resins tend to adsorb many types of metal cations, including lanthanides and other actinides.[28] However, the waste stream for anionic resins usually must have a delicate pH balance to form mostly anionic uranyl hydroxides or other uranium species, yet not high enough to

cause precipitation of the uranium, which occurs typically over pH 8.[31] Increased selectivity must be balanced with favorable kinetics of both adsorption and desorption.[29] While flow rate over the solid support can be adjusted, if the kinetics are slow, many cycles of waste and washing may be needed for effective removal and reuse, while generating more secondary waste. In addition, the solid support has the additional requirement of durability. This means resistance to chemical fouling (undesirable accumulation of ions, organic residue, bacteria, algae or other aquatic organisms), degradation of the solid support (especially under pH extremes), or delamination of the functional groups.[31]

Dendrimers

Dendrimers are hyperbranched, highly monodisperse polymers synthesized from a core with repeating monomeric branches extending from the core. Dendrimers are made of three main parts: a core, the branches, and the terminal groups, which do not have to be identical (**Figure 1**). Each functional group can be carefully selected to have specific solubility, stability or reactivity, binding capabilities, geometry, and intermolecular interactions. Every diverging branch point is considered a "generation", and dendrimers are often named with the prefix G*X*, where *X* denotes the generation and a ".5" can be added to denote termination at a different branch point, if applicable. The generation or size of the dendrimer can also contribute unique properties to the dendrimers.

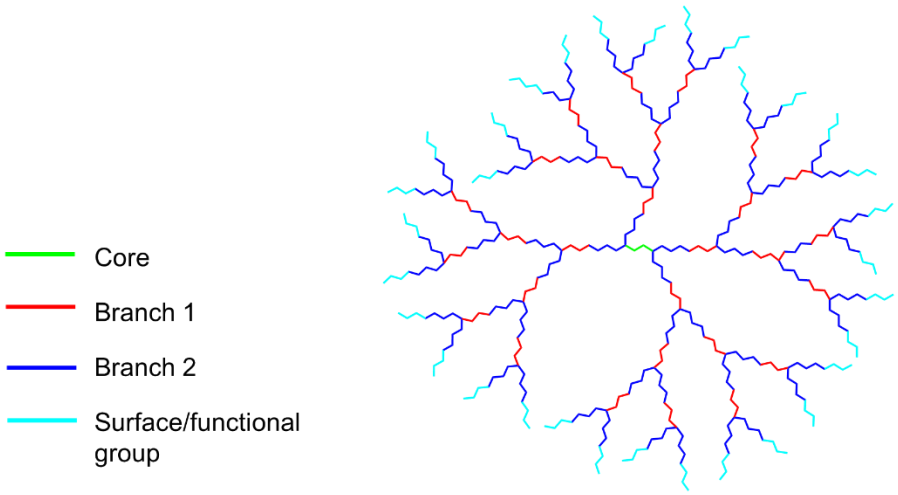

Figure 1. The three generic parts of a dendrimer (branches are typically considered one part).

Dendrimers are known for having multiple binding sites for metal ions, which can be customized with different branches, terminal groups, and size/generation. The benefit of using dendrimers for separatory applications is the presence of "dendritic effects". This is an umbrella term for any unexpected physiochemical behavior which occurs because of the size, generation, and structure of the dendrimer. The steric effects, solubility, shape, and chemistry of functional groups in dendrimers can, and often does, vary from that in a monomeric or linear polymeric form of the branches.[32,33] Relying on the small size differences or chemical differences in the hardness or softness of metal ions for separatory purposes can be challenging, but enhancement of these effects with dendritic effects allow for an extra layer of selectivity. One study using crown ether-functionalized dendrimers for LLE termed these dendritic effects "positive" or "negative" based on whether they enhanced or hindered extraction.[33]

It has been demonstrated that certain dendrimers, like polyamidoamine (PAMAM, see **Figure 2**) dendrimers, coordinate metal ions exceptionally well.

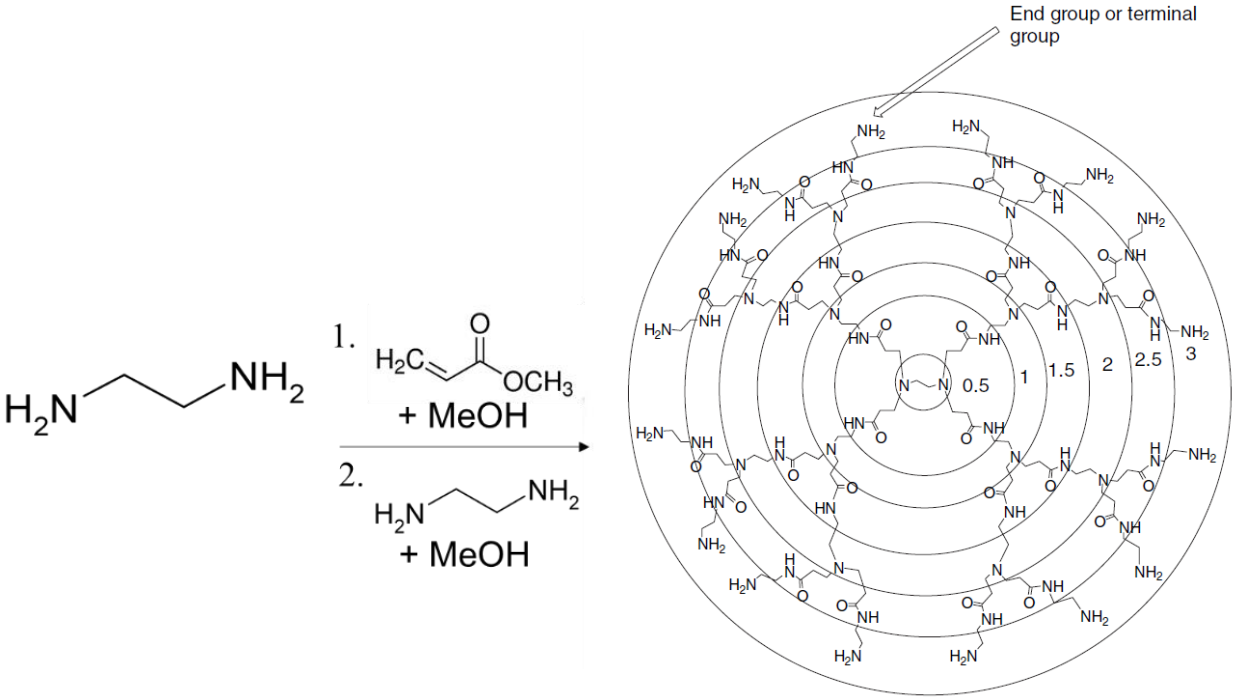

Figure 2. General form of a PAMAM dendrimer. The right part of the figure is replicated from **Reference 34**.

Therefore, they have been proposed for all types of metal ion sorption and extraction, including wastewater remediation and filtration, among many other applications.[35,36,37,38,39] Different types of functionalized solid support systems have been proposed to enhance the separatory abilities of dendrimers, such as polymer-enhanced ultrafiltration (PEUF) membranes,[40,41,42] hollow fiber membranes (HFMs),[43] functionalized magnetic nanoparticles,[44,45] resins,[46,47,48,49] polymer hydrogels,[50] functionalized silica gels,[51] and supported liquid membranes (SLMs).[52] Actinides, in the trivalent form, have been shown to undergo effective complexation with diglycoamic acid/diglycoamide (DGA)- or carbamoylmethylphosphine oxide (CMPO)-based dendrimers, and in the actinyl form with

poly(amido) amine (PAMAM)- or poly(propyleneimine) (PPI)-based dendrimers, and separatory processes can be demonstrated using processes utilizing various solid supports.[42,44,46,49,52,53] In several studies, it has been noted that dendrimers with nitrogen donor groups have unusually high binding capacity for the uranyl ion compared to other metal ions including lanthanides or other fission products, although the exact origin of this phenomenon is unknown.[42,48,54]

Metal ions can coordinate at interior or exterior binding sites on dendrimers, but the exact coordination chemistry is less important as the metal loading increases and nearly all sites become binding sites. The addition of more metal ions enhances the important separatory functions of dendrimers by increasing the weight and structure of the complex, which can affect the known soft colloidal properties of dendrimers.[55,56,57,58] Additionally, with increasing generation, dendrimers intrinsically become more globular and compact as the branches begin to interact.[32] They have also been simulated and demonstrated to aggregate through interpenetration of multiple dendrimers, and to have the ability to undergo self-assembly utilizing transition metals, stimulated by a number of different methods.[59,60] The combination of increased mass of added metal ions, increased structure/rigidity from metal ion coordination, and the possibility for supramolecular interactions and subsequent aggregation makes it possible that the soft colloidal nature of the dendrimer could transform into a much denser, extended structure that can precipitate and suspend in solution. Being that some dendrimers are especially selective for certain ions, such as the uranyl ion, a liquid-to-solid separation that requires only the dendrimer, the metal ion, controlled pH, and centrifugation is possible. The need for solid support

systems, such as membranes, ultrafiltration apparatuses, functionalized resins or other aforementioned elements can be eliminated.

This work focuses on addressing several major goals of nuclear energy: maximizing the energy efficiency, minimizing carbon emissions, closing the fuel cycle, and increasing efficacy of decontamination and reclamation of radionuclides by examining PAMAM dendrimers as extracting agents for lanthanides and actinyl ions. Dendrimers have excellent potential for addressing all three goals through aqueous sequestration of uranium and other materials for fuel and in reprocessing applications to generate MOX fuels and close the fuel cycle. Environmental remediation is even possible with separation of certain ions in environmental aqueous locations. The ability to customize different parts of the dendrimer for different properties including selectivity for certain metal ions, solubility, and binding capacity allows for specialized design to target elements key to a closed nuclear fuel cycle and environmental reclamation, like the actinides. The potential for second phase or solid-phase separation due to the colloidal nature and dendritic effects of dendrimers add an additional interesting feature with the potential for circumventing many of the challenges of LLE/SX and SPE/IX.

Chapter 2: Scope and Aims of the Dissertation

This work will examine the coordination chemistry, selectivity, solubility binding and separatory capacity of PAMAM dendrimer complexes with metal ions of particular interest to the nuclear fuel cycle, namely uranium, neodymium (as a representative for the lanthanides), and neptunium. To investigate these important properties, complementary analytical tools will be used, including fluorescence spectroscopy, UV-Vis spectroscopy, x-ray absorption spectroscopy, dynamic light scattering, and neutron activation analysis. The following objectives were addressed with these techniques:

1. Examining the coordination chemistry of PAMAM dendrimers including binding capacity and formation constants using steady-state fluorescence spectroscopy.
2. Examining the nature of uranyl-PAMAM dendrimer binding, specifically denticity and geometry, using time-resolved laser-induced fluorescence, and x-ray absorption spectroscopy.
3. Proposing a theory for the formation of precipitate using neutron activation analysis and dynamic light scattering.
4. Investigating effects of selected factors on formation of precipitate using neutron activation analysis.
5. Examining the selectivity of PAMAM dendrimers using steady-state fluorescence spectroscopy and UV-Visible spectroscopy.

The first four goals specifically focus on uranyl-PAMAM dendrimer complexes to determine the origin of enhanced binding and precipitation of these complexes, whereas

the final goal constitutes a comparative study of other metal ion-PAMAM dendrimer complexes to further understand the coordination chemistry and selectivity of the PAMAM dendrimer.

Chapter 3: Background and Theory

3.1. Fluorescence Spectroscopy and Quenching

Photoluminescence is the phenomenon of emission of light from a substance due to relaxation of electrons from electronically excited states. Fluorescence, one of two types of luminescence, results from spin-allowed transitions. Phosphorescence, the other type of luminescence, encompasses spin-forbidden transitions (*i.e.* triplet to singlet transitions) which are possible by undergoing intersystem crossing. The average time a fluorescent species, also called a fluorophore, remains in an excited state is called the fluorescence lifetime (τ). Fluorescence occurs quickly, from 10^{-12} to 10^{-6} seconds. Fluorophores that undergo phosphorescence have a longer lifetime of the excited state, from 10^{-6} to 10^{-3} seconds, because of the kinetically unfavorable change in electron spin during relaxation. An excited state can lose energy in forms such as translational movement, vibrational and rotational motion, or heat during decay. The remaining energy emitted as a photon is less than the energy of the absorbed photon. Therefore, the fluorescence emission spectrum is often red shifted in comparison with the absorption spectrum. The quantified spectral shift is called the Stokes shift.[61,62]

Quantum yield (Φ) is the ratio of photons emitted by luminescence to photons absorbed through luminescence. Fluorescence intensity (I) is a metric in arbitrary units that is proportional to the amount of light emitted from a substance following absorption of light for a given experimental setup. It is also proportional to concentration. Fluorescence intensity can be affected by the structure of a molecule or the environment of a molecule,

including functional groups, rigidity of the molecule, polarity of solvents, pH of solutions, temperature, viscosity, turbidity, temperature, and concentration.[61,62]

A fluorophore can also undergo molecular interactions that decrease the photon emission, and hence the measured signal, from a sample, a phenomenon known as "quenching". There are two types of quenching: static and dynamic quenching. Static quenching occurs when a nonfluorescent complex is formed between the fluorescent molecule and another species, called a quencher. Dynamic quenching, also known as collisional quenching, occurs when an excited fluorophore interacts with the quencher and undergoes nonradiative decay. The fluorophore and quencher usually must be in close proximity in order to interact via energy transfer, charge transfer, or electron transfer which are all slightly different mechanisms that result in radiationless deactivation.[63] Dynamic quenching typically results in a shorter fluorescence lifetime of the fluorophore because additional pathways of nonradiative decay are present. Taking these factors into consideration, static and dynamic quenching can give insight into the coordination chemistry and electron-level interactions between two species.

3.1.1 Fluorescence of PAMAM Dendrimers

PAMAM dendrimers are observed to have blue fluorescence in the region 430-460 nm with an excitation wavelength of approximately 350 nm. PAMAM dendrimers are large organic molecules without traditional fluorophores, so the functional groups acting as fluorophores have only been determined through careful, deductive experiments. The exact PAMAM dendrimer electronic states involved in fluorescence is therefore undetermined and may in fact not be from transitions solely in the electronic states of the dendrimer. Any

1→ 2 nitrogen-branched dendrimer with triethylamine (TEA) as a backbone exhibits fluorescence regardless of the end groups or linking molecules, which led to the hypothesis that the tertiary amine groups act as fluorophores.[64] TEA also fluoresces at 440 to 460 nm, which is approximately the same as PAMAM dendrimers.

Studying the difference between TEA and 1→2 N-branched dendrimers in oxygen-rich atmospheres, air, and nitrogen atmospheres has led to several conclusions.[65] The unexpected fluorescence at the tertiary sites is apparently only possible through oxidation, as fluorescence intensity from PAMAM dendrimers under nitrogen atmosphere is much lower than those exposed to air, oxygen-rich atmospheres, or oxidizing molecules (such as ammonium persulfate). Enhancement in fluorescence yield between TEA and the tertiary amines in dendrimers appears to be due to crowding in the interior. This is proposed to encapsulate oxygen more efficiently in the interior and restrict rotational and translational movement, leaving the majority of deexcitation to occur by electronic transitions.

Once oxygen is positioned in the interior of the dendrimer, fluorescence has been proposed to occur through the formation of short-lived exciplex or radical species. The lone pair of electrons on a nitrogen atom or lone pairs on the oxygen can become electronically excited and bind to the other structure which exists in the ground state, termed an exciplex.[64,65,66] The bound exciplex undergoes charge/electron transfer which can lead to a larger Stokes shift, if radiationless decay occurs, and band broadening of the amine fluorescence, depending on the energy levels of each monomer involved in the exciplex.

Fluorescence of a short-lived tertiary amine-oxygen radical could produce a similar effect. The absorption of a peroxyl radical formed from a TEA radical in an oxygen-

saturated solution was demonstrated to be red-shifted from the absorption of the TEA radical, to a wavelength of approximately 380 nm. Absorption and rapid relaxation of a tertiary amine-oxygen radical could therefore produce the blue fluorescence that is observed in PAMAM dendrimers.[64] External oxygen is not considered essential for either an exciplex or a radical to form, as the dendrimers have oxygen atoms as part of ester groups on their flexible branches, which can interact with tertiary amines from other branches. This can be verified by a weak fluorescence present even in dendrimers in nitrogen-bubbled atmospheres.

3.1.2 Luminescence of the Lanthanides and Actinides

In general, lanthanides are most stable in their trivalent cation form in aqueous solutions, and have unique spectroscopic properties. Their 4*f* electrons can undergo 4*f*-4*f* (weak, electric dipole forbidden) or $4f^n$-$4f^{n-1}(n-1)d$ transitions or electron transfer transitions, usually to ligands or the solvent.[67,68] The environment around the lanthanide, including factors such as pH, complexed ligands, and the type of solvent, can also impact or change the luminescence spectra of lanthanides by inducing ligand-field splitting. Ligand-field sublevels for the lanthanides in various crystal fields have been meticulously identified and can number in the thousands.[67] The ligand-field splitting phenomenon can alter the energy of the sublevels involved in the transition, which can change the Stokes shift. Depending on the nature of the sublevels, some transitions can also be nonradiative, which lowers fluorescence yield, or produce very broad bands, making spectral analysis challenging.

The photoluminescence of the lanthanides in aqueous media is therefore very complex, involving spin and parity-allowed $f \leftrightarrow d$ transitions, $f \leftrightarrow f$ Laporte forbidden transitions and charge transfer peaks. Some lanthanides fluoresce relatively strongly, some weakly, and some not at all depending on the types of transitions involved. While the *f-d* and metal-to-ligand charge transfer bands are broad and intense, the *f-f* transitions are typically narrow, very weak, and have low molar absorption coefficients. They are weak because they are Laporte (parity) forbidden transitions, and sometimes are spin forbidden as well. But, the 4*f* electrons are shielded from external factors in the environment by the filled 5*s* and 5*p* electrons, which is the reason the spectral bands of the *f-f* transitions are so narrow and usually not shifted or broadened by the environment.[69] This is important for quantitative spectral analysis of the lanthanides despite the low fluorescence yield of these bands.

However, certain lanthanides have been observed to have *f-f* "hypersensitive" transitions, whose intensity can be significantly enhanced by the environment, including ligands or the solvent, without shifting of the spectra or broadening of the band. Judd and Ofelt individually theorized this phenomenon as either being due to induced asymmetry of the crystal fields of lanthanides or enhancement of pseudo-quadrupole transitions in the 4*f* shell due to dielectric inhomogeneities in the environment, now known as the Judd-Ofelt theory.[70,71] Therefore, experimentalists often focus on enhancement of the important hypersensitive transitions for quantitative analysis by carefully designing the lanthanide media or ligands to promote asymmetry and transfer electrons for higher fluorescence yield. Because these transitions end up dominating the lanthanide luminescence, those that

do luminesce tend to have longer fluorescence lifetimes due to the forbidden nature of their $f \leftrightarrow f$ transitions.

Luminescence of the actinides is both less well known and less cohesive than that of the lanthanides. The radioactive nature of the actinides often precludes in-depth study, especially of the heavier actinides that exist briefly and in small quantities. The remaining actinides can exist in various oxidation states and sometimes in polyatomic ionic forms, depending on the environmental conditions, normally leading to richer and more complex spectra than the more uniform lanthanides.[72]

Overall, a few trends can be noted. The trivalent form of americium, curium and other actinides are similar to the trivalent lanthanides and are often considered the chemical analogs of the 4*f* elements. For the same reasons as previously discussed within the Judd-Ofelt theory, they also have hypersensitive *f-f* transitions. In addition, the 5*f* electrons are less shielded than the 4*f* electrons by outer shell electrons, so the actinides have spin orbit coupling parameters and ligand field effects that are approximately twice as large.[73] This makes them substantially more susceptible to changes in the environment. The increased spin-orbit and electrostatic interactions relax Hund's rule and Russell-Saunders coupling which causes both ground state mixing and excited electronic state mixing for the heavier 5*f* ions. Therefore, the peaks are often broader than their 4*f* analogs.

The actinyl form of uranium, neptunium, and americium (AnO_2^+/AnO_2^{2+}) have different luminescence qualities from each other despite having very similar chemical forms. This is because the uranyl ion, which has been well studied and characterized, has a $5f^0$ electronic configuration which is not representative of the other actinyls. In general, the

$5f^n$ actinyl ions have $5f$-$5f$ transitions and transitions resulting from excitation and relaxation of an electron from a molecular orbital of primarily oxo ligand character to a molecular orbital of metal character, termed ligand-to-metal charge-transfer (LMCT).[74] Therefore, luminescence of the actinyls including the excitation spectrum can theoretically be used to probe both the local environment (equatorial coordination) and the nature of the An-O bonds.

3.1.2.1 Uranyl (VI) Luminescence

The luminescence of the uranyl ion is the most studied of the actinides and famous because of its green phosphorescence, which was utilized as a coloring agent and glow-in-the-dark novelty in glass around the time of the Great Depression. The long-lived, high-intensity luminescence results from transitions between the molecular orbitals resulting from mixing of the $5f$ and $6d$ orbitals of uranium with the $2p$ orbitals of oxygen. The highest occupied molecular orbitals (HOMOs) are predominantly of $2p$ oxo character, while the lowest unoccupied molecular orbitals (LUMOs) are non-bonding $5f$ orbitals.[75,76]

Therefore, the major excitation band for the uranyl ion is an LMCT band. Intersystem crossing to a triplet state of the uranyl (VI) ion leads to several characteristic peaks from long-lived phosphorescence ($<10^{-6}$-10^{-3} seconds) upon emission to the ground state.[75] Typically, in an aqueous medium, there are four peaks between 480 nm – 580 nm (**Figure 3**).

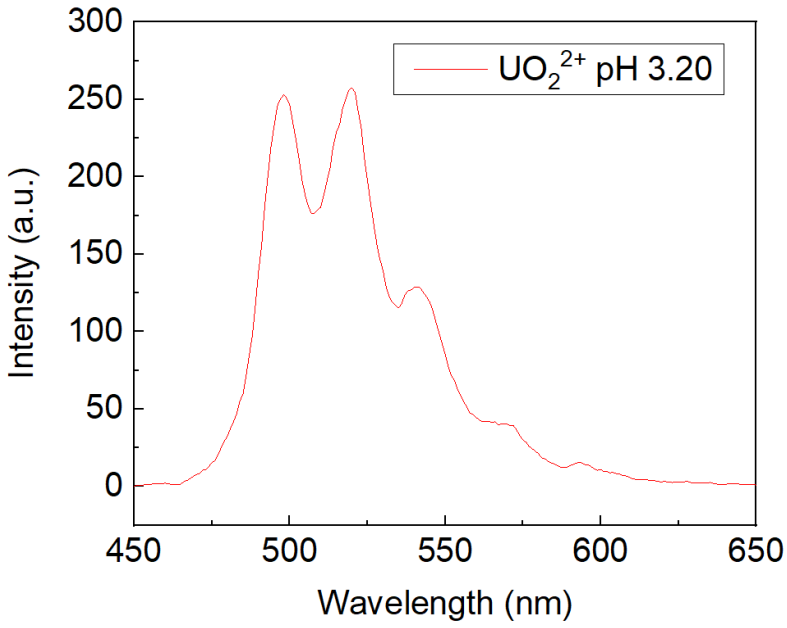

Figure 3. Phosphorescence of the uranyl ion in aqueous medium.

Two important features can be noted from the spectrum: the energy of the highest energy peak and the spacing between that and the next highest energy peak. These show the energy gap between the HOMO and the LUMO and the Raman active total symmetric stretching frequency, respectively. Overall, this helps to characterize the uranium-oxo bonds. Naturally, a change in pH or the ligand environment can change the appearance of the band by introducing new species that stabilize different excited electronic states, thereby shifting or broadening the peaks, or by causing a change in the oxidation state which can completely change the electronic structure and associated transitions. This makes it challenging to analyze uranyl luminescence directly except with careful deconvolution of the spectra and accounting for all experimental parameters that could alter the luminescence.

3.1.3. The Stern-Volmer Relationship

LMCT bands or other non-hypersensitive peaks can be difficult to use as probes of the immediate environment. As previously discussed, emission not associated with hypersensitive transitions in the lanthanides and actinides can be significantly altered by the environment beyond a change in the fluorescence intensity. Speciation and oxidation/reduction of the metal can change the electronic sublevels and transitions associated with deexcitation, and change the energy and broadness of the peaks. Additionally, some lanthanides and actinides do not luminesce. To bypass these challenges, alternative methods to probe the interaction of metals with ligands and the environment can be utilized.

In lanthanides or actinides with hypersensitive transitions, the characteristic peak and the shifted or "split" peak that appears when a complex is formed can be monitored and quantified with absorption or fluorescence spectroscopy to determine properties such as the denticity of the ligand, the binding sites and the stability constant(s).[68] This is not as straightforward with complex fluorescence, or if the complex is nonfluorescent. One of the alternative analytical techniques invokes the principles of fluorescence quenching to examine the complexation of metal ions with ligands. Several processes, shown in **Table 1**, occur in the process of a molecule fluorescing.

Table 1. Generalized processes involved in fluorescence. Note: *F* refers to a fluorophore and *Q* refers to a quenching agent.

Process	Equation	Rate of Process
Photoexcitation/Absorption	$F + h\nu \rightarrow F^*$	$k_{abs}[F]$
Fluorescence/Phosphorescence	$F^* \rightarrow F + h\nu$	$k_f[F^*]$
Nonradiative Decay	$F^* \rightarrow F$	$k_{nr}[F^*]$
Intermolecular Quenching	$F^* + Q \rightarrow F + Q$ $F^* + Q \rightarrow F + Q^*$	$k_q[F^*][Q]$

A steady-state approximation can be made assuming that the number of excited molecules is small at any given time (usually the case to avoid experimental issues such as the inner-filter effect).[61,77] Therefore, if [F] remains roughly constant, the small change in excited molecules can be approximated as:

$$-\frac{\delta[M^*]}{\delta t} = k_f[F^*] + k_{nr}[F^*] + k_q[F^*][Q] - k_{abs}[F] = 0 \quad (1)$$

Rearranging the equation, the following is obtained:

$$[F^*] = \frac{k_{abs}[F]}{k_f + k_{nr} + k_q[Q]} \quad (2)$$

The fluorescence quantum yield is:

$$\phi = \frac{number\ of\ photons\ emitted}{number\ of\ photons\ absorbed} = \frac{rate\ of\ emission}{rate\ of\ absorption} = \frac{k_f[F^*]}{k_{abs}[F]} \quad (3)$$

$$\phi = \frac{k_f(k_{abs}[F])}{k_{abs}[F](k_f + k_{nr} + k_q[Q])} = \frac{k_f}{k_f + k_{nr} + k_q[Q]} \quad (4)$$

Now, if there are no quenching molecules, the quantum yield can be defined as:

$$\phi_0 = \frac{k_f}{k_f + k_{nr}} \quad (5)$$

The ratio of the quenched and unquenched quantum yield, which is proportional to the ratio of quenched and unquenched molecules is therefore:

$$\frac{I_0}{I} \propto \frac{\phi_0}{\phi} = \frac{k_f(k_f+k_{nr}+k_q[Q])}{k_f(k_f+k_{nr})} = \frac{k_f+k_{nr}+k_q[Q]}{k_f+k_{nr}} = \frac{k_f+k_{nr}}{k_f+k_{nr}} + \frac{k_q[Q]}{k_f+k_{nr}} \quad (6)$$

$$\frac{I_0}{I} \propto \frac{\phi_0}{\phi} = 1 + \frac{1}{k_f+k_{nr}} k_q[Q] \quad (7)$$

The fluorescence lifetime of the fluorophore is equivalent to the inverse of the rate of the sum of the radiative and nonradiative rate of decay:

$$\tau = \frac{1}{k_f+k_{nr}} \quad (8)$$

Therefore:

$$\frac{I_0}{I} \propto \frac{\phi_0}{\phi} = 1 + \tau k_q[Q] \quad (9)$$

The lifetime and the rate of quenching can be grouped into the Stern-Volmer constant (K_{SV}) to produce the Stern-Volmer relationship, if the lifetime of the fluorophore remains constant:

$$\frac{I_0}{I} = 1 + K_{SV}[Q] \quad (10)$$

The Stern-Volmer constant is analogous to a binding constant as long as collisional/dynamic quenching is negligible. Stern-Volmer plot of $I_0/I - 1$ versus $[Q]$ for a given complex can therefore give the overall binding constant of the complex, provided the plot is linear. However, it must be noted that the Stern-Volmer plot can be linear whether there is static quenching or dynamic quenching. Comparing the ratio between the unquenched and quenched lifetime can distinguish the difference between static and dynamic quenching using the following equation:

$$\frac{\tau_0}{\tau} = 1 + \tau_0 k_q[Q] \quad (11)$$

Static quenching does not alter the lifetime ($\tau_0 = \tau$), so a graph of $\tau_0/\tau - 1$ versus [Q] will have a slope of zero. Normally, dynamic quenching decreases the lifetime of the fluorophore, so the same plot will have a positive, linear slope.[63]

For PAMAM dendrimer complexes, the luminescence of the metal ion can be complex, unpredictable (depending on the environment), or nonexistent for the reasons previously described. However, the PAMAM dendrimer fluorescence is not affected by the coordination of metal ions. Despite the remaining uncertainty over the exact origin of the fluorescence, two broad excitation peaks and one broad emission peak are characteristic of PAMAM dendrimers. Based on what is known about the fluorescence of the dendrimer, any interactions that disrupt the interaction between oxygen and the dendrimer should ideally revert the amines back to their nonfluorescent state. Complexation with metal ions can therefore quench the fluorescence in a measurable way, a valid alternative to the reverse scenario of measuring the change in the metal ion luminescence.

3.1.4. Steady-State and Time-Resolved Fluorescence (TRF) Spectroscopy

Adding in a third dimension of time to produce time-resolved fluorescence (TRF) spectra is invaluable for supplementing and expanding on information collected from steady-state fluorescence spectra. TRF and steady-state fluorescence are not mutually exclusive, and with careful experimental design, both can be used for complementary analysis of fluorophores. The major difference between steady-state and any type of TRF spectroscopy is that in the former excitation occurs continuously and concurrently with the emission measurement, whereas time-resolved measurements utilize staggered excitation pulses, which allows the fluorescence to be measured as a function of time.

For example, time-correlated single photon counting (TCSPC), one of the most common forms of TRF, relies on the difference in time between an initial light pulse, usually at a single wavelength from a tuned laser or monochromatic filter, and the detection of an emitted photon.[78] Naturally, because each fluorophore molecule takes a statistically different amount of time to deexcite, the spectrum of TRF is actually a histogram of times of photon deexcitation registered by the detector. This can be represented as a two-dimensional graph if only one emission wavelength is selected or as a three-dimensional graph if it is collected over a range of wavelengths. The lifetime is defined as inversely proportional to the overall rate of deexcitation (Γ), which is inherently comprised of radiative and nonradiative decay:

$$\tau = \frac{1}{\Gamma} = \frac{1}{k_f + k_{nr}} \tag{12}$$

The nonradiative rate term can also be expanded to include the rate of quenching, internal conversion, intersystem crossing, and other processes that contribute to the loss of energy of the photon emitted through fluorescence.[61] Although the lifetime is considered the average time the fluorophore exists in an excited state, because it is inversely proportional to the rate of decay it is actually the time at which the intensity has decreased by 1/e of the initial intensity at t=0:

$$\frac{I}{I_0} = e^{-t/\tau} \tag{13}$$

If there are multiple fluorophores, multiple energy transfer mechanisms, different chemical environments, or other inhomogeneities that lead to populations with different lifetimes, multiple additive exponential terms with different lifetimes may exist. This technique can

be used on very short-lived fluorophores (nano- to picosecond lifetimes) depending on how quickly the light source can pulse. For molecules with long lifetimes, care must be taken in the spacing between excitation pulses to allow the molecule to fully de-excite for an accurate time distribution before the next pulse arrives.

The addition of lifetime measurements allows for two important enhancements in comparison with steady state analysis, besides the inherent ability to calculate the fluorescence lifetime. The first is the ability to deconvolute complex spectra, especially those with overlapping or unidentified fluorescence bands. While this can be done with just steady-state measurements, the difference in lifetime between populations adds an additional metric for discrimination due to differences in electronic configuration and subsequent decay pathways in fluorophores. The second benefit was previously discussed, which is the use of the lifetime-dependent Stern-Volmer relationship to determine the exact nature of quenching of the fluorophore, if any: static, dynamic or a mixture of both.

3.2 Neutron Activation Analysis (NAA)

NAA is a nuclear analytical technique for quantitative and qualitative measurement of the composition of a sample. Samples are exposed to free neutrons in a process called irradiation, using a reactor or other irradiator. Certain isotopes with an appropriately high likelihood of interacting with the neutron (high neutron cross section) will scatter or absorb the neutron. Absorption can lead to stable isotopes or nuclides that undergo radioactive decay. The resultant radionuclides each have a distinctly identifying method of decay, based on the type, energy, and half-life of the radiation. The radioactivity can be

analyzed using gamma spectroscopy or another radiometric technique to measure the radiation of the constituent isotopes.[79]

The number of radioactive atoms present (N) at a given time after irradiation (t_{cool}) is a function of the neutron flux (φ), the cross section (σ), the number of target atoms (N_T), the decay constant (λ) and the irradiation time (t_{irr}), assuming isotropic irradiation.

$$N = \varphi\sigma N_T(1 - e^{-\lambda t_{irr}})e^{-\lambda t_{cool}} \quad (14)$$

Because decay is characterized by the number of nuclear transformations of each atom of the specific isotope, it is proportional to both the mass of the radionuclide and its activity. Therefore, the count rate (R) observed by a detector at a given decay energy (for example, the γ-energy) is usually defined as its activity (A), multiplied by the efficiency (ψ) of the detector.

$$A = \lambda N \quad (15)$$

$$R = \lambda\psi\varphi\sigma N_T(1 - e^{-\lambda t_{irr}})e^{-\lambda t_{cool}} \quad (16)$$

Using this equation, the activity of an irradiated sample can be used to back-calculate the original number of atoms, mass, or concentration of the original (parent) isotope in the sample. As with most spectroscopic techniques, irradiating a set of standards with known concentrations of the isotope in parallel with the samples to construct a calibration curve can be used in lieu of **Equation 16**, especially if one or more of the variables is unknown or estimated. Analysis of NAA samples is usually performed using gamma-ray spectroscopy, which identifies and quantifies the amount of characteristic gamma rays of the radionuclides produced.

3.3 Extended X-Ray Absorption Fine Structure (EXAFS)

X-ray absorption spectroscopy (XAS) is an atomic probing technique that uses x-rays to examine the local structure, geometry and electronic structure of an atom. XAS utilizes a photon from an incident x-ray which interacts with an electron, exciting the electron to an unoccupied, higher state and leaving behind a core hole. This is an inner-shell spectroscopy, meaning the x-rays typically interact with a 1s, 2s or 2p electron, requiring a tunable, high-energy x-ray beam typically found at a synchrotron facility.[80]

The core hole is filled within femtoseconds by a higher energy core-electron, which results in the discharge of either an x-ray photon or a secondary (Auger) electron. The former is called x-ray fluorescence and predominates in higher energy x-ray regimes (>2 keV), and the latter is called the Auger Effect which is most frequent in the lower energy x-ray regime.[81] The incident x-ray energy/excitation energy must be greater than that of the binding energy for either of these to occur. When the x-ray energy exactly matches the binding energy, there is a sharp increase in absorption, which is called the absorption edge in XAS. If the electron is highly excited beyond this point, it is completely ejected from the atom through the photoelectric effect.

The edge energy depends exponentially on the atomic number (Z^2), meaning it is element specific. Thus, for elements with higher atomic number, such as uranium, a lower energy L or M shell electron is typically targeted rather than a K shell electron to utilize the energy regime achieved by most x-ray beams at synchrotrons.

Each atom naturally has a probability of absorption based on Beer's Law for x-rays:

$$I = I_0 e^{-\mu t} \quad (17)$$

Where I_0 is the intensity of the incident x-ray beam, I is the transmitted intensity through the sample, μ is the absorption coefficient, and t is the path length/sample thickness. Note that I can represent a photon of any energy or wavelength along the electromagnetic spectrum, which encompasses both the UV-visible region for fluorescence and the x-ray region for XAS techniques. Therefore, the absorption coefficient as a function of energy $\mu(E)$ is an important constant calculated through XAS data acquisition. For transmission XAS, it is measured in accordance with Beer's law as:

$$\mu(E) = log\left(\frac{I_0}{I}\right) \tag{18}$$

And for fluorescence XAS as:

$$\mu(E) \propto \frac{I_f}{I_0} \tag{19}$$

Where I_f is the fluorescence intensity of the sample.

Following the absorption edge, oscillations can be observed in a spectrum of $\mu(E)$ vs. energy. The x-ray absorption near edge structure (XANES) is the region immediately above the absorption edge (within 50 eV), whereas the extended x-ray absorption fine structure (EXAFS) is the higher energy region following the XANES region. At energies higher than the absorption edge, the ejected electron approximates a wave and interacts with the surrounding environment, causing scattering. This includes adjacent, bonded atoms, as well as those in the surrounding medium, such as other atoms in a solution. The backscattered wave can return to the original, central atom with a phase and amplitude characteristic of the scattering atom and interfere constructively or destructively with an outgoing wave depending on its properties. The interference between the waves is

incorporated as a modulation of the absorption coefficient, causing oscillations. The frequency tends to indicate the distance from other atoms, while the amplitude shows the identity and coordination number of neighboring atoms.[82]

These oscillations are modeled as the EXAFS fine-structure function χ(E), defined as:

$$\chi(E) = \frac{\mu(E)-\mu_0(E)}{\Delta\mu_0(E)} \quad (20)$$

Where $\mu_0(E)$ is a smooth background function fit from the oscillating EXAFS region that is assumed to be the "bare atom" absorption and $\Delta\mu_0(E)$ is the difference between the absorption immediately before the edge and immediately after the edge at the smooth function. Rather than relating this function to the energy of the photoelectron, it is typically derived as a function of the wavenumber k following the preference to model it as a wave undergoing interactions.

$$k = \sqrt{\frac{2m(E-E_0)}{\hbar^2}} \quad (21)$$

Where E is the energy of the photoelectron, E_0 is the absorption edge energy, m is the electron mass and $\hbar$ is the reduced Planck constant.

The derivation of the overall fine-structure as a function of the wavenumber from first principles is quite complicated and involves several important concepts such as Fermi's Golden Rule, the Bohr radius, Green's function for multiple scattering theory, a damped spherical wave correction, and a number of different approximations, among others.[80,81] This is beyond the scope of this introduction, as the overall EXAFS equation incorporates these principles into a single, albeit complex, equation, which different

computational codes fit using *ab initio* calculations. The overall EXAFS equation is defined as:

$$\chi(k) = \sum_j \frac{N_j f_j(k) e^{-2k^2\sigma_j^2}}{kR_j^2} sin\left(2kR_j + \delta_j(k)\right) \quad (22)$$

$$\chi(k) = \sum_j \frac{N_j S_0^2}{kR_j^2} f_j(k) e^{-2R_j/\lambda_j(k)} e^{-2k^2\sigma_j^2} sin\left(2kR_j + \delta_j(k)\right) \quad (23)$$

This equation is the sum of all relevant variables over all identical scattering atoms in the *j*th atomic shell. N_j is the number of scattering atoms and R_j is their distance from the central atom. $f_j(k)$ is the backscattered amplitude and $\delta_j(k)$ is the backscattering phase of a photoelectron scattered by an atom in the *j*th atomic shell. S_0^2 is the amplitude reduction factor, which in principle is due to the relaxation of outer shell electrons when a core hole is generated, but in practice is a fitting parameter accounting for anything affecting the amplitude of the scattering.[83] $\lambda_j(k)$ is the wavenumber dependent inelastic mean free path of the photoelectron. σ_j^2 is a measure of disorder in the neighboring atom distance, and $exp(-2k^2\sigma_j^2)$ is considered the effective Debye-Waller factor which incorporates additional thermal vibration and motion and structural disorder.[84]

Typically, $f_j(k)$, $\delta_j(k)$ and $\lambda_j(k)$ are the terms that are derived theoretically by some computational code, such as FEFF and the rest are fit according to data acquired. It is important to note this EXAFS equation assumes a single electron approximated as a spherical wave undergoing a single scattering event and does not handle multi-excitation or multi-scattering events nor disorganized environments well.

3.4 Dynamic Light Scattering

Dynamic light scattering is a nondestructive analytical technique for measuring the size distribution of particles in solution based on the scattering of light by the particles. All molecules suspended in liquids or gases have Brownian motion, which is random movement within the medium due to the solute and solvent molecules interacting and changing direction upon collision. The speed of this movement is dependent on factors such as the size of the particle and the temperature. Smaller particles will move faster upon collisions with other particles, whereas larger particles will move more slowly according to the principle of conservation of momentum. Therefore, the velocity of particles in a solution can be correlated to the size of the constituent molecules. However, particles will also move faster at higher temperatures and slower at lower temperatures, and therefore the temperature must be known and uniform within a sample to relate the velocity of particles to their size.

An incoming beam of light, typically from a laser, passing through a solution will scatter when interacting with the particles undergoing Brownian motion. The light mostly scatters elastically and isotropically because the particles in solution are much smaller than the wavelength of the light, called Rayleigh scattering. There is constructive and destructive interference between scattered light waves and further secondary scattering from other particles. The type and intensity of interference changes over time both because of the size of the particles and the fact that the particles are in motion. Smaller particles cause changes in signal more quickly because there are more in a given volume, whereas there are fewer larger particles in a volume of similar size. [85,86]

The intensity as a function of time can be measured directly, but it is easier to simply compare the signal at one time to another time. The comparisons are made between very small, discrete time intervals δt (nanoseconds to microseconds) so the intensities between two time points can be assumed to be related within that time frame because the particles cannot move very far. For much larger time intervals, the same assumption could not be made due to the rapid motion within the medium. This analysis is done with an autocorrelator, which measures the correlation function via a correlation coefficient with a value of 0.00 (no correlation) to 1.00 (perfect correlation) beginning with an initial time t and multiples of the delay time, e.g. $t + \delta t$, $t + 2\delta t$, $t + 3\delta t$, and so on. Eventually, the time spacing is so large that the particles will be assumed to be no longer correlated (0.00).[85]

The fluctuations in intensity over time are modeled by a second order correlation function of the form:

$$g^2(\tau) = \frac{<I(t)I(t+\tau)>}{<I(t)>^2} \tag{24}$$

Where I is the intensity of light at time t, and τ is the delay time (e.g. the amount of time that the function is shifted from the origin at t = 0). The brackets indicate an averaging over all times. The intensity is proportional to the particle radius to the sixth power and inversely proportional to the laser wavelength to the fourth power. The resultant correlation function is an exponentially decaying function of the delay time τ:

$$g^{(2)}(\tau) = B(1 + \beta e^{-2\Gamma\tau}) \tag{25}$$

Where B is the baseline of the correlation function or the minimum value that the function decays to at infinite time, β is the correlation function amplitude, and Γ is the decay rate.

For samples with many different size particles (polydisperse), the correlation function is written as:

$$g^{(2)}(\tau) = B(1 + \beta(g_1(\tau)^2) \quad (26)$$

The decay rate is further related to Brownian motion in the form:

$$\Gamma = Dq^2 \quad (27)$$

Where D is the translational diffusion constant and q is the magnitude of the scattering vector, defined as:

$$q = \frac{4\pi n_0}{\lambda_0} sin\left(\frac{\theta}{2}\right) \quad (28)$$

Where n_0 is the index of refraction of the solvent, λ_0 is the wavelength of the incident beam and θ is the scattering angle. Solving for the diffusion constant using **Equation 27** and **28**, the hydrodynamic diameter of the particle can be calculated as:

$$d(H) = \frac{kT}{3\pi\eta D} \quad (29)$$

Where k is the Boltzmann constant, T is the temperature, and η is the solvent viscosity. This is termed the Stokes-Einstein equation and involves a few assumptions, namely that the particle is approximately spherical and diffusing in a medium with proportionally small molecules and a low Reynolds number (continuous, non-turbulent fluid motion). In addition, the ionic concentration must be sufficiently high.[85] The ionic concentration is inversely proportional to the electric double layer of charge around the surface of the particles, so an increase in the concentration will reduce the likelihood of a thick, stationary electric double layer of charge that will artificially increase the hydrodynamic diameter.[86]

Different software uses different algorithms to represent the size of particles. The size of particles in a polydisperse sample is most commonly represented as a percentage of

the total intensity, which directly correlates to the above equations. This can be converted to a percentage of the total volume using Mie theory.[86] Previously, it was mentioned that DLS is based on the assumption that the particles are smaller than the wavelength of light, whereas the Mie theory weights those particles less due because they are larger compared the wavelength of light. Therefore, there are differences in the shape of the particles and the refractive index between the particles and the solvent.[87] Also, because a size distribution is a histogram of signals in different channels corresponding to sizes, a number-weighted distribution can be calculated by dividing the counts in a given channel from the intensity-based size distribution by the total number of counts. Practically, for polydisperse samples, the volume-weighted and number-weighted distributions are more useful, but the user community tends to prefer reporting DLS results with intensity-weighted distributions to avoid compounded errors and assumptions resulting from the transformation to volume- and number-weighted distributions.

3.5 Ultraviolet-Visible-Near Infrared (UV-Vis-NIR) Spectroscopy

UV-Vis spectroscopy is an analytical technique based on the electronic absorption of photons. Light of a given energy from a light source that matches the difference in energy between two electronic states in the molecule will be absorbed by the molecule to promote one electron to a higher electronic orbital. This is a complementary technique to fluorescence, which measures the de-excitation of an electron to the ground state. The extent of this absorption and its location along the electromagnetic spectrum is unique for every molecule, and can occur at multiple wavelengths depending on the available transitions. The wavelengths of light with the energy needed for most electron transitions

spans the range of 100 nm to 780 nm, which correlates to the UV to visible region. The most probable electronic transitions will be by valence shell electrons from the highest occupied molecular orbital (HOMO) to the lowest unoccupied molecular orbital (LUMO), which encompasses transitions such as σ to σ^*, n to σ^*, π to σ^*, σ to π^*, n to π^*, π to π^*. Wavelength is inversely proportional to energy, so the higher energy transitions in the UV region encompass most of the potential transitions, whereas the visible region typically can only achieve the lower energy n to π^* or π to π^* transitions. The NIR spectral region, from 780 to 2500 nm, is mainly dominated by absorption due to vibrational and stretching motion of chemical bonds, however, weak, low energy *f-f* Laporte forbidden electronic transitions of the lanthanides and actinides can also appear in this region.[88]

Each molecule has a specific probability of an electronic transition occurring at a specific wavelength or energy, which is quantified by a constant called molar absorptivity coefficient (ε). As previously discussed in **Section 2.1.2.**, the lanthanides and actinides tend to have low probability of excitation because many of their valence electron transitions are forbidden by spin or parity. Experimentally, absorbance (A) and concentration (c) are related by the molar absorptivity coefficient and the path length (l) which is the distance the light must travel through the sample:

$$A = \varepsilon l c \tag{30}$$

This is called the Beer-Lambert Law. For lanthanides and actinides, typically a high concentration or a long path length sample holder must be used to obtain an adequate absorbance signal given the low molar absorptivity.

Complexation of an absorbing molecule, such as a metal ion, with a ligand can decrease the characteristic absorbance peaks of the UV-visible-NIR spectrum in a number of ways. Part of the absorbance can be shifted to higher wavelengths, corresponding to lower energy. This phenomenon, called red shift or bathochromic shift, is due to stabilization of the excited state with a ligand, usually based on higher polarity, which decreases the energy gap of the transition. The opposite blue shift, or hypsochromic shift, is due to better stabilization of the ground state versus the excited state, decreasing the gap of the transition. Charge transfer bands can result when an electron from the ground state of a ligand is excited to an excited state of the complexed metal which is at a similar energy level as an excited state of the ligand, which is called a ligand-to-metal-charge transfer (LMCT). The reverse can happen from a metal ground state to a ligand excited state, called a metal-to-ligand charge transfer (MLCT) band. This is similar to charge transfer bands discussed in uranyl ion luminescence, except with interaction with a separate ligand molecule, rather than the oxygens in the polyatomic actinyl cations. It is important to note these new or shifted peaks may not be observable due to limitations of the spectrometer, especially in the UV region.

Chapter 4: Experimental Approach

4.1 Materials

Sodium nitrate was obtained from (VWR). Generations 0 through 3 PAMAM dendrimers with ethylenediamine cores were purchased from Sigma-Aldrich in 20% methanol. Dendrimers were dried in air before reconstitution in any other solvents. Depleted uranyl nitrate hexahydrate was used as received from International Bio-Analytical Industries, Inc. Neodymium nitrate in its aqueous form was dried by heat before reconstitution in any solvent. All aqueous solutions were made with deionized and degassed water purified by UV-photo-oxidation and an ultrafiltration membrane to a resistivity of 18.2 MΩ·cm or less with a Barnstead™ GenPure™ UV/UF unit, followed by purging with nitrogen gas to remove dissolved CO_2.

4.2. Preparation of Samples

PAMAM dendrimer complexes were prepared in one of two ways. For fluorescence spectroscopy (steady-state and time-resolved) and neutron activation analysis, several samples were prepared with a constant concentration of G*X* PAMAM dendrimer (where *X* is 0, 1, 2 or 3) and a variable amount of metal ion such that the molar ratios of metal ion to G*X* PAMAM dendrimer ranged between 0 (no metal ion) to 1 (one metal ion to one dendrimer) in increments of 0.1, and from 1 to 35 (a large excess of metal ions) in increments of 5. UV-Vis spectroscopy samples were prepared with a constant concentration of metal ion and a variable amount of G*X* PAMAM dendrimer such that the molar ratio of G*X* PAMAM dendrimer to metal ion ranged from 0 (no dendrimer added) to 1.

4.2.1. Fluorescence Samples

The fluorescence samples were prepared from four stock solutions: 1) a 1 M sodium nitrate stock at a pH of 7-7.2, 2) a 0.01 M metal ion (in nitrate form) in 1 M sodium nitrate stock at a pH of 3-3.2, 3) a 0.1 M metal ion (in nitrate form) in 1 M sodium nitrate stock at a pH of 3-3.2, and 4) a ~0.004 M G*X* PAMAM dendrimer in 1 M sodium nitrate stock at a pH of 7-7.2 (**Figure 4**). The metal ion was either neodymium (III) or uranyl (VI).The sodium nitrate stock and the dendrimer stock were mixed together first, then an aliquot of the metal ion stock was added to the solution to obtain the desired molar ratio with a total volume of 2.5 mL. The 0.01 M metal ion stock solution (2) was used for molar ratios of metal ion to dendrimer between 0:1 and 1:1, while the 0.1 M metal ion stock solution (3) was used for molar ratios of metal ion to dendrimer >1:1. Final ratios are reported as a ratio XX.X:1 relative to a 1 mM G*X* PAMAM dendrimer solution, e.g. a 0.1:1 ratio refers to a 0.1 mM metal ion solution in a 1 mM PAMAM dendrimer solution.

The solutions were shaken on a vortex mixer for an hour and then left to equilibrate overnight for at least 12 hours. The pH was measured prior to analysis. The multiple amine sites of the PAMAM dendrimer tended to buffer the solutions well, and the final pH of the equilibrated samples ended up between pH 6.8-7.2. However, dilute HNO_3 or NaOH were used to adjust the pH of the samples if necessary. Samples made with the uranyl ion had visible precipitation at high metal ion loading (depending on the dendrimer generation) which was not observed with other metal ions.

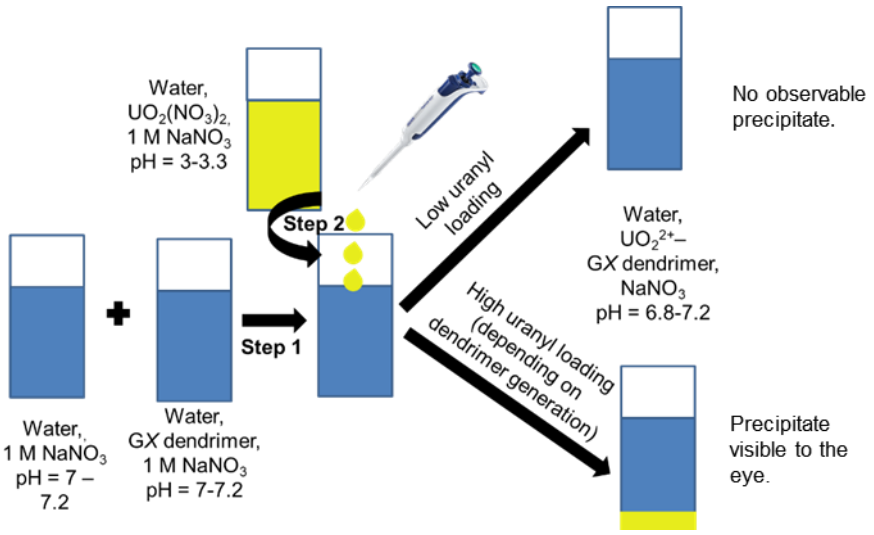

Figure 4. Sample Preparation and Formation of Precipitate.

All samples were centrifuged for 5 minutes at 4000 rpm, whether precipitate was observed by eye or not. The supernatant was separated from the precipitate into a clean glass vial using a disposable plastic pipette for analysis.

4.2.2 NAA Samples

The stock solutions for neutron activation analysis were the same concentrations and volumes as those detailed in **Section 3.2.1** and prepared with the same methods. However, all stock solutions were prepared with only the uranyl ion and in a 1M potassium nitrate ionic medium, rather than sodium nitrate. The precipitate (observable or undetectable by eye) remaining in the vial was dissolved in 3 mL 1 M HNO_3, which led to a clear solution. Both the supernatant and dissolved precipitate were utilized for these experiments.

4.2.3 EXAFS Samples

EXAFS samples were prepared using a 0.1 M uranyl nitrate in 1 M $NaNO_3$ stock solution, a 11-16 mM G*X* PAMAM dendrimer in 1 M $NaNO_3$ solution (depending on the generation) and a 1 M $NaNO_3$ stock solution. Fourteen samples (Sample 2-14) were prepared at a neutral pH with a variety of uranyl:G*X* PAMAM dendrimer ratios using different volumes of the stock solution for G0-G3, according to **Table 2.** The prepared samples held the uranium concentration at 5 mM for adequate and comparable signal using fluorescence-EXAFS data collection, and the concentration of the dendrimer was varied to achieve the desired uranyl:G*X* PAMAM dendrimer ratio. A fifteenth sample (Sample 1) acted as a uranium standard, with 5 mM $UO_2(NO_3)_2$ in 1 M $NaNO_3$, with an approximate pH of 3.2. The volume size for each prepared sample was only 500 µL, of which a 90 µL aliquot was taken from each sample for analysis.

Table 2. Samples prepared for EXAFS experiment.

Sample Number	Dendrimer Generation	Uranyl:Dendrimer Ratio
1	N/A	5 mM $UO_2(NO_3)_2$
2	G0	1
3	G1	1
4	G2	1
5	G3	1
6	G1	2
7	G2	5
8	G3	10
9	G1	0.5
10	G2	0.5
11	G1	5
12	G1	15
13	G0	0.5
14	G3	0.5
15	G3	20

4.2.4. DLS Samples

Two samples with molar ratios of 0.1:1 UO_2^{2+}:G2 PAMAM dendrimer and 0.5:1 UO_2^{2+} G2 PAMAM dendrimer were prepared in the standard procedure described in **Section 4.2.1.** The samples were left to equilibrate overnight and measured the following day. A third sample was prepared by first mixing the PAMAM dendrimer and 1 M sodium nitrate stock solution together in a cuvette. The cuvette was inserted in the sample holder of the DLS instrument. An aliquot of the uranyl nitrate solution was added by submerging a pipette tip halfway into the volume of solution in the cuvette and slowly depressing the plunger button before removing the pipette. The final composition of the solution was 0.5:1 UO_2^{+}:G2 PAMAM dendrimer of the typical volume and composition as described in **Section 4.2.1.**

4.2.5. UV-Vis-NIR Samples

UV-Vis-NIR samples were prepared based on the molar absorptivity coefficients of the given species. Samples were designed to have an absorption of 0.5-0.7 a.u. for the maximum peak with the given flow cell utilized. Because the absorbance is highly dependent on the solvent and surrounding environment, as previously discussed, the stock solutions were typically assayed at acidic pH<2 using a Cary 14 UV-Visible spectrometer prior to pH adjustment and sample preparation. After pH adjustment, the absorbance was re-measured to determine the optimal concentration given the sample environment.

For neodymium (III) samples, three stock solutions were prepared: a 10 mM $Nd(NO_3)_3$ stock solution in 1 M sodium nitrate at a pH of 3, a 1 M sodium nitrate solution at a pH of 7-7.2 and a 4 mM G*X* dendrimer solution at a pH of 7-7.2. Various amounts of the

three stock solutions were mixed such that each sample had a final concentration of 0.35 mM neodymium (III), a molar equivalent of 0.0 – 1.0 G*X* PAMAM dendrimer:Nd^{3+} in increments of 0.1, and an overall ionic strength of 1 M sodium nitrate. The final pH was approximately 6.8 – 7.2.

For neptunyl (V) samples, three stock solutions were similarly prepared: a 10 mM NpO_2NO_3 stock solution in 1 M sodium nitrate at a pH of 3, a 1 M sodium nitrate solution at a pH of 7-7.2 and a 4 mM G*X* dendrimer solution at a pH of 7-7.2. Various amounts of the three stock solutions were mixed such that each sample had a final concentration of 1 mM NpO_2^+, a molar equivalent of 0.0 – 1.0 G*X* PAMAM dendrimer:NpO_2^+ in increments of 0.1, and an overall ionic strength of 1 M sodium nitrate. The final pH was approximately 6.8 – 7.2.

Neptunyl (VI) was prepared by dissolving 240 µL of approximately 2 M $NpNO_3$ stock solution in 3 mL of 4 M HNO_3. The solution was heated to near dryness and redissolved in 3 mL of 4 M HNO_3. The heating and redissolution steps were repeated four times, then when the solution was evaporated to near dryness a fifth time, it was redissolved in 1 M sodium nitrate for a final concentration of 12 mM $Np(NO_3)_2$. The solution was adjusted to a pH of 3 by bubbling ammonium nitrate through the solution. A 1 M sodium nitrate stock solution was prepared in the standard manner. A 20 mM G*X* PAMAM dendrimer solution in 1 M sodium nitrate was also prepared. The concentration of neptunyl (VI) and dendrimer in the prepared samples was slightly higher compared to samples with other metal ions due to the fact that the molar absorptivity coefficient of Np (VI) is low and a standard 1 cm plastic cuvette was used to better measure the absorption and potential precipitation over time

(flow cells can have unstable signal or air bubbles develop in stagnant samples). Seven samples were created with a concentration of 4.5 mM $Np(NO_3)_2$, a molar ratio of 0, 0.1, 0.3, 0.5, 0.7, 0.9 or 1 G*X* PAMAM Dendrimer: $Np(NO_3)_2$, and an overall ionic strength of 1 M sodium nitrate. The final pH was approximately 6.8 – 7.2, though the pH varied over time as Np(VI) was reduced to Np(V)

4.3. Experimental Techniques

4.3.1. Fluorescence Spectroscopy

Steady-state fluorescence spectroscopy was collected using a standard Cary Eclipse fluorescence spectrometer. The excitation wavelength was set at 360 nm. Time-resolved fluorescence was measured on an ultrafast setup equipped for time-correlated single photon counting (TCSPC). The samples were excited by a 13 fs second harmonic of an 800 nm laser pulse. The probe laser pulse and the incoherent fluorescence of the sample were focused on a barium borate (BBO) nonlinear crystal. When the probe laser pulse reaches the crystal, it acts as a light gate pulse and upon the arrival of the fluorescence, the sum frequency of the photons was generated. This sum-frequency signal was detected by a charge-coupled device (CCD) spectrograph. Varying the time delay of the gate pulse allowed the time resolution of the fluorescence to be measured by relating the sum-frequency generation to the correlation function between the probe laser intensity and the fluorescence intensity.[89,90]

4.3.2 Neutron Activation Analysis

To determine the amount of uranyl in both the liquid phase and the solid

precipitate NAA was utilized. 1 mL of the supernatant and 1 mL of the re-dissolved precipitate were transferred to sealed polyethylene vials (NAA grade, LA Container) in duplicate. The duplicates were stacked and sealed in a larger polyethylene vial as secondary containment, then put into TRIGA irradiation tubes as tertiary containment. The vials were irradiated in the UCI TRIGA Reactor for 1 hour at 250 kW in the rotary sample position (lazy susan), with one large polyethylene vial to each position. The estimated thermal neutron flux is $8.0*10^{11}$ neutrons/s*cm^2.

The samples tested include depleted uranium, which contains over 99.7% U-238. Upon absorption of a neutron, U-239 is produced. The half-life of U-239 is a relatively short 23.45 minutes, so samples are typically left in a lead-shielded container for 24 hours or more so nearly all U-239 undergoes beta decay to Np-239 with a half-life of 2.36 days. The primary gamma energy of Np-239 is 106 keV, which is closely grouped with a number of plutonium K x-rays of similar energy from the daughter product Pu-239 (**Figure 5**).[77]

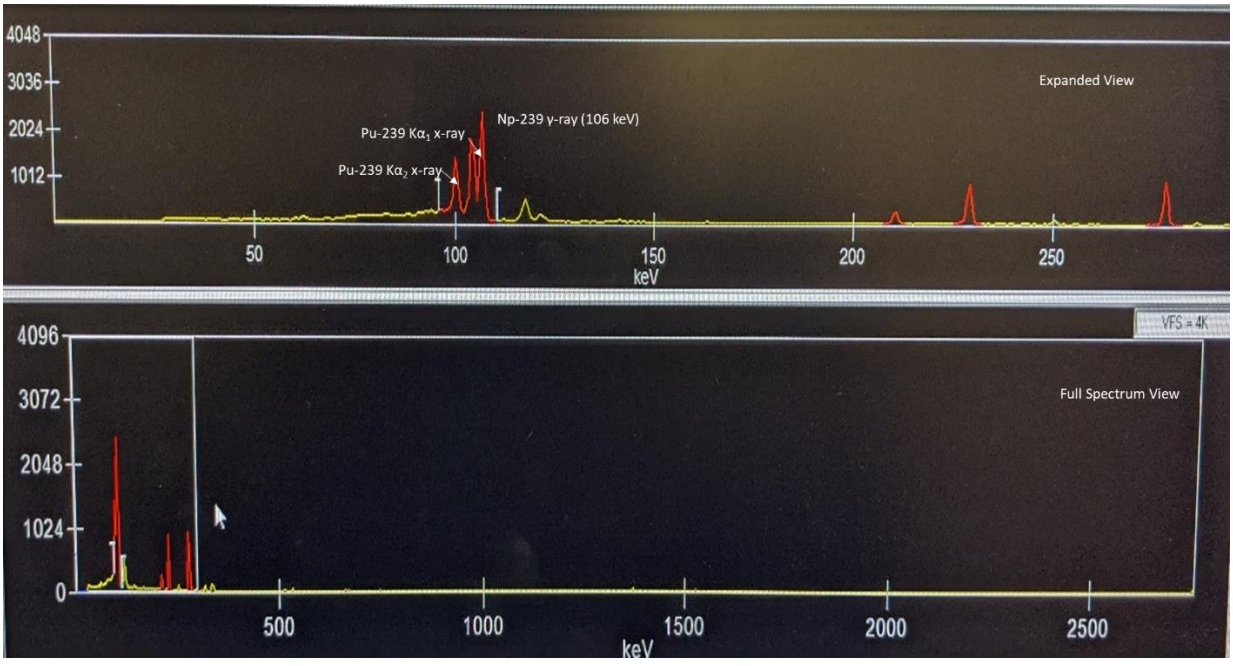

Figure 5. Gamma Spectrum of Np-239.

A liquid nitrogen cooled Canberra high purity germanium (HPGe) detector is then used to count the area under the triplet peak (the identified region of interest or ROI, see **Figure 5**), and the data is collected by Genie 2000 Gamma Analysis software. For adequate statistics, particularly low error counts, the acquisition was terminated at a minimum of 10000 counts in the specified triplet ROI with a dead time of 5% or less. Highly radioactive samples which would achieve 10000 counts in a matter of seconds would be set to record data for a minimum of 120 seconds. The number of counts in the 106 keV peak is recorded. Although the irradiation of the samples ends at exactly the same time, the samples continue to decay during the gamma spectroscopy measurements, which can take multiple hours. The activity of the sample was corrected for the decay from the end of irradiation to the time of measurement, which corresponds to t_{cool} from **Equation 16**.

$$A = A_0 e^{-\lambda t_{cool}} \tag{31}$$

Where A_0 is the initial activity immediately after irradiation, and A is the activity at the time t_{cool} after irradiation. A set of uranium standards at pH 3 in a range of different concentrations is irradiated in parallel with the samples to determine the concentration of uranium in each sample (after the activity decay correction). Typically, four to five $UO_2(NO_3)_2$ standards were used in duplicate to create a standard curve. This curve accounts for variations in the neutron flux in the stacked vials during irradiation, the distance from the detector, and the efficiency of the HPGe. From the recorded standard curve, the concentration of uranium in the original sample can be back-calculated, accounting for time elapsed since the irradiation and the sample size.

4.3.3 EXAFS

Each sample was individually loaded into an SSRL radioactive material sample cartridge ("primary") of type 1u (**Figure 6**), which consisted of polyvinylidene fluoride (PVDF) with a carved sample chamber sealed with a plug and O-ring. Each side of the holder was sealed with Kapton film epoxied on the PVDF. Three cartridges were fit into a secondary PVDF holder, consisting of two sides screwed together, each with three windows for the beam to interact with the three samples in turn (**Figure 6**).

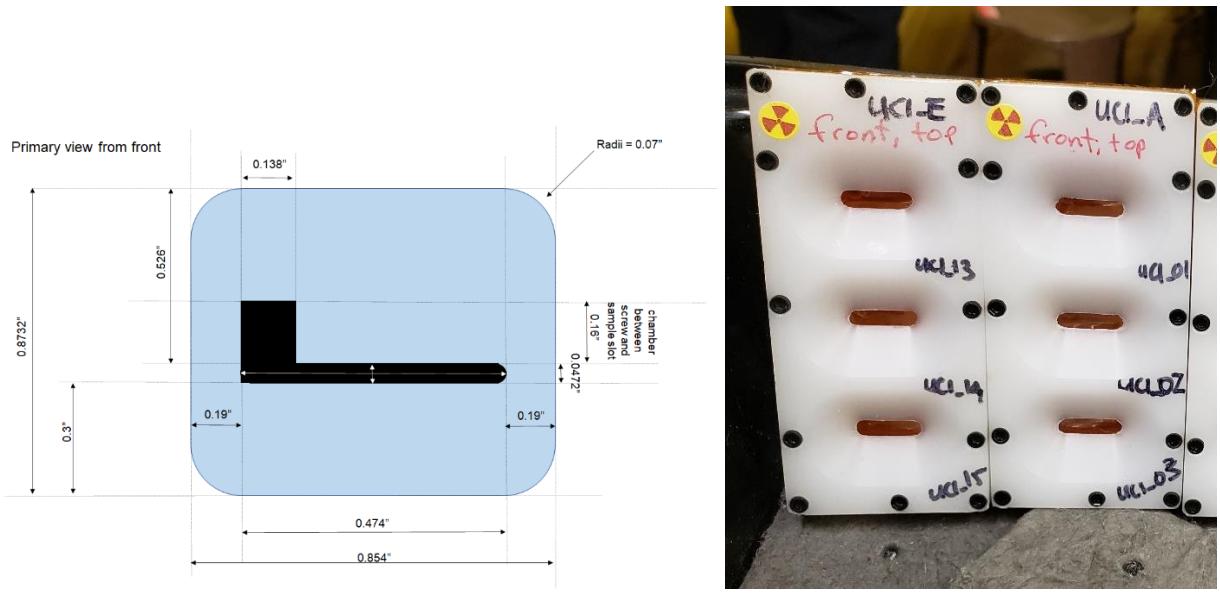

Figure 6. Images of an EXAFS cartridge sample holder drawing (left) and two secondary holders (right), each of which hold three of the sample cartridges.

XAS was performed at the SLAC National Accelerator Laboratory in the Stanford Synchrotron Radiation Lightsource on Beamline 11-2 from March 25-27, 2019 under Proposal 5182. The uranium L_3-edge is approximately 17.16 keV, so the X-ray fluorescence spectrum was collected in the energy range of 17.00 – 18.10 keV. Energy selection was attained with a double-crystal silicon (220) monochromator. The energy beam was

detuned approximately 30% to reject higher order harmonics. A high resolution, monolithic solid-state 100-element germanium detector collected XAS data in fluorescence mode due to the low concentration of uranium.

Samples were measured at ambient room temperature. A sample containing 0.2 μCi U-238 in the UO_2 form was used as a standard to calibrate the energy spectrum. The same standard was measured in parallel with each sample and the I_1/I_2 fluorescence signal was collected as a comparison with the sample signal. The secondary holders were loaded into tertiary holders which are fixed at an approximately 45° angle to both the incident beam and the detector (**Figure 7**).

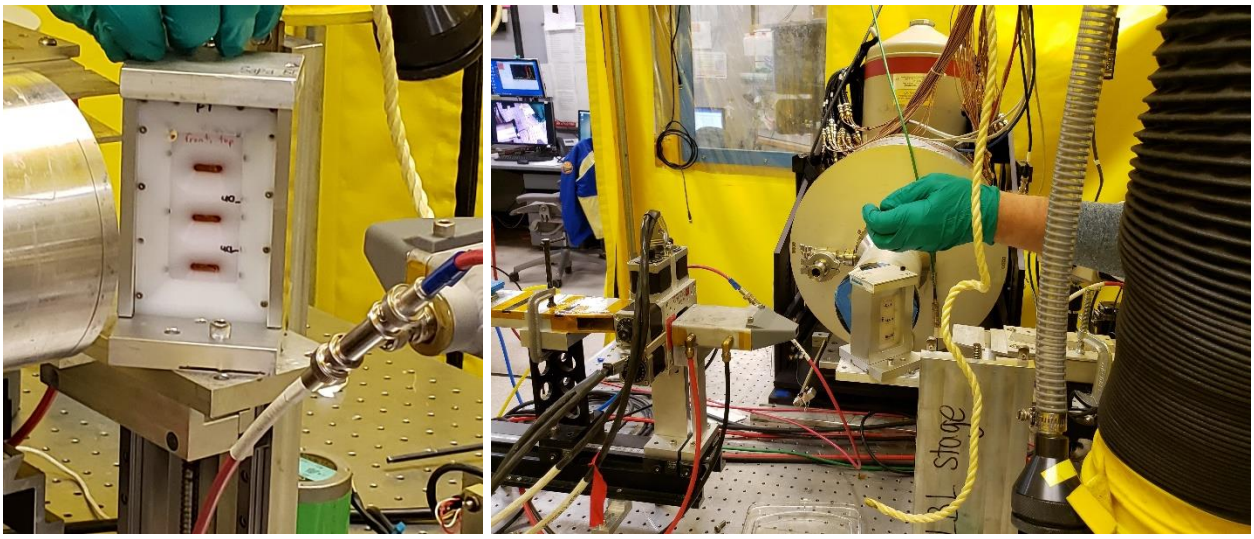

Figure 7. Front (left) and back (right) perspective of the beam, tertiary sample holder, and detector alignment

The beam was aligned manually using xMAP GUI, the software interface, to enter the window of the selected sample. For each sample, signal was collected for 1.5 – 2 hours for adequate signal to noise ratio averaged over approximately 6 scans, and therefore each

secondary was changed manually every 4.5 – 6 hours when all three samples in the secondary were measured.

4.3.4. DLS

DLS measurements were obtained using a Malvern Panalytical Zetasizer Nano ZS instrument. The refractive index was set as 1.333 for the solvent, water, and 1.430 for the G2 PAMAM dendrimer. Non-invasive back-scatter (NIBS) detection was used to measure the samples at approximately 173° to reduce multiple scattering effects and the signal from contaminants.[86] The distributions were typically collected in triplicate in a collection time automatically chosen by the Zetasizer software. The time-dependent distributions were collected in triplicate with a time of 10 seconds each.

4.3.5. UV-Vis-NIR Spectroscopy

UV-Vis measurements for neodymium (III) based complexes were obtained using an Ocean Optics Jaz modular spectrometer utilizing the UV-Vis channel (approximately 200-850 nm). A LWCC-2500 liquid waveguide capillary cell, a flow cell with a pathlength of 500 cm, from World Precision Instruments (WPI) was used to amplify the neodymium signal about 500 times compared to the path length of a standard 1 cm cell. Neptunium (V) and (VI) NIR absorbance measurements were collected using a NIR Quest spectrometer with a range of 900 – 2000 nm. NpO_2^+ samples were injected into a 100 mm SMA-Z flow cell from FIAlab instruments to amplify the signal. Prior to injection, the samples were centrifuged at 4000 rpm for five minutes. The supernatant was removed and analyzed. The precipitate, visible or invisible to the eye, remaining in the solution was redissolved in 0.01 M HNO_3 and shaken on a vortex mixer for at least one hour before being removed and injected into

the flow cell for measurement. NpO_2^{2+} samples were measured in 1 cm disposable plastic cuvettes in an Ocean Optics' CUV-UV fiber optic cuvette holder.

Ocean Optics' OceanView software was used to collect the data. The software was set to collect signal for 15 ms for neodymium (III) samples, 3600 ms for neptunium (V), and 250 ms for neptunium (VI) samples for optimal signal (limited by the absorbance of the solvent and the flow cell utilized). Spectra were background subtracted using Origin and smoothed using a Matlab code based partially on Eiler's discrete penalized least squares smothing function.[91] This function was partially inspired by the Whittaker smoother as a matrix and vector-based alternative to conventional Savitzy-Golay smoother that utilizes polynomial fitting and cannot easily deal with missing sections of data and consumes more computational resources compared to using matrix operations.

Chapter 5: Results

5.1. Fluorescence Spectroscopy

Fluorescence spectroscopy measurements were taken in two configurations: steady-state and time-resolved depending on the desired goal of the analysis.

5.1.1. Steady-State Fluorescence Spectroscopy

Steady state fluorescence spectroscopy analyzed the basic strength of binding for a 1:1 uranyl ion-G*X* PAMAM dendrimer complex and estimated the uranyl binding efficiency of generation 0 – 3 of the PAMAM dendrimer.

5.1.1.1 Selection of Excitation Wavelength

The excitation and emission peaks of different generations of PAMAM dendrimers and various lanthanides and actinides can be found in the literature. However, for reasons described in **Chapter 3**, the solution pH, solvent, ionic medium and dendrimer generation can shift the peaks of a typical spectrum. To examine complexation chemistry using the fluorescence of the PAMAM dendrimer alone, it must first be confirmed that an excitation wavelength can be chosen that either selectively excites the PAMAM dendrimer or causes emission of other species in solution at different wavelengths than the PAMAM dendrimer. Using an emission wavelength of 450 nm selected from the literature, each generation of PAMAM dendrimer is found to have two excitation wavelengths at approximately 260 nm and 360 nm (**Figure 8**).

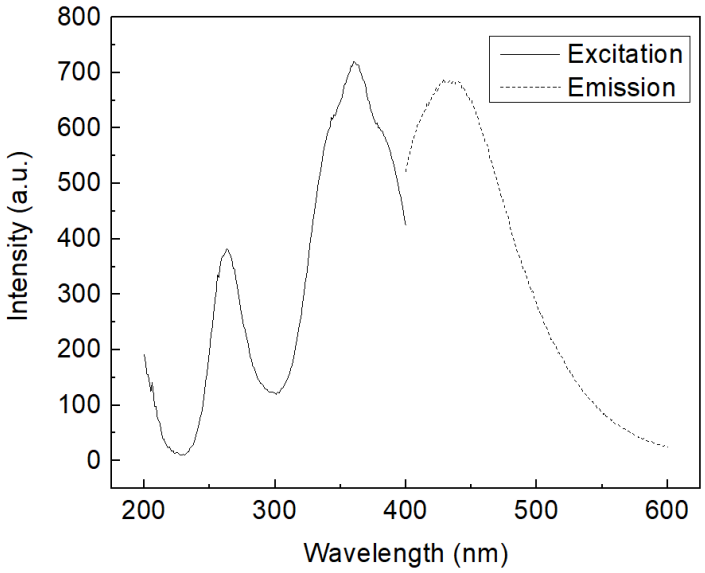

Figure 8. Excitation and emission bands for PAMAM dendrimer generation 2.

The excitation spectrum of the uranyl nitrate solution was obtained at an emission wavelength of 520 nm in accordance with the literature at two pH values representative of 1) the dissociated UO_2^{2+} ion at pH 3.20 and 2) hydroxylated UO_2^{2+} species at pH 7.28. It is noted there is an excitation peak similar to the PAMAM dendrimer at 260 nm (black line), and two additional peaks at around 330 nm and 430 nm (red and blue line) (**Figure 9**).

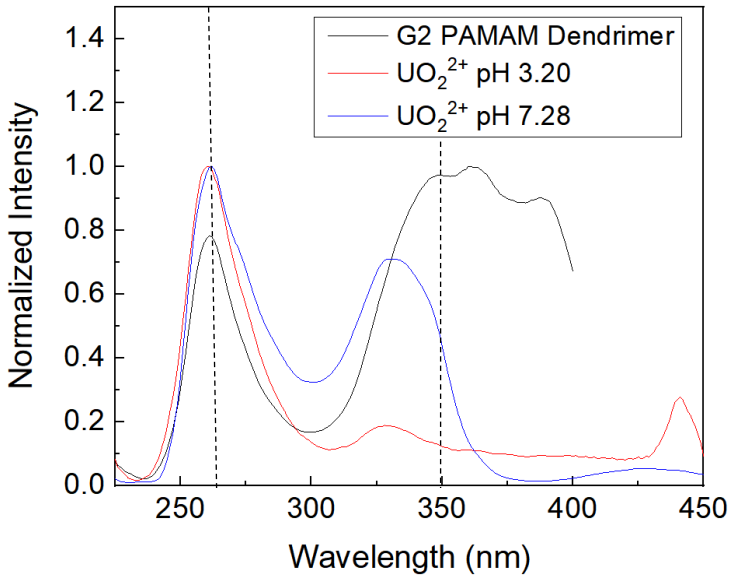

Figure 9. Normalized emission spectrum for a representative G2 PAMAM dendrimer and the uranyl ion at high and low pH. Note λ_{em} = 450 nm for the PAMAM dendrimer and λ_{em} = 520 for the uranyl samples.

The uranyl peaks are slightly shifted depending on the pH of the solution. In accordance with these results, the emission spectrum resulting from the two different excitation wavelengths corresponding to the dendrimer were measured: 260 nm and 360 nm (**Figure 10** and **Figure 11**). The uranyl ion has an intense peak at pH 7.28 (pink line), yet when the pH is decreased to 3.20, the peak(s) are barely visible (green line). This verifies that direct analysis of the uranyl ion would be challenging due to the dependence on the environment. However, there is no interference with the PAMAM dendrimer fluorescence at about 450 nm (black line), nor the uranyl-PAMAM dendrimer complexes (red and blue line), meaning deconvolution is not necessary and a direct analysis of the quenching of the uranyl fluorescence is both possible and simple.

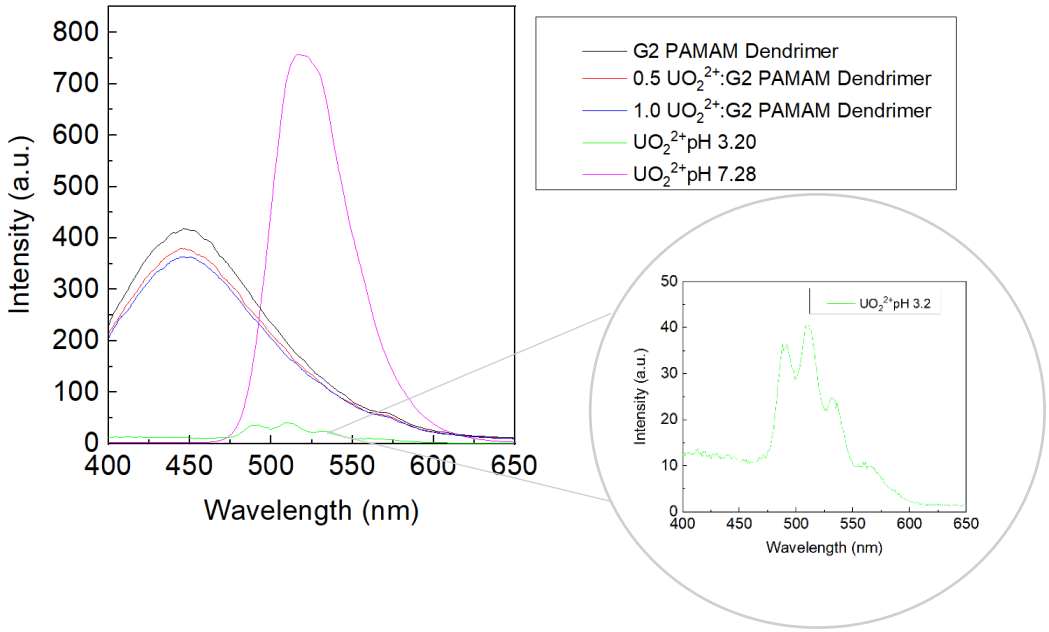

Figure 10. Representative samples with λ_{ex}= 260 nm

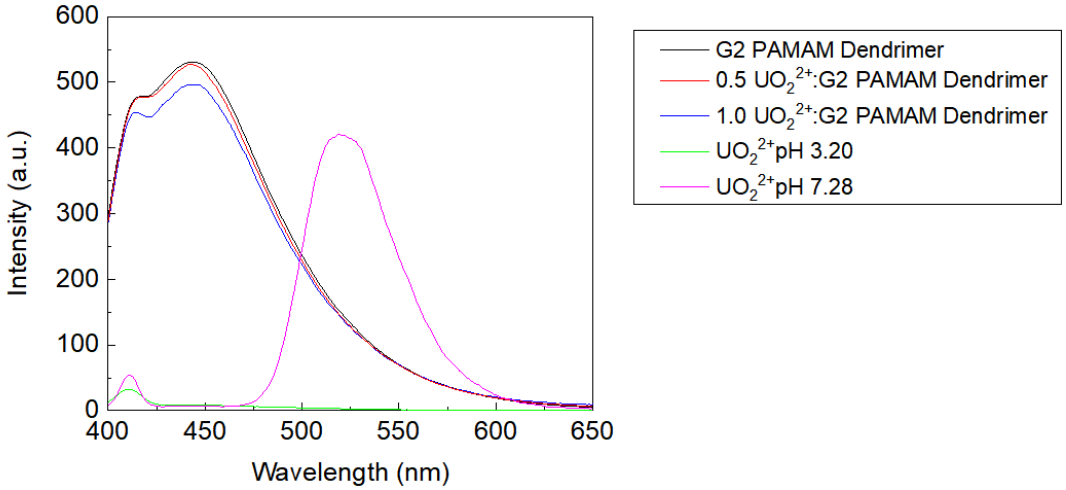

Figure 11. Representative samples with λ_{ex}= 360 nm

Of these two options, an excitation wavelength of 360 nm maximized the fluorescence intensity of the dendrimer and minimized the intensity of the uranyl emission at high pH. Minimizing the uranyl emission at high pH is important to avoid complex signatures that

may arise from overlap of free uranyl in the solution. It is important to note that whether using 260 nm or 360 nm as the excitation wavelength, the emission of the uranyl ion at any pH is negligible at 450 nm using the same experimental parameters, including slit width. Deconvolution of uranyl emission from the dendrimer spectrum will not be necessary to measure quenching effects of the dendrimer emission at 450 nm.

5.1.1.2 pH Effects

Changes in the solution pH can cause protonation or deprotonation of ligand or speciation of the metal ions, which can affect fluorescence intensity and quantum yield of emission peaks. To examine the effect of pH on the fluorescence of the dendrimer and its complexes, solutions of pure G*X* PAMAM dendrimer, 1:1 UO_2^{2+}:G*X* PAMAM dendrimer and 1:1 Nd^{3+}:G*X* PAMAM dendrimer were prepared at variable pH adjusted using dilute HNO_3 and NaOH and analyzed with fluorescence spectroscopy (**Figure 12**). Because the ultimate goal is to measure quenching of the dendrimer fluorescence, the normalized fluorescence intensity at 450 nm is monitored.

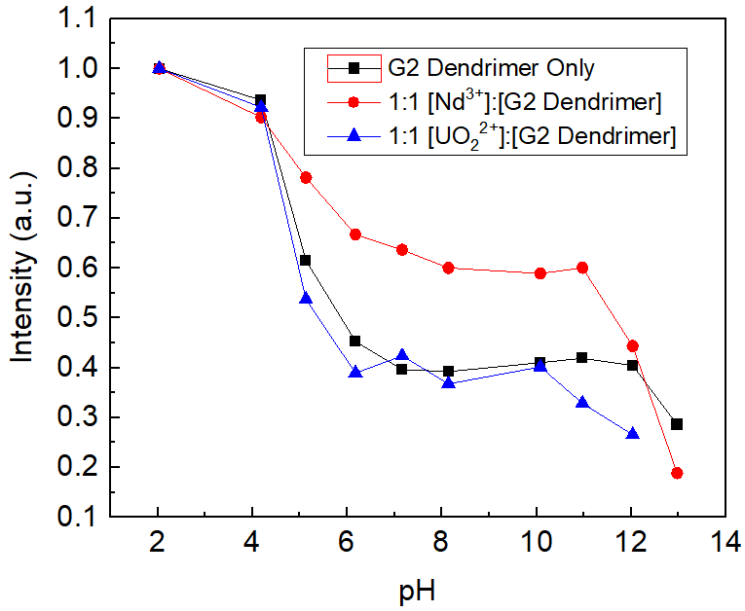

Figure 12. Fluorescence intensity dependence on pH monitored at 450 nm.

Within the range of pH about 6.5 to 10, the fluorescence intensity at 450 nm of the dendrimer itself should not vary significantly. The samples used for steady state fluorescence were chosen to be within the range of pH 7 ± 0.2 for consistency.

5.1.1.3 Stability Constants

With the experimental parameters optimized, several samples were prepared with increasing molar ratios of uranyl (VI) or neodymium (III) to G*X* dendrimer from 0 to to a 1:1 molar ratio of metal ion:G*X* PAMAM dendrimer in increments of 0.1. The sample's fluorescence was measured at 450 nm, the approximate maximum wavelength of dendrimer fluorescence. Three phenomena were observed. First, when G0 PAMAM dendrimer is mixed with either UO_2^{2+} or Nd^{3+}, the fluorescence at 450 nm does not decrease in any observable pattern (**Figure 13**). The signatures of UO_2^{2+} and Nd^{3+}

photoluminescence are observable even with small (<0.1:1) molar ratios of metal ion to GX dendrimer.

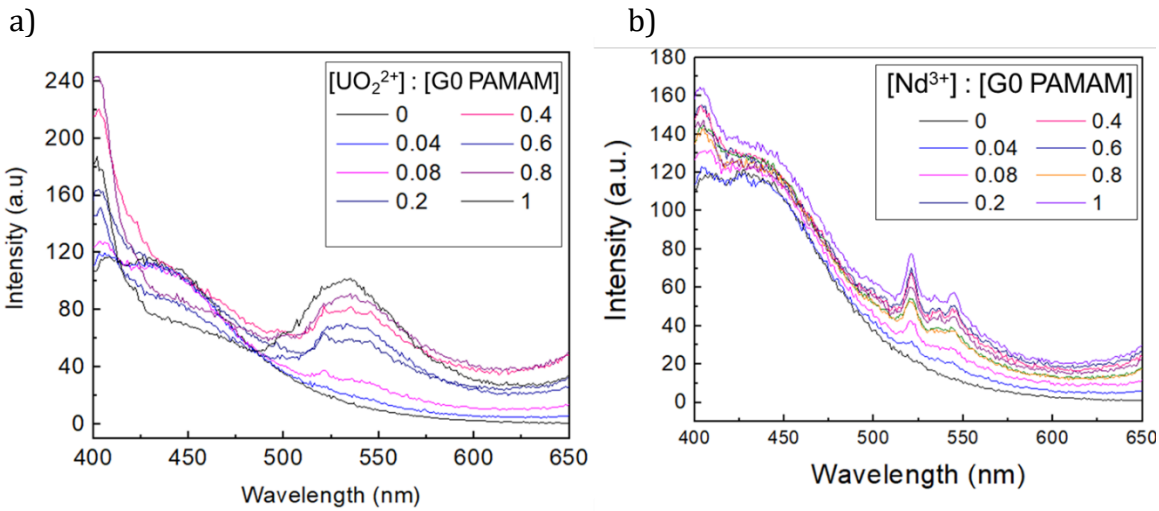

Figure 13. Fluorescence spectra of G0 PAMAM dendrimer complexes with uranyl (a) and neodymium (b).

The presence of free metal ions even with a small molar ratio of metal to ligand and the inability to distinguish a pattern of dendrimer quenching indicates that G0 PAMAM dendrimers only weakly coordinate to metal ions. This would be consistent with the documented dendritic effect in which higher generations of G*X* have additional strength and stability of complexes with metal ions. Larger dendrimers with long branches have more flexibility to orient their coordination sites around the metal ions which results in a transition from an extended, hyperbranched structure to a more globular, compact structure, stabilizing the metal ions mainly in the interior.

In addition to lacking a significant dendritic effect, the smaller generation dendrimers like generation 0 have fewer tertiary amines and rely on the terminal groups, primary amines, as coordination sites. Although generation 0 has four of these primary

amine sites, at pH 7-7.5 at which these samples were prepared, the amines are partially protonated. This data suggests the primary amines preferentially protonate over forming strong, stable complexes with metal ions for Generation 0. This also shows the behavior of UO_2^{2+} is analogous to Cu^{2+} binding with G*X* dendrimers. It has previously been demonstrated that Cu^{2+} preferentially binds to interior terminal amines with only an excess of "weak binding sites" which could either be another internal coordination center, such as the amide groups, or the terminal groups.[55]

Next, for generation 1-3, quenching was observed when the selected generation was mixed with increasing amounts of the uranyl ion. The quenching was noted by a decreasing signal from dendrimer fluorescence intensity at 450 nm (**Figure 14**). Signal in the region of uranium luminescence is minimal, indicating that as the amount of uranium is increased in the samples, only a small amount is not complexed to the dendrimer and is free in the solution. The amount of free uranium remaining in the solution was quantified using neutron activation analysis (see **Chapter 5.3**).

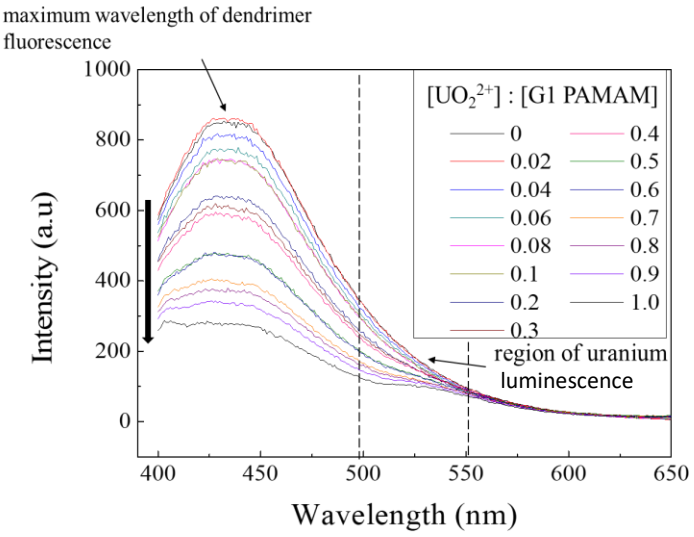

Figure 14. Fluorescence spectrum of G1 PAMAM dendrimer with varying molar ratios of uranyl ion.

The change in signal of the dendrimer at approximately 450 nm was used to construct a Stern-Volmer plot for G0-G3 PAMAM dendrimer (**Figure 15**).

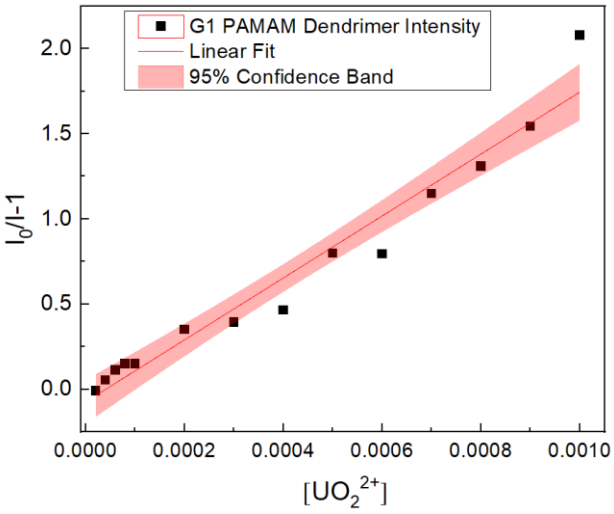

Figure 15. Stern-Volmer plot of uranyl (VI)-G1 PAMAM dendrimer complexes.

The Stern-Volmer plots show an upward trend with slight deviations from a perfectly linear trend as the ratio of uranyl ion to G*X* dendrimer increases. Some signs of minor plateaus may be seen in the figure although these are based on one or two points and are quite uncertain. As previously discussed, measurements show the principal site of binding for metal ions in PAMAM dendrimers is the tertiary amines, which are also the fluorophores with dominant quantum yield. However, other weak binding sites such as the primary amines or other internal groups can also bind the uranyl without significant quenching to the net dendrimer fluorescence.

Using these plots, the first stability constant (log β_{11}) for a 1:1 UO_2^{2+}:G*X* PAMAM dendrimer was calculated for generations 1 through 3 (**Table 3**).

Table 3. First stability constants for uranyl-PAMAM dendrimer complexes

Dendrimer Generation	First Stability Constant (log β_{11})
G0	----
G1	3.26 (0.20)
G2	3.10 (0.18)
G3	2.88 (0.45)

The first stability constant decreases as the generation increases. Although polydentate ligands usually are stronger complexing agents, more coordination sites do not necessarily result in more stable complexes. Many studies, including this one, indicate the strongest and most common binding site exists within the PAMAM dendrimers at the tertiary amines. However, the aforementioned dendritic effect has been observed to cause a change in flexibility and shape of the larger generation dendrimers. Higher generation dendrimers change from an open, extended structure to a spherical, contracted shape (**Figure 16**) .[92]

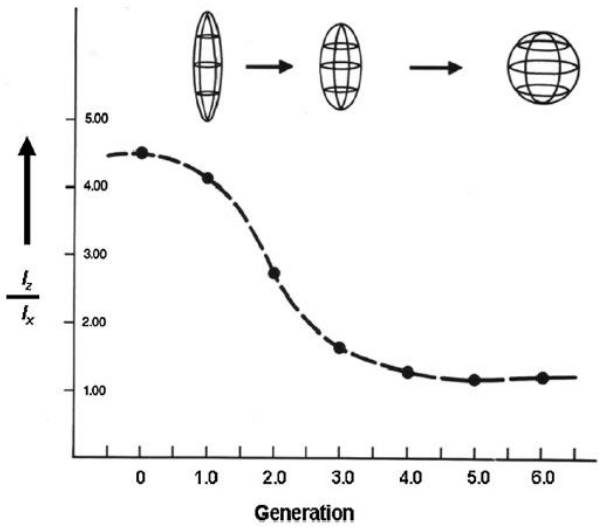

Figure 16. Structural change in PAMAM Dendrimers as a function of aspect ratio I_z to I_x. Figure generated from **Reference 32.**

Due to the change in morphology, the higher generations can experience structural hinderance, in which the interior tertiary amines are shielded by the terminal portions of their long branches as they contract into a globular shape. Therefore, although there are more numerous interior sites in higher dendrimer generations that benefit from both stronger coordination chemistry and the encapsulation effect observed in dendrimers, the steric hinderance to reach those sites could cause preferential binding of metal ions to weaker binding sites like the oxygens of amides or the terminal amines. For the 1:1 UO_2^{2+}:G*X* PAMAM dendrimer case observed here, the decrease of the stability constant with an increase in generation would correspond with steric restriction on the binding of uranyl ions. However, it is likely that there is a mixture of 1:1 complexes with uranyl ions bound to the tertiary amines and weaker sites, leading to an overall lower stability constant.

This demonstrates the stability constant can be calculated using a Stern-Volmer plot to quantify metal ion quenching of the dendrimer fluorescence. However, it is important to note that this is only a proof of concept using a ratio of one metal ion to one dendrimer molecule. In reality, the dendrimer (L) has multiple coordination sites for complexation with several (n) metal ions (M):

$$n\mathrm{M} + \mathrm{L} \rightleftharpoons \mathrm{M_nL}$$

In which case, the overall stability constant takes the form:

$$\beta = \frac{[M_n L]}{[M\}^n [L\}}$$

Studies have shown the overall stability constant of PAMAM dendrimer complexes generally increases with dendrimer generation when dendrimers are loaded with the total mole ratio corresponding to the maximum number of coordination sites.[93,94] . In addition, with so many potential donor sites, as the general structure shows (**Figure 2**), and the presence of dendritic effects, such as steric congestion for higher generation dendrimers, it is likely there is not a single predominating complex that can be predicted by simply looking at the structure.

Finally, the same experiments were repeated using Nd^{3+} as the metal ion. In contrast with uranyl-PAMAM dendrimer complexes, no quenching is observed in the dendrimer fluorescence with neodymium-PAMAM dendrimer complexes. The fluorescence signal at 450 nm remains unchanged within ± 6.5% of the average signal intensity, with no clear increase or decrease of the fluorescence signal (**Figure 17**).

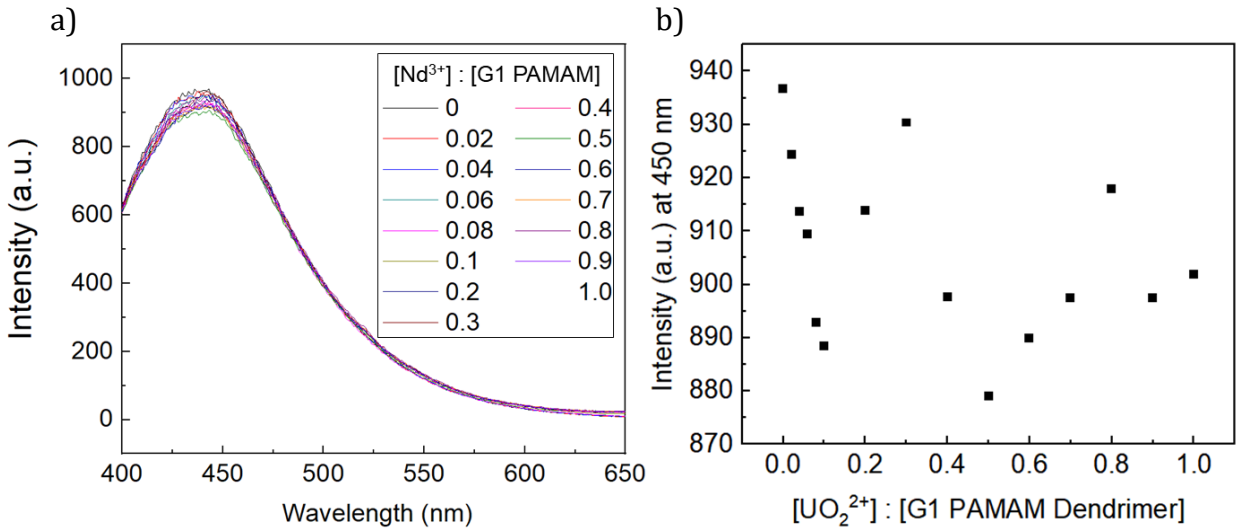

Figure 17. Fluorescence spectrum of G1 PAMAM dendrimer with varying molar ratios of neodymium ion.

There is no linear, decreasing pattern of dendrimer fluorescence intensity for generations 1-3, indicating that quenching is negligible in neodymium complexes. Oxidized tertiary amines and imidic acids in the interior of the PAMAM dendrimers are the main fluorophores, and therefore the neodymium ion is likely not found in the interior cavities of any of the PAMAM dendrimer generations.

Unlike the uranyl ion, which is difficult to analyze with absorption spectroscopy because of a large ligand-to-metal charge transfer peak, neodymium can be analyzed using UV-vis spectroscopy to monitor changes in the free Nd^{3+} concentration. For absorption experiments, samples with varying molar ratios of G*X* PAMAM dendrimer to Nd^{3+} were prepared up to a 1:1 ratio at approximately pH 7 (**Figure 18**).

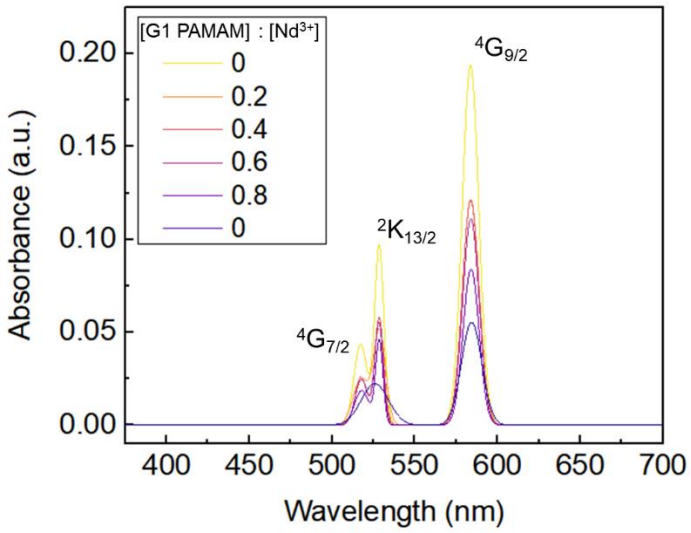

Figure 18. UV-Vis spectra for Nd3+ with varying molar ratios of G1 PAMAM dendrimer added.

There is a decrease in absorbance characteristic of the Nd^{3+} ion when complexed with generation 1-3 PAMAM dendrimers, which is indicative of either speciation or complexation. Both processes change the wavelength of absorption and thus changes the characteristic spectrum. Using a predominance diagram in conjunction with the experimental parameters (log[Nd] = -3.68, pH = 6.8 – 7.2), it is determined the primary neodymium species in solution should be Nd^{3+} (**Figure 19**).

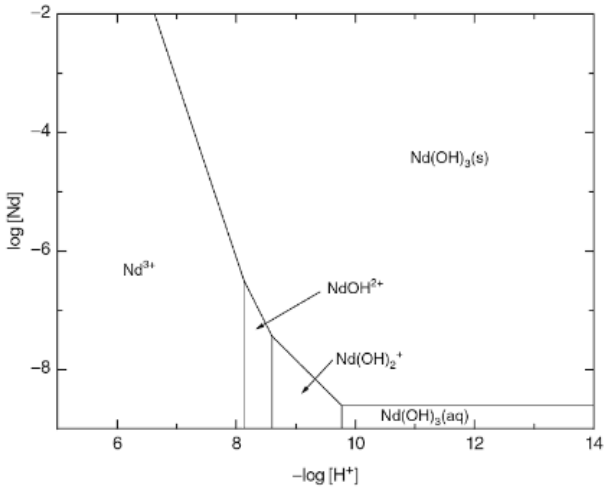

s

Figure 19. Neodymium predominance diagram at 25°C. Figure replicated from **Reference 95**.

Therefore, if speciation by hydrolysis is eliminated as a possibility, the decrease in Nd^{3+} must be due to complexation with the PAMAM dendrimers. Specifically, the coordination centers must be the primary amine sites because of the lack of quenching at the fluorescent tertiary amines and amide groups. The size of the trivalent neodymium cation is likely the reason it cannot easily be encapsulated in the interior of PAMAM dendrimers, in comparison with copper and uranyl ions which are known to complex well with internal coordination sites. Nd^{3+} has an ionic radius of approximately 1.21 –1.25 Å, whereas Cu^{2+} has an ionic radius of 0.71 –0.86 Å depending on the coordination geometry.[96] The hexavalent uranyl ion exists as a dioxo cation. Although the axial portion of the cation may be comparatively long due to the oxygen bonding (approximately 1.80 Å), the equatorial radius is contracted to 0.66 – 0.87 Å. The smaller size of the uranyl ion, in addition to an open equatorial plane, could lead to stable, polydentate internal binding with one or more branches of the PAMAM dendrimers.

5.1.1.4 Metal Ion Loading

Each PAMAM dendrimer has multiple theoretical primary and tertiary amine coordination sites (see **Table 4**), and thus could be a multidentate ligand, and is unlikely to bond to only one metal ion.

Table 4. Primary and tertiary amine binding sites available in Generations 0 through 3 PAMAM dendrimer.

Dendrimer Generation	Tertiary (Interior) Amines	Primary (Terminal) Amines
G0	2	4
G1	6	8
G2	14	16
G3	30	32

All tertiary amines, including those part of the ethylenediamine core are counted as possible coordination sites, however, steric effects including contraction (one of the dendritic effects) can naturally limit the accessibility to these sites. The larger dendrimers have so many coordination sites that they could possibly act as multidentate ligands for multiple metal ions. The possibilities for different variations of dendrimer complexes, especially those of higher generations, are so numerous that different metrics are often used to quantify complex formation. The extent of binding (EOB) is equivalent to the ratio moles of metal ion bound to the dendrimer $[M]_b$ to the total amount of metal ion in solution $[M]$.

$$EOB = \frac{[M]_b}{[M]}$$

In practice, the EOB increases with increasing metal ion added until reaching a maximum of 1, indicating 100% of the metal is complexed with the dendrimer, then decreases as an excess of metal ion is added to the solution and remains free in the solution when the dendrimer is saturated with metal ions.

In this study, fluorescence of the uranyl ion was not directly measured because of possible challenges with deconvoluting and quantifying different uranyl species' signatures in the neutral pH of the samples. However, by increasing the moles of uranium added to solution until the fluorescence of the PAMAM dendrimer is quenched to zero intensity, an approximate saturation point (EOB) can be determined (**Figure 20**). Samples with a range of molar ratios of uranyl ion to G*X* PAMAM dendrimers up to ratios larger than the total number of binding sites were prepared, to ensure an excess of uranyl ions which theoretically would saturate the dendrimer.

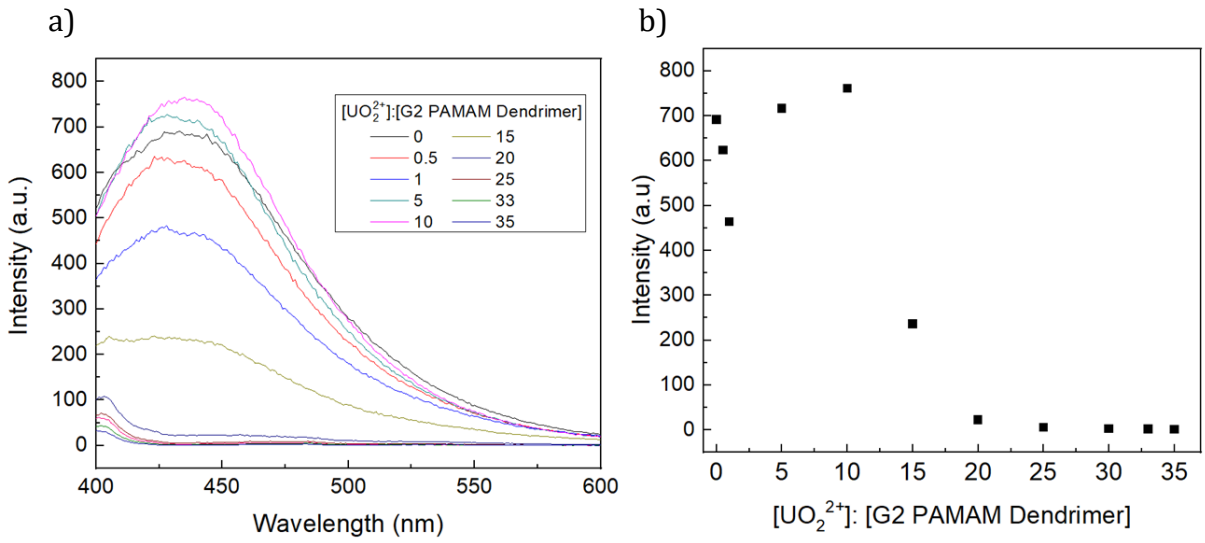

Figure 20. Quenching of G2 PAMAM dendrimer fluorescence with an excess of uranyl ions.

A yellow, gelatinous precipitate begins to visibly form at uranyl to dendrimer molar ratios greater than one, the exact ratio depending on the dendrimer. Further studies that examine the uranyl distribution between liquid and solid phase, and the exact nature of the precipitate, will be discussed later in **Chapter 4.2** and **4.4**. It can be assumed that the dendrimer fluorescence in the liquid phase will decrease whether it is due to quenching from complexation with the uranyl in the liquid phase, or physically removed from the liquid by complexing with the uranyl and precipitating as a solid. Therefore, when the dendrimer fluorescence intensity reaches approximately zero, it is an indication of full binding (EOB approximately 1) with uranyl in some form of the many possible options. The maximum amount of uranyl ion loading for each PAMAM dendrimer generation were measured (**Table 5**).

Table 5. Uranyl ion loading on G1-G3 PAMAM dendrimers.

Dendrimer Generation	Molar Ratio at Maximum Metal Loading	Total Coordination Sites
G1	5 – 10	14
G2	20 – 25	30
G3	35 – 40	62

The number of uranyl ions per binding sites for each dendrimer generation indicates that until generation three, multidentate coordination is unlikely despite the available equatorial plane on the uranyl ion that is usually the site of multidentate binding. This is consistent with other studies that have measured generation three and higher to find large

molar ratios of the uranyl ion complexed to PAMAM dendrimers. One study found 34 uranyl ions complexed with one Generation 2 dense shell PPI-based glycodendrimer, compared to only two europium (III) ions.[54] Compared with other monatomic ions of various sizes and oxidation states, the number of uranyl ions complexed to a single dendrimer was found to be more than double the number of Ni (II) ions, the next largest binding number of the ions in this study. Another study found 220 uranyl ions coordinated to a single Generation 4 PAMAM dendrimer.[42] These amalgamation of this data suggests very unique, enhanced coordination chemistry for uranyl-dendrimer complexes, especially compared to neodymium and the other lanthanides.

5.1.1.5 Effect of Ionic Concentration

Varying the concentration of the ionic medium can reveal if there is any effect of the medium on complexation and/or precipitation. The first can be investigated using steady-state fluorescence to determine if the amount of uranyl binding, proportional to the quenching of dendrimer fluorescence, would change if there are a higher or lower concentration of competing ions in solution. Identical solutions of 1:1 uranyl ion:G2 dendrimer were made in solutions with an $NaNO_3$ ionic strength of 1×10^{-5} to 5 M and the fluorescence was measured in comparison with a non-complexed G2 PAMAM dendrimer (black line, **Figure 20**).

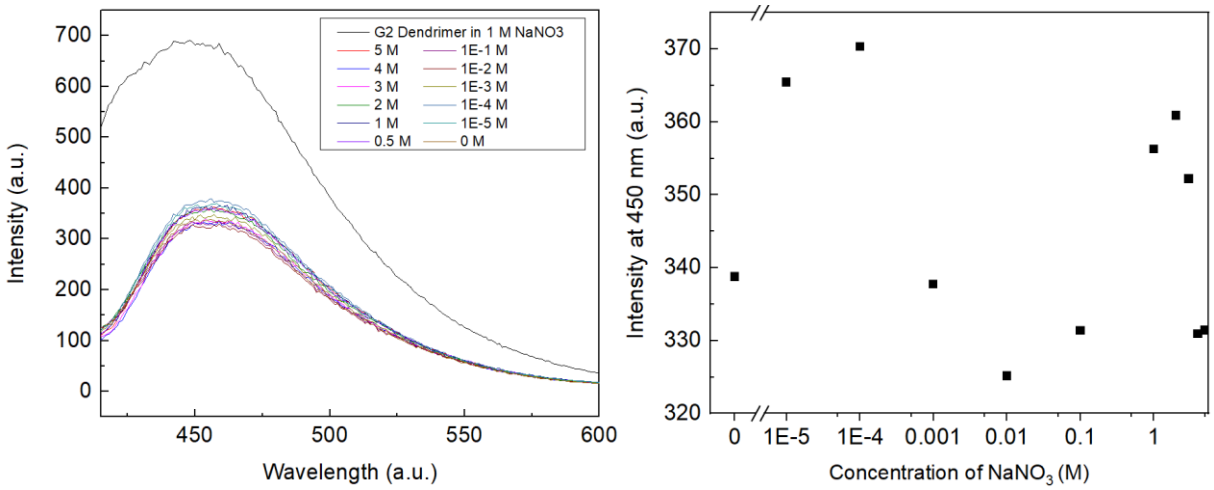

Figure 21. Fluorescence of 1:1 UO_2^{2+}:G2 PAMAM dendrimer complexes in varying ionic strength of $NaNO_3$.

There is slight variation in the maximum dendrimer fluorescence at 450 nm, however, with no clear trend and with a variation of ± 30 arbitrary intensity units from the median value. In comparison with the fluorescence intensity of the non-complexed dendrimer in 1 M $NaNO_3$, the difference among the 1:1 uranyl:G2 PAMAM dendrimer complexes is minor. This would be expected, as PAMAM dendrimers have proven to have a unique affinity for the uranyl ion and would be unlikely to selectively choose another cation, such as Na^+ to bind to.

5.1.2 Time-Resolved Fluorescence

Time-resolved fluorescence investigated the binding between the uranyl ions and the dendrimer by examining the change in the dendrimer fluorescence lifetime at different molar ratios of uranyl:G*X* PAMAM dendrimer, and if this could be attributed to static or dynamic quenching.

5.1.2.1 Fluorescence Lifetimes of PAMAM Dendrimers

PAMAM dendrimers of generation 4 and larger have been observed to have two, short fluorescence lifetime components.[65] Studies varying the temperature and pH of the PAMAM dendrimer solution have shown that some luminescence quenching can occur from collisional deactivation of the tertiary amines with oxygen as a function of temperature, but pH only affects fluorescence intensity, not the lifetime below a pH of 8. The existence of two lifetimes could indicate either a difference in the local structure of the tertiary amine, for example an ethylene diamine core amine or a branching amine, or a different fluorophore that has not yet been detected by other analytical methods. Either possibility is equally plausible, especially because the pathway to fluorescence is an energy transfer mechanism that has only been generally determined using indirect methods.[65,97] Using time-resolved fluorescence, the fluorescence lifetimes were determined for generations 0 through 3 by extracting two dimensional plots of fluorescence intensity versus time at 450 nm from the three-dimensional TCSPC data (**Figure 22** and **23**).

a)

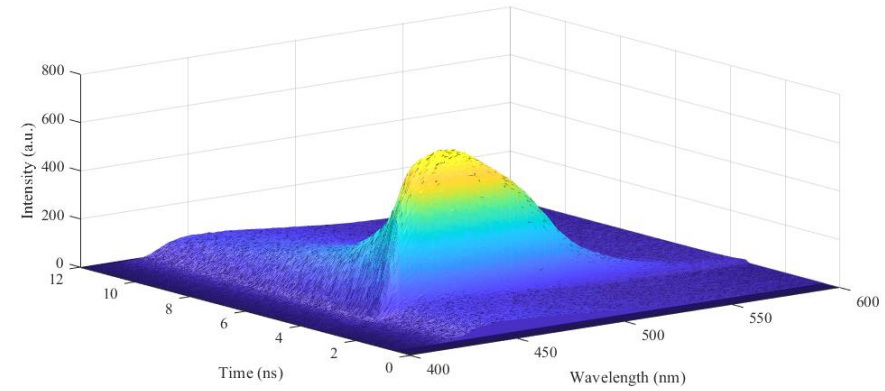

b)

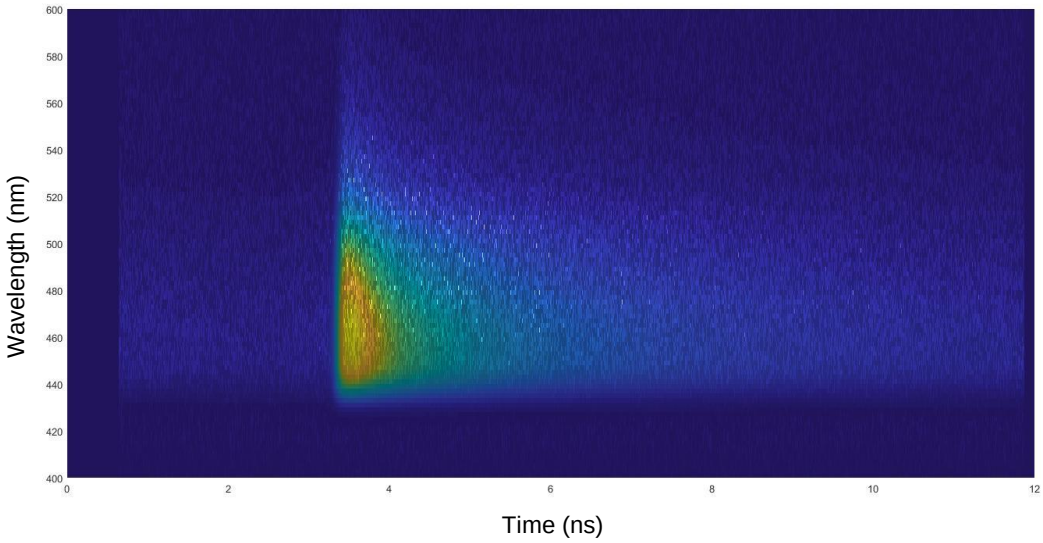

Figure 22. Three-dimensional (top) and top-down (bottom) view of a G1 PAMAM dendrimer TCSPC spectrum.

The nonlinearity of a log-linear intensity-time plot of the time-resolved data reveals that generations 0 – 3 all have multiexponential lifetimes (**Figure 23**).

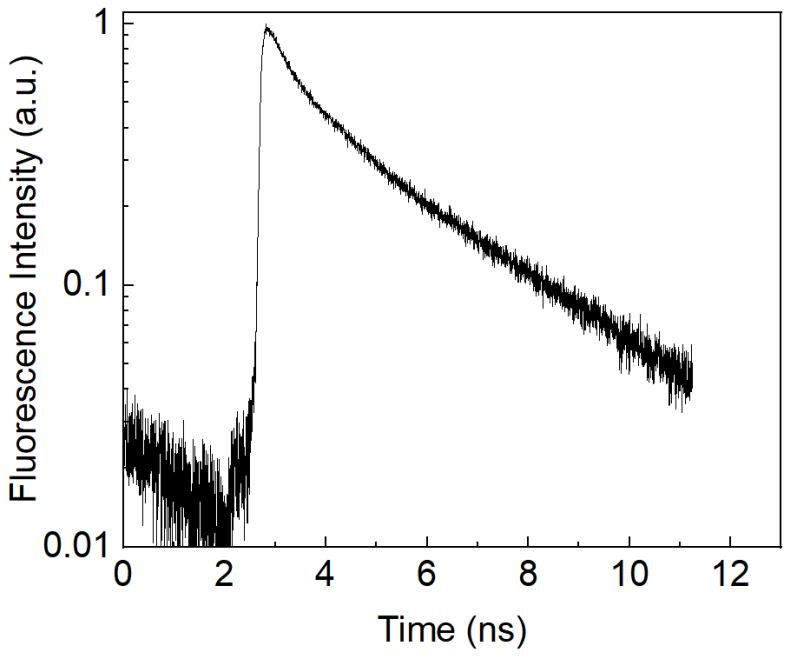

Figure 23. Time-resolved fluorescence spectrum of a G1 PAMAM dendrimer at 450 nm. Fitting the exponential curves allows the following fluorescence lifetimes to be calculated (**Figure 24**, **Table 6**).

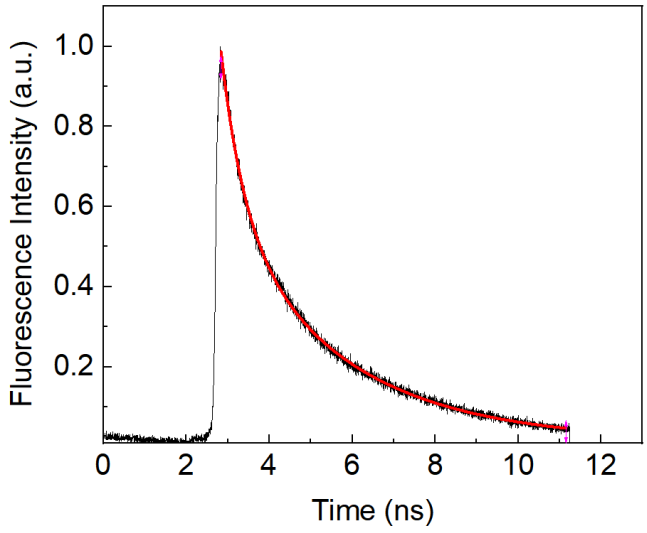

Figure 24. Biexponential decay fitting of time-resolved data for a G1 PAMAM dendrimer.

Table 6. Fluorescence lifetimes of G0 – G3 PAMAM Dendrimer.

Dendrimer Generation	τ_1 (ns)	τ_2 (ns)
G0	2.477 (0.028)	0.504 (0.008)
G1	2.461 (0.009)	0.509 (0.002)
G2	2.361 (0.040)	0.410 (0.015)
G3	2.154 (0.026)	0.369 (0.009)

The shorter lifetime could be minor fluorescence from the solvent, but it is slightly shorter with an average of 0.448 ns compared to 0.764 ns for the sodium nitrate solvent alone. Weak signal from solvent excitation and scattering not efficiently eliminated by the emission filter are often mutually detected as artifacts of complex decay lifetime fitting, especially with ultrafast measurements. Larson and Tucker have previously measured 3 lifetimes, including a background signal/artifact of a similar time, and two dendrimer fluorescence lifetimes (1.3 – 2.5 ns and 4.2 – 7.1 ns, depending on generation) for carboxylate-terminated PAMAM dendrimers denoted as G*X*.5 (*X* = 2, 3, 4, 5, 7).[97] Wang *et al*. reported two PAMAM dendrimer lifetimes, a stable 1.7 – 2.2 ns and a temperature-dependent 5.3 – 8.7 ns lifetime for only G4.[65] If the data are fit to have three fluorescence lifetimes, the lifetimes do correspond closest to those calculated by Larson and Tucker. However, the error in the lifetimes of a triexponential decay fit are so large as to be unreliable, and thus a biexponential fit is selected with one lifetime attributed to the background and one to the dendrimer.

The longer dendrimer wavelengths are not observed in these results. Other studies have shown this is highly sensitive to collisional deactivation from heat or collisional

quenching from the solvent or other ions and species in solution.[65,98] Therefore, local heating during TCSPC from repeated laser pulses in the same part of the sample, quenching from the sodium nitrate medium, or alternative de-excitation mechanisms can shorten this lifetime to be within the range of the other dendrimer fluorophore or the background, or make the quantum yield so low as to be nearly undetectable. Although we are able to distinguish the location of the fluorophore for the shorter PAMAM dendrimer lifetime due to the simplicity of generation 0, the origin of the longer lifetime (interior, non-core tertiary amines, imidic acid or a different, unknown fluorophore) continues to be up for debate.

The shorter dendrimer lifetime is highly useful to examine the complexation between the uranyl ion and the dendrimer because it appears to mostly be unaffected by the external environment, unlike the longer lifetime. TCSPS samples were the same samples used for steady-state fluorescence measurements, with increasing molar ratios of uranyl to G*X* dendrimer (**Figure 25**).

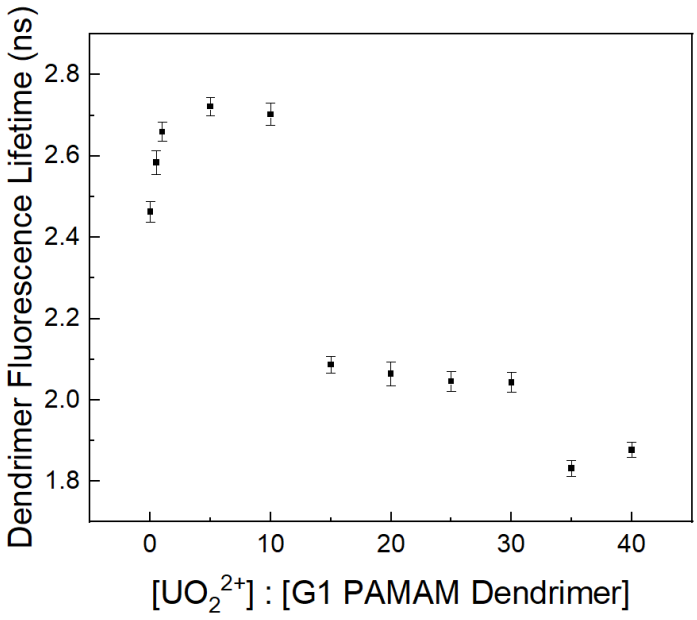

Figure 25. Fluorescence lifetime variation of G1 PAMAM dendrimer at 450 nm with increasing molar ratios of uranyl ion.

The measured lifetime of the dendrimer changes as more uranyl ions are added, however the change in fluorescence lifetime is not a linear, patterned decrease. This means the method of quenching is not necessarily dynamic/collisional. Different "groups" of lifetimes can be seen using **Figure 23** as an example, which shows the fluorescence lifetime of the dendrimer and uranyl-G1 PAMAM dendrimer complexes. First, in the 0 to 1 molar ratio range, there is a slight increase in dendrimer fluorescence. The Stern-Volmer plot and visual analysis shows complexation of uranyl and the dendrimer in the liquid phase. Normally, the fluorescence lifetime will remain the same or decrease due to additional non-radiative pathways of de-excitation. In this case, because the tertiary amine fluorescence is generally attributed to energy transfer from oxygen atoms, it could also include energy transfer from the oxygen atoms in the uranyl ion which will slightly increase the lifetime of the dendrimer if the method of energy transfer is longer than from oxygen in the

atmosphere or solution. In addition, it is likely that the amine groups are being partially protonated, which buffers the additional protons being added from the aliquot of low pH uranyl ion, which is why the pH remains approximately neutral. This could increase the lifetime and the intensity of the fluorescence.

From a molar ratio of 5 to 10, the lifetime remains nearly constant, indicating a stable complex in solution. This is aligned with the steady-state observation that the extent of binding in the liquid phase is at a maximum of 1 at a molar ratio between 5 and 10 for G1. This saturated uranyl-dendrimer complex is a ground-state complex because the dendrimer lifetime does not change significantly once the uranyl-dendrimer complex is formed, typical of static quenching. At a ratio above 10, an appreciable amount of precipitation begins to occur. The nature of this precipitation is discussed in **Section 4.2** and **Section 4.4**, but may possibly be due to cross-linked dendritic forms. Other complexes, such as liquid-phase multi-uranyl/dendrimer complexes, can still co-exist in small quantities, but above a certain molar ratio the precipitate predominates and appears to be preferred over the liquid phase complexes to the extent that the complexes will reconfigure into a precipitate at a high molar ratio.

The lifetime above a molar ratio of 10 must be solely attributable to whatever liquid-phase species or complexes are remaining in solution after some portion of the uranyl-PAMAM dendrimer complexes have precipitated. The fact that there are two discrete, nearly constant dendrimer fluorescence lifetimes (with molar ratios of 15 – 30 and 35+) indicates the presence of two ground-state configurations of the dendrimer with pathways for radiationless deactivation that shorten the fluorescence lifetime from its

intrinsic form (molar ratio = 0). This could be due to competing factors in the liquid phase of samples, such as protonation at the tertiary amine sites if the uranyl ions selectively cross-link at the primary, the accessibility of oxygen in the dendrimer cavities, or even the presence of other uranyl-dendrimer complexes that can exist in solution. Therefore, although there is evidence of a consistent, ground-state dendrimer complex in the liquid phase, the exact conformation resulting in these fluorescence lifetimes above a molar ratio of 10 is still a challenge to determine given the complexity of the coordination chemistry and existence of a second phase.

5.2. Neutron Activation Analysis

The fluorescence data show the overall decrease in dendrimer signal due to complexation, but the uranyl-dendrimer complexes can evidently be present in a liquid or solid phase. Therefore, the point at which the dendrimer is shown to be fully saturated using the dendrimer fluorescence signal does not necessarily indicate maximum separation of the uranyl ion in either phase. In liquid-solid separation, 100% binding efficiency does not correlate to 100% separatory efficiency. Maximum separatory efficiency is when nearly all uranyl ion precipitates into the solid phase while maximum binding efficiency simply indicates that uranyl has occupied all binding sites of the dendrimer, regardless of the solubility of the complex. Neutron activation analysis is a nuclear method for quantitative determination of elemental concentrations. Separating the liquid and solid phases allows the uranyl distribution to be determined as a function of several variables, such as the ratio of uranyl ion to dendrimer, dendrimer generation, absolute concentration of the uranyl ion and the ionic concentration.

.

5.2.1 Metal Ion Loading

For Generations 1 through 3, uranium separation into the solid phase increases with an increase in the uranyl:G*X* dendrimer ratio until maximum separatory efficiency (near 100%) is reached. At this point, the dendrimer has been fully saturated with the uranyl ion in such a manner that the greatest possible amount has precipitated into the solid phase. After this point, any excess uranium will remain in the liquid phase. Generation 0 PAMAM dendrimer is an exception because there are much fewer binding sites, and nearly all uranyl-G0 PAMAM dendrimer complexes separate into the solid phase with very low uranyl loading, so at higher ratios the uranium is not tangibly extracted from the liquid phase (**Figure 26a**).

a)

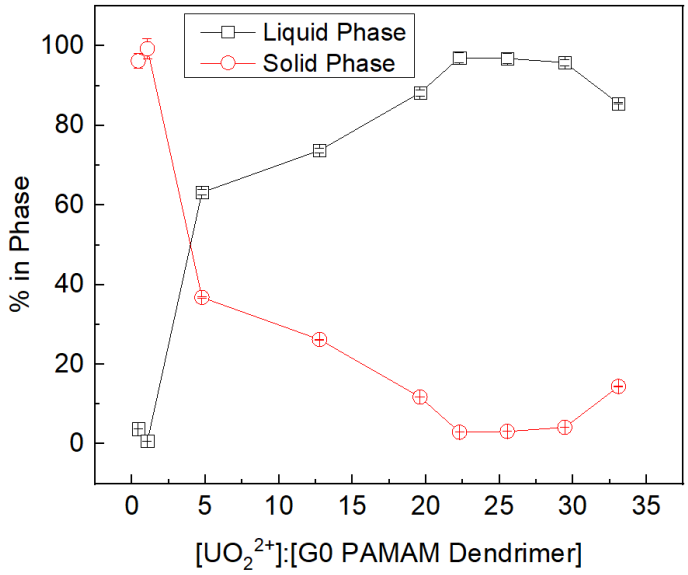

b)

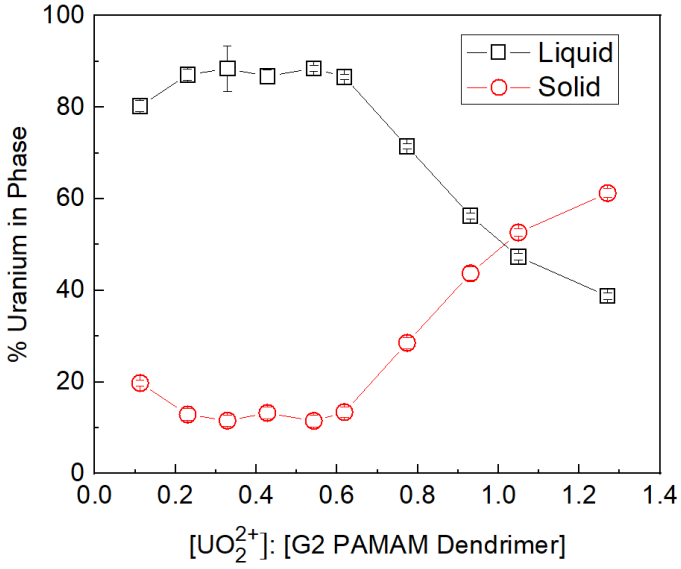

Figure 26. Distribution of uranium in the solid and liquid phase for Generation 0 (a) and Generation 2 (b) PAMAM dendrimer using NAA.

The ratio at which maximum separatory efficiency is reached is less than the maximum metal ion loading ratio/saturation point reported in **Section 5.1.1.4** (**Table 5**), likely because the dendrimer is fully saturated at some point where the uranyl-dendrimer complexes are in equilibrium between the liquid and solid phase. Consequently, as more uranyl ions are added past this equilibrium point, the uranyl remains in the liquid phase (and thus the percentage in the liquid phase increases), either as a uranium species or as a uranyl-dendrimer complex that does not precipitate into the solid phase.

NAA also reveals that a precipitate is present at low molar ratios (<0.1:1 UO_2^{2+}:G*X* PAMAM dendrimer) (**Figure 25**). Even if not visible by eye, centrifugation and removal of the liquid phase allows for NAA of the residual, imperceptible material remaining in the vial to be measured.

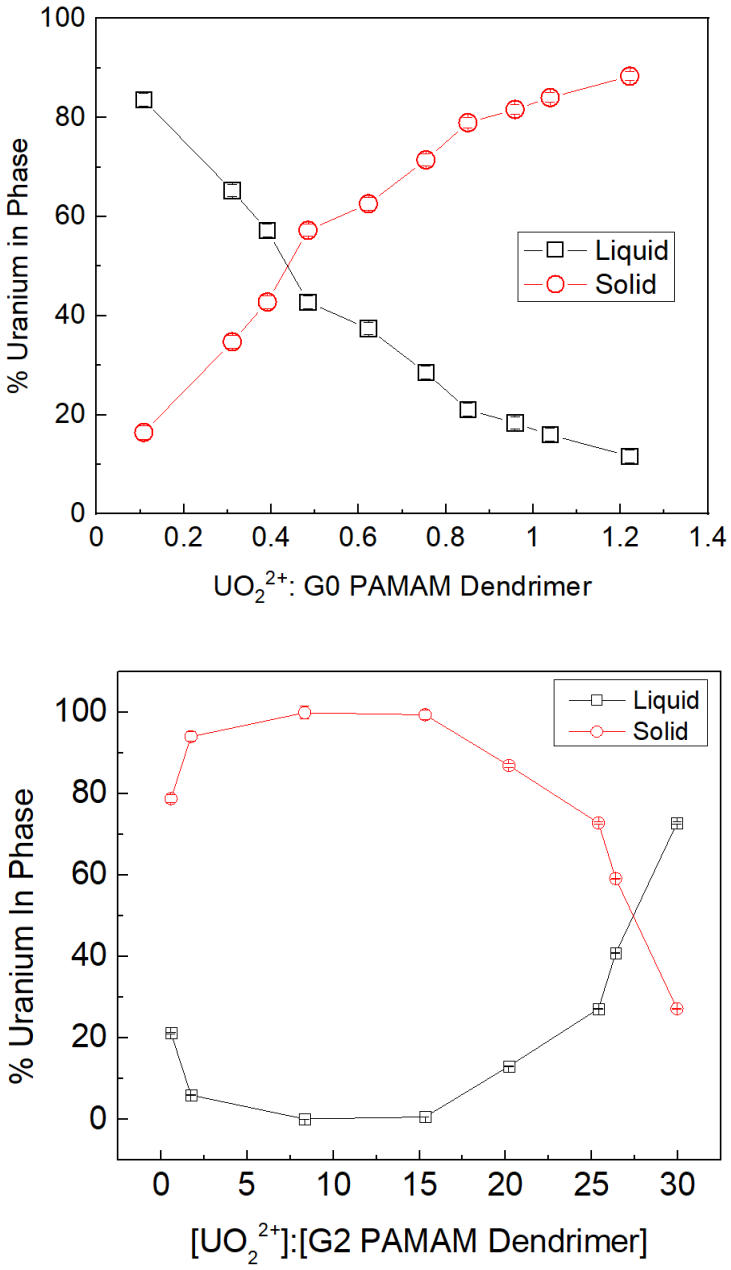

Figure 27. Distribution of uranium in the solid and liquid phase at low uranyl ion loading for Generation 2 (top) and Generation 0 (bottom) PAMAM dendrimer using NAA.

As would be expected, the transition from uranium predominantly in the liquid phase to the majority in the solid phase occurs at a lower ratio for smaller generations of the PAMAM dendrimer. The fewer binding sites in the smaller generation are saturated

with fewer metal ions, and the maximum percent of the uranyl-dendrimer complex has precipitated into the solid phase.

5.2.2 Retention Capacity

The maximum ratio at which nearly 100% of the uranium has separated into the solid phase can be translated into a mass per mass retention capacity, analogous to an adsorption/retention factor typically used to determined solid phase extraction efficiency. The mass of uranium at the given separatory ratio can be divided by the mass of dendrimer at that ratio to calculate this retention capacity (**Table 7**).

Table 7. Retention capacity (g/g) as a function of PAMAM dendrimer generation.

Dendrimer Generation	Molar Ratio at Maximum Separatory Efficiency	Retention Capacity (g uranium/g G*X* dendrimer)
G0	1	0.46
G1	5	0.83
G2	8 – 15	0.58 – 1.10
G3	10 – 12	0.34 – 0.73

There are two competing effects present as dendrimers increase in size. Naturally, as the size/generation increases, the number of binding sites increases. However, morphological changes can cause steric hinderance of metal ion binding as the generations increase (see **Figure 10**). The results observed in **Table 6** demonstrates that Generation 2 has the highest potential g/g retention capacity at a possible maximum of 1.10 g uranium/g G2 PAMAM dendrimer, but also represents the transition point where steric effects begin to limit the accessibility of the binding sites, no matter how numerous. This is in accordance with observations reported in **Figure 10**. All four generations have a high loading capacity which is expected given the number of binding sites and the unusual affinity of PAMAM

dendrimers for uranyl ions. In comparison with other sorbents and resins, meticulously compiled in Table 2 of Aly and Hamza's (2013) journal article, very few come close to approaching or exceeding the capacity of G0 PAMAM dendrimer, let alone meeting the G1 or higher end of the G2 and G3 PAMAM dendrimer capacity ranges.[20]

Table 8. Selected high-capacity SPE separatory and preconcentration sorbents for U(VI) ions. Data extracted from **Reference 20**.

Sorbent	Solid Support	Retention Capacity (g uranium/g sorbent)	Type of Sample
Amidoximated poly n-vinyl 2-pyrrolidone	Amidoxime resin	0.750	Synthetic
Acrylamido acrylic acid	Amidoxime resin	0.440	Synthetic sample at pH 6
CT/Amine	Crosslinked chitosan	0.428	Synthetic
3,4-dihydroxybenzoylmethyl phosphonic acid	Amberlite XAD-16	0.395	Synthetic
Acrylamidoxime	Amidoxime resin	0.350	Synthetic sample at pH 2
(Bis-3,4-dihydroxy benzyl)p-phenylene	Amberlite XAD-16	0.340	Synthetic

One notable pattern is that many of the highest retention capacities are those with synthetic samples, suggesting that many of these high retention capacity sorbent may be artificially high due to careful design of the experimental parameter, just as in this work. Further investigation must be done to examine how these complexants will fare in a non-simulated sample, such as groundwater, seawater, or simply any synthetic solutions with high levels of competing ions. In addition, it is noted that four of the top six sorbents are amido or amine based, indicating that the uranyl binding phenomenon is consistent with this functional group and enhanced by dendritic effects and not an anomaly.

5.2.3. Effect of Uranyl Concentration

Precipitation is typically concentration dependent on one or more species in solution. Simply examining a reaction quotient of a generic, coordination complex with multiple ions for one ligand, we would expect that the solubility would be dependent on the concentration of both species in solution.

$$M_nL(s) \rightleftharpoons nM\,(aq) + L\,(aq) \quad (32)$$

$$K_{sp} = [M]^n[L] \quad (33)$$

Thus far, the effects of dendrimer generation and the ratio of uranyl ion to dendrimer have been explored, but the absolute concentration of uranium has mainly been dictated by the ideal concentration of the species analyzed with different types of spectroscopy. 1:1 uranyl:G2 PAMAM dendrimer complexes were created with an absolute uranium concentration spanning four orders of magnitude (5×10^{-4} mM to 5 mM), see **Figure 28**.

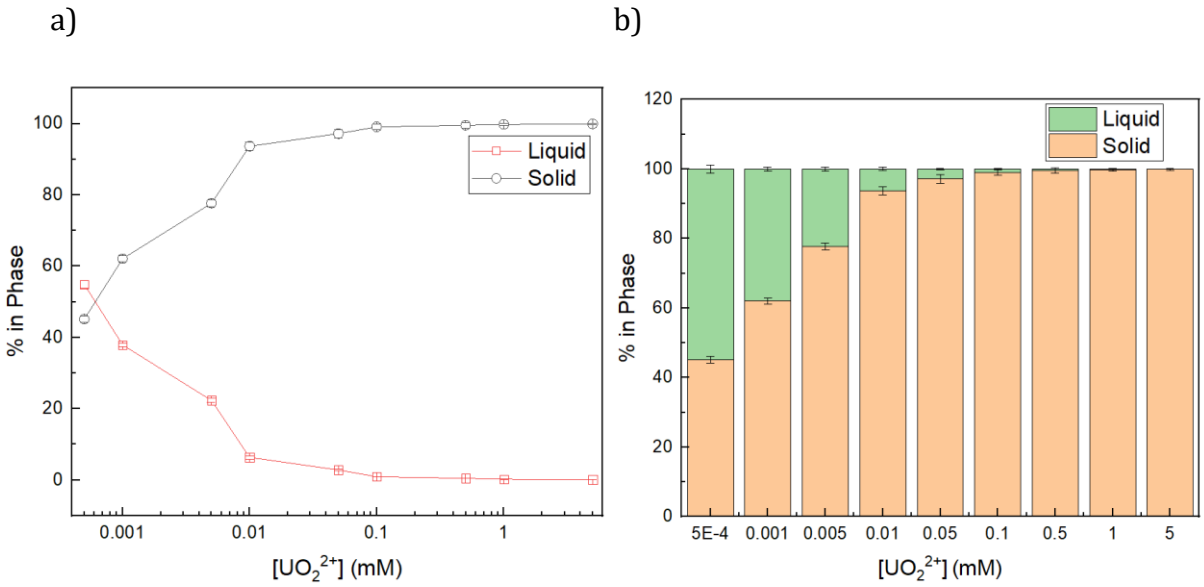

Figure 28. Distribution of uranium in the liquid and solid phase with varying absolute concentrations of uranium.

Between a uranium concentration of 0.05 - 0.1 mM, the percent precipitating in the solid phase begins to approach 99%+. This could be considered the threshold where the maximum separatory efficiency begins. Considering the amount of uranium in aqueous environmental and nuclear reprocessing conditions, this means that there must be some preconcentration phase or multiple cycles of the uranium aqueous stream contacted to a dendrimer solution for an appreciable amount of precipitation to occur. Preconcentration techniques can be physical, such as evaporation of part of the volume, or chemical, such as non-selective membranes or resins that can be used to concentrate all ions in solution.

5.2.4. Effect of Ionic Strength

NAA was used to measure the amount of uranium precipitating from 1:1 UO_2^{2+}:G2 PAMAM dendrimer solutions with varying strength of the ionic medium (**Figure 29**). The ionic strength for these solutions differed from the fluorescence experiments in that the

KNO_3 concentration ranged only from 0 – 2M KNO_3, due to the solubility in water at room temperature.

a) b)

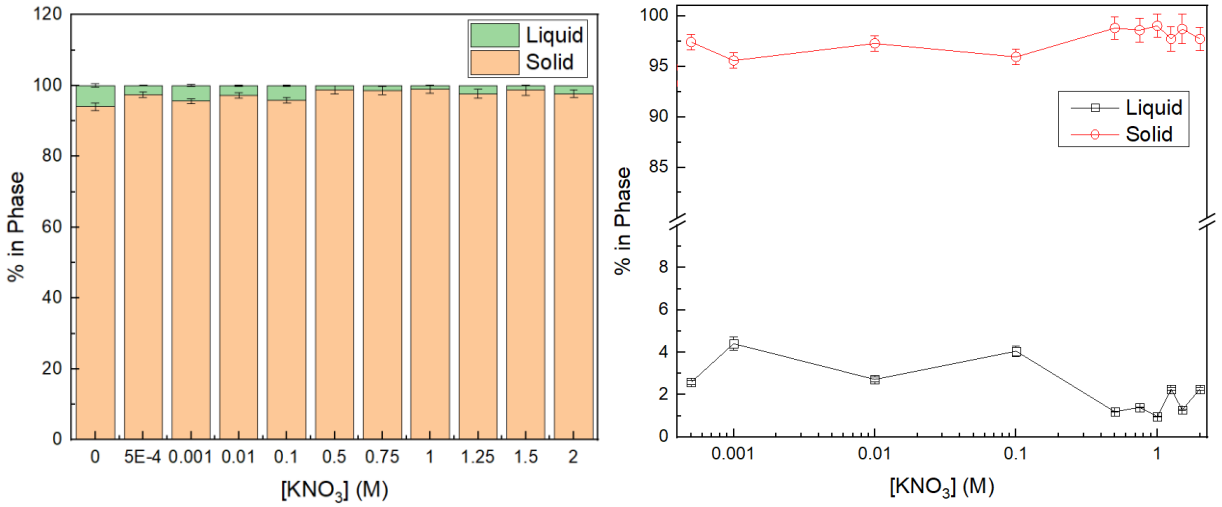

Figure 29. Distribution of uranium in the liquid and solid phase with varying concentrations of KNO_3.

Even with a smaller concentration range compared to the fluorescence experiments with a $NaNO_3$ ionic medium, it is evident that the ionic strength of the solution has no observable effect on the precipitation phenomenon in these samples. Lower concentrations (<0.5 M) of KNO_3 may have slightly lower precipitation into the solid phase, but all concentrations still precipitate approximately 95-100% of the uranium in solution, even with an ionic strength of 0 M. The trend is not significant enough to warrant further investigation.

This eliminates any possibility of a salting-out effect, where a high concentration of salt ions in solution can promote precipitation of non-electrolyte macromolecules by increasing the concentration of charged ions until the water molecules have accommodated the maximum amount of charges. The least soluble particles, macromolecules such as

proteins, large organic molecules, and importantly in this case, dendrimers, would precipitate. It is based on the Hofmeister series, which rates NO_3^- as one of the ions better for solubility of proteins, and therefore a proportionally smaller contributor to stabilization/precipitation of macromolecules and colloids compared to other ions, whereas K^+ and Na^+ have the opposite effect.[99,100] In this case, the competition of the ions seems to result in neither an increase nor a decrease in the solubility of the dendrimer. It also excludes the common ion effect, which would decrease the solubility of $UO_2(NO_3)_2$ by increasing the concentration of NO_3^- in solution from $NaNO_3$ or KNO_3 to reverse the equilibrium of dissociation of $UO_2(NO_3)_2$. Whether the NO_3^- concentration is 0 M or 2 M, the uranyl ion tends to almost entirely precipitate.

5.3 Extended X-ray Absorption Fine Structure

An attempt at examining the coordination chemistry of uranyl-PAMAM dendrimers was undertaken using EXAFS by measuring the uranium L_3 edge. A positive bump in the EXAFS region of the data was observed in the raw data for all samples (**Figure 30**). This bump is most likely due to inhomogeneities within the solution.

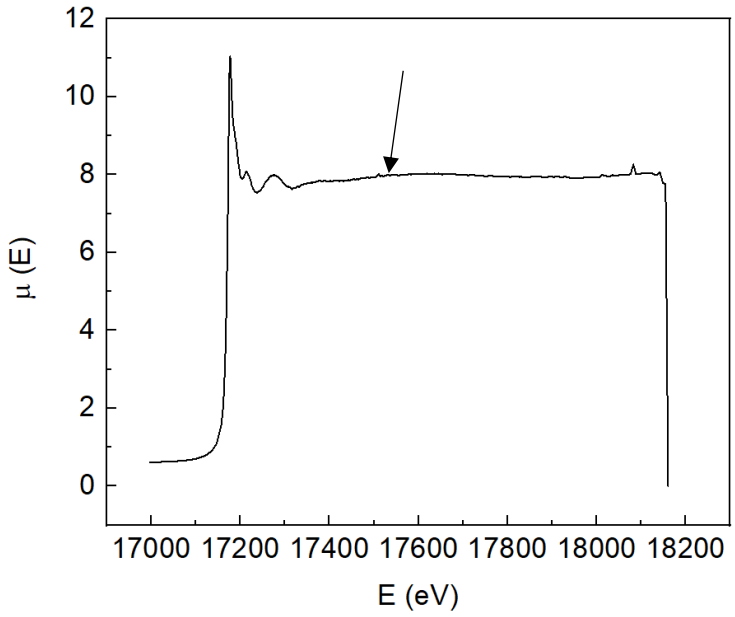

Figure 30. X-ray absorption fine structure (XAFS) of a 1:1 UO_2^{2+}:G1 PAMAM dendrimer sample. The arrow indicates the area where the "bump" was observed.

Although no precipitate or gelation was observed in the samples due to the low concentration and relatively small volume of the samples, the research discussed in prior sections shows that complexes can precipitate in solution, even if invisible to the eye. At the time of this experiment, the NAA and metal loading studies had not yet concluded with evidence of this precipitate at low concentration. If small amounts of precipitate are suspended in the solution, an anisotropic signal will be observed. Additionally, in general it is known that dendrimers, especially higher generation dendrimers, can have colloidal properties. While colloids can, and have been studied using EXAFS, they typically require immobilization on a solid support or as a solid or powdered form, precise *in situ* experimental design, or particular data analysis utilizing a modified regularization algorithm rather than the standard Fourier transform-based analysis.[101,102,103]

Presence of any second phase makes the solution inhomogeneous, which makes determination of the complex structure (including coordination number and bond distances) very challenging. The signal is an average of all structures and complexes in the sample, and the signal can change according to different local structures and phases in the sample, making the EXAFS spectrum and fits hard to deconvolute if there is more than one unknown structure. It especially affects the disorder term (σ^2) of the equation, and subsequently the amplitude of the EXAFS function $\chi(k)$.[83] However, it is important to note that even sample 1, the uranium standard, has this abnormality in the EXAFS region. This points to larger experimental challenges, such as dust or other particulate matter in the samples, or misalignment of the sample in the x-ray beam. In fact, while scanning the alignment in the horizontal direction, there were two distinct I_0 maxima, approximating a "double hump" at some point. This was noted several times throughout the experiment, as well as the observation that the beam may not have been fully on the sample, which is possible due to the fact these were new primary holder designs.

Although this may introduce more error, this is not a limiting issue for processing the EXAFS spectra. The data were fit with a *k*-range between 2.5 and 11.0 $Å^{-1}$ to exclude the bump from the data processing. A Gaussian window of 0.3 $Å^{-1}$ was applied prior to Fourier transforming. Three peaks were fit, with two fixed axial oxygens, an equatorial contribution to the uranyl, and a multiple scattering peak from the axial oxygens. The data were fit between 1.2000 to 3.5000 Å with 9.4 degrees of freedom using Stern's rule.[104] Backscattering was calculated with the FEFF code. Examples of fitting the EXAFS data of Sample 7 and 8 can be seen below (**Figure 31**, **Table 9**).

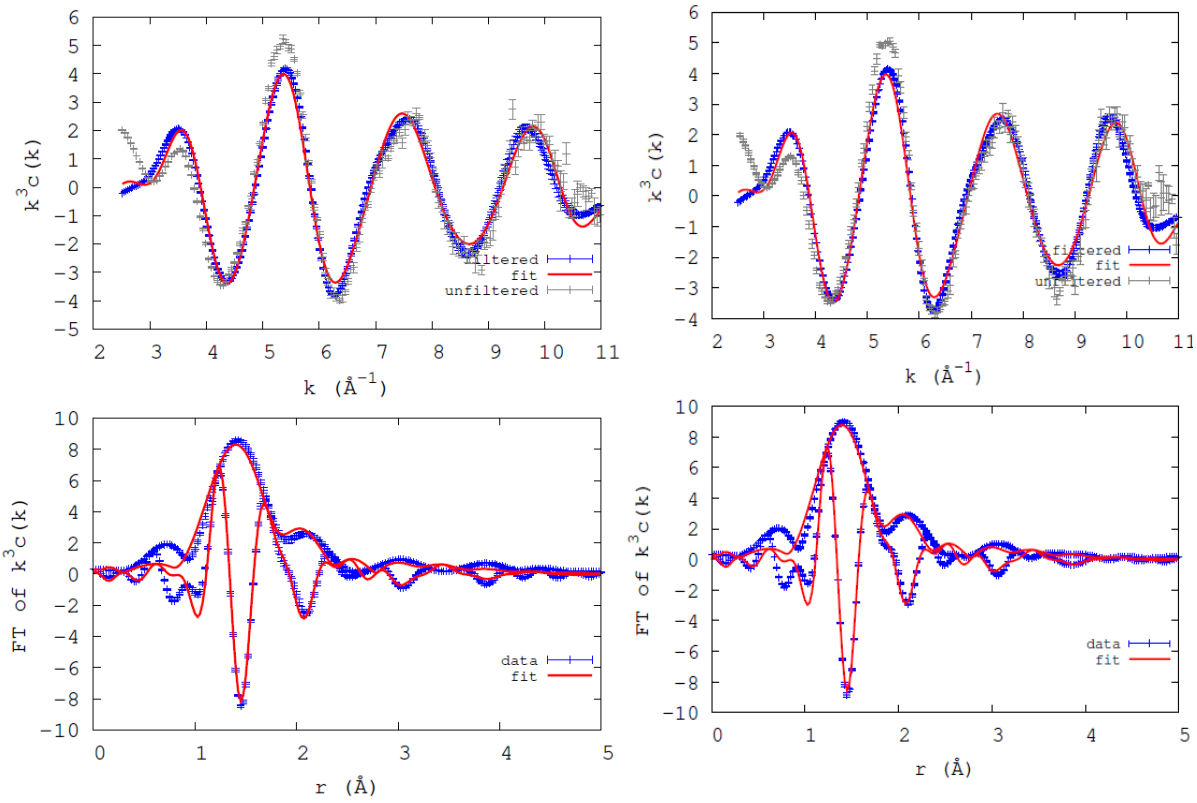

Figure 31. The uranium L_3-edge EXAFS spectra (top) and Fourier transformed spectra (bottom) of Sample 7 (left) and Sample 8 (right).

Table 9. Results for the coordination number (*N*), Debye-Waller factors (σ^2), and Bond distances (*R*) from data fitting of the EXAFS Spectra for Sample 7 and 8. Note: the amplitude reduction factor (S_0^2) was held constant at 1.000 during the fitting process.

	Sample 7			Sample 8		
	N	σ^2 (Å^2)	R (Å)	N	σ^2 (Å^2)	R (Å)
U-O Axial	2	0.0021(6)	1.782(5)	2	0.0015(7)	1.781(5)
U-O Equatorial	6 (2)	0.021(7)	2.35(1)	7 (2)	0.024(8)	2.36 (2)
Multiple Scattering Peak	1	0.010	3.576	1	0.010	3.574
ΔE_0		-21.0			-21	
S_0^2		1.000			1.000	
R (%)		15.09			15.82	

In the case of the uranyl ion, the two double-bonded oxygens in the dioxo structure occupy the axial spots, so binding primarily occurs in the equatorial plan. Overall, the

coordination number along the equatorial plane of the uranyl ion determined by the EXAFS fit ranged from about five to seven (**Figure 32**). The Debye-Waller factor for the equatorial bonded atoms was relatively large for all samples. This indicates a high amount of disorder in the equatorially bonded atoms, which is to be expected when considering the numerous possible coordination sites and resultant structures of the complexes, including possible second phases or other inhomogeneities. No clear trends were observed with variations in generation or metal loading.

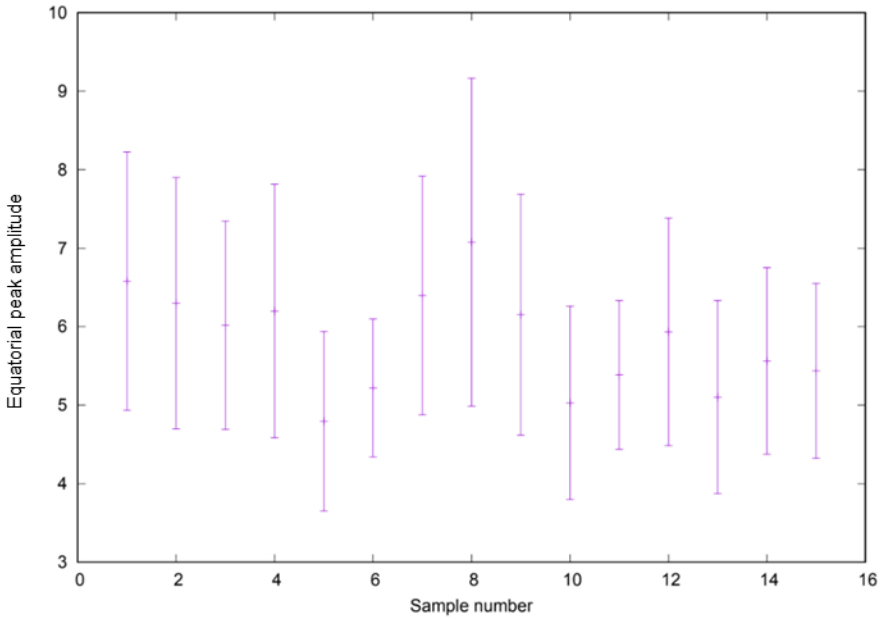

Figure 32. Equatorial coordination number of uranyl ion determined by EXAFS.

EXAFS measurements of copper-PAMAM dendrimer complexes have proposed two octahedral complexes: one structure having copper bound to four tertiary PAMAM dendrimer amines complexed along the equatorial plane and two water molecules bound

along the axial plane, and the second structure having copper bound to two tertiary PAMAM dendrimer amines and two nitrate ions along the equatorial plane, and two water molecules along the axial plane.[55] Drawing parallels to the uranyl ion, the two water molecules in the axial plane proposed in the copper-PAMAM dendrimer structure would be replace by the axial oxygen atoms, and the equatorial plane of the uranyl ion would be replaced by some coordinating species. The equatorial plane of the uranyl is known to coordinate between four to six atoms, with the five-coordinated form apparently being most favored in aqueous solutions.[105,106,107] Multidentate ligands have been shown to force a "congested" six- or seven-coordinate binding, particularly in "sterically demanding bi- and terdentate nitrogen ligands", and also in longer, more flexible diglycoamide (DGA)/alkyl amine chains.[108,109] Thus, it is possible that equatorial coordination numbers of about five to seven are indeed accurate, especially in comparison with the DGA binding schemes.[109] Depending on the size of the dendrimer, which is indicative of the number of coordination sites, these five to seven bonds could be to primary or tertiary amines, water molecules or trace nitrate ions.

It is nearly impossible to separate the binding between the uranyl ion with oxygen or with nitrogen in the inner coordination sphere. Nitrogen and oxygen have similar electron configurations which results in a small difference in backscatter amplitude, making it almost impossible to distinguish between the two. However, by taking advantage of a slight difference (~0.3 Å) in the bond lengths between the equatorially bonded nitrogen (from the dendrimer) and the equatorially bonded oxygen (from water), another

attempt at fitting the data with an additional distinction between the two bond lengths may give more specific insight into the structure of these complexes.

Run 011, which was Sample 5 with a uranyl:G3 PAMAM Dendrimer ratio of 1, differed from the other samples in a few aspects. No bump was observed in the pre-processed EXAFS spectrum as was observed in the other runs. Therefore, the fit could be extended to a *k*-max of 15 $Å^{-1}$. There could be evidence of less coordination in the inner shell due to a very slight (less than 1 Å) increase in the U-O equatorial bond length compared to all other runs. Visibly, the second peak was seen to split into two separate peaks, and a new U-C peak was fit with a bond length of 2.91 Å, which is longer than the equatorial atoms in the first shell and could be found outside the inner sphere (**Figure 33**). The carbon atom was chosen in accordance with a fit found in the literature, but it could also be an oxygen or nitrogen atom.

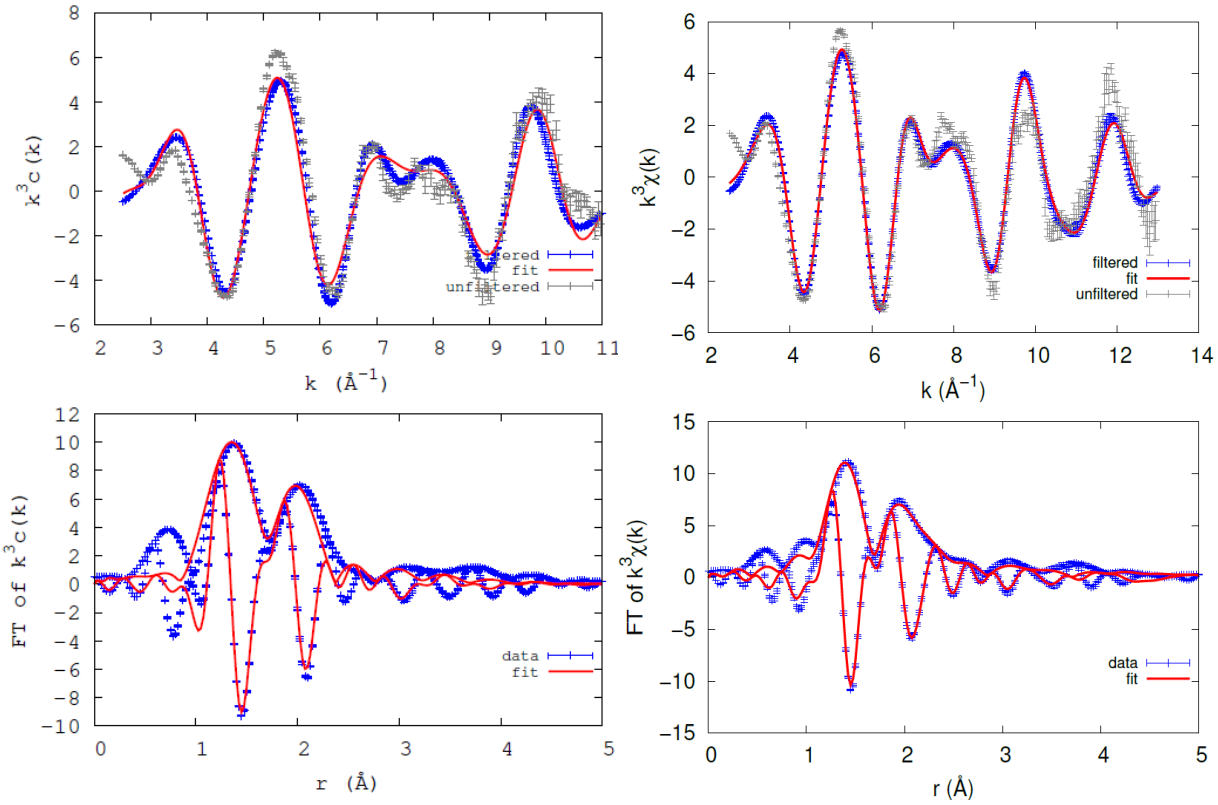

Figure 33. EXAFS spectra fitting for Sample 5 with three (left) and four (right) fit peaks in the.

A fourth peak was added to the fit parameters of the other 14 runs to determine if there could be interactions between uranium and another uranium or carbon or any other atoms with longer bond distances than the local oxygen and nitrogen atoms. However, the bond distances would converge to be within a few tenths of an Angstrom of the bond distances of the oxygen/nitrogen in the first shell, which indicated that it was unlikely that the uranyl ion was bonding strongly and consistently with any atoms outside of the inner coordination sphere. This would normally eliminate any patterned uranyl extended structures in the area observed, including metal-ion assisted crosslinking or attached dimers, trimers, etc. of the uranyl-G*X* PAMAM dendrimer complexes. However, a few of the

runs had a very flat second peak (U-O equatorial fit). This could indicate that if the bump in the EXAFS region was resolved, other runs may have had the equatorial fit peak split into two peaks when the Fourier transform is applied to transition from *k*-space to *R*-space, with one being an outer shell coordination and one being an inner shell coordination.

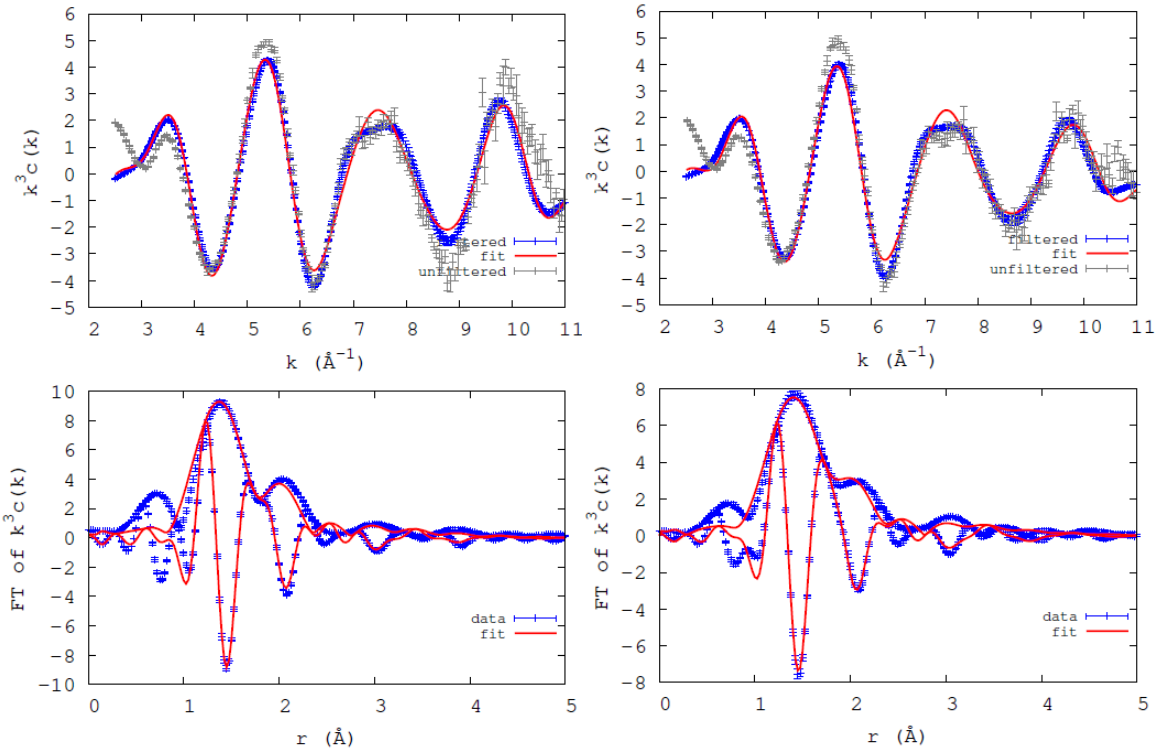

Figure 34. Sample 10 (left) and Sample 12 (right). Examples of flat peaks in the EXAFS spectra that could transform into two peaks after Fourier transform from *k*-space to *R*-space.

Although the coordination numbers and distance may be valid for the uranyl-ion dendrimers, the disorder of the solution, including multiple possible complexation schemes and possible second phase formation, makes the data challenging to interpret. Careful design to avoid the bump in the EXAFS region, including lowering the concentration of the uranium, trying other primary sample holders, and other *in situ* experimental procedures

appropriate for colloidal mixtures would be beneficial. In addition, small-angle x-ray scattering is a useful technique to quantify the shape, structure, distribution, and aggregate behavior of liquid nanoparticle dispersions or colloids, which is most likely the form of the uranyl-PAMAM dendrimer complexes. This could be explored in the future.

5.4 Dynamic Light Scattering

Dynamic light scattering can measure the distribution of differently sized particles in solution. This can give insight to the method of complexation, given that the particles involved are large enough. Because precipitate was observed in the uranyl-PAMAM dendrimer samples in such a way that complicates liquid-phase analysis, a technique like DLS which is particularly suited to observe the precipitate is highly useful. PAMAM dendrimers have diameters in the single (Generation 0 to 8), or tens (Generation 9 and above) of nanometers range, and are typically monodisperse compared to other types of polymers. Molecules of this size can be measured with DLS. Relevant to this work, a generation 2 PAMAM dendrimer has a theoretical diameter of approximately 2.9 nm.[110] A solution of 1 mM Generation 2 PAMAM dendrimers in 1 M $NaNO_3$ was analyzed with DLS (**Figure 35**). The results showed a peak at an average of 3.014 ± 0.618 nm and one peak at 703.0 ± 126.2 nm which were consistent over three trials.

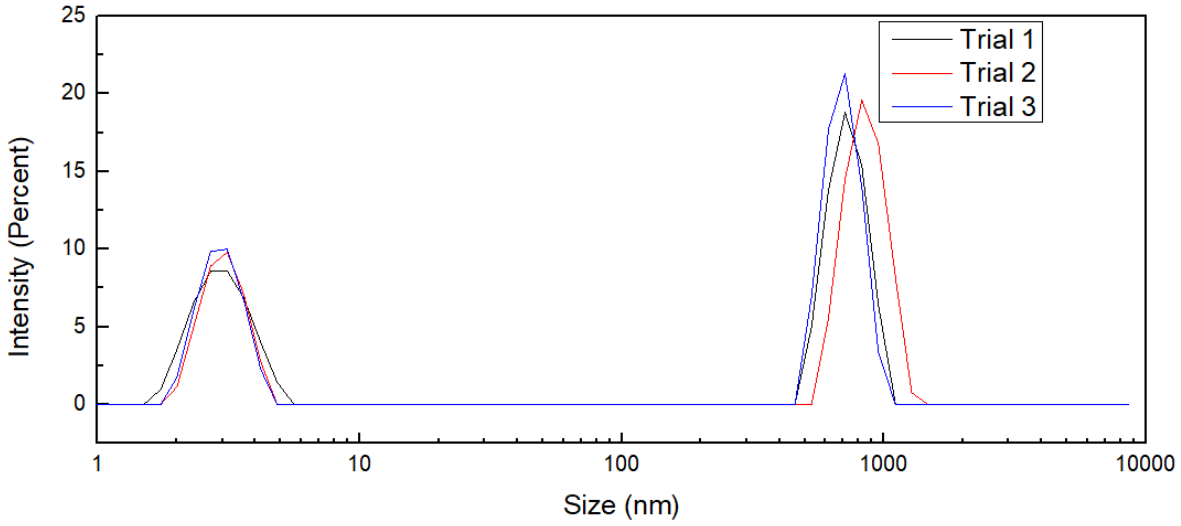

Figure 35. Size distribution of particles in a 1 mM G2 PAMAM dendrimer solution.

The peak at approximately 3 nm corresponds to the G2 PAMAM dendrimer, while the 700 nm peak was a contaminant from the nanopure water. The peak from the solvent could not be reliably removed even with a 0.45 µm Whatman polyviylidene difluoride (PVDF) Luerlock syringe filter or a 0.2 µm PVDF Chromafil Luerlock syringe filter. At times, the filter would introduce more small particulate matter even after flushing several times with water or filtering the samples up to five times. In addition, the small size of the PAMAM dendrimer poses a challenge for the data to be represented by an intensity distribution given this contamination. Large particles scatter light with intensity many times higher than smaller particles because the intensity is proportional to the sixth power of the radius.[111] If the distribution is represented as a function of volume, taking into account that the smaller particles scatter proportionally less light, then the solvent peak is much less significant (**Figure 36**)

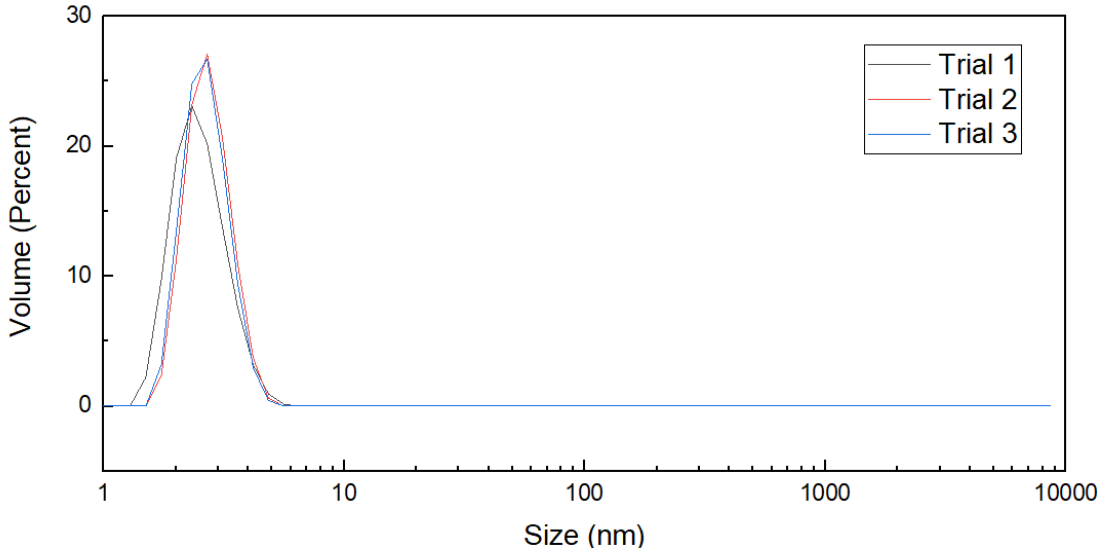

Figure 36. Volume distribution of 1 mM PAMAM dendrimer solution in 1 M NaNO3.

However, this volume distribution should only be used a verification that the majority of particles in solution are the small dendrimer particles, as it uses many assumptions such as the particles being perfectly spherical and dilute in the solvent, high accuracy of the optical properties of the solvent and the solute and that particles are homogeneous, and therefore may not translate the intensity to the volume with high reliability.[112]

Nevertheless, the peak at 3 nm can be monitored for changes, as well as any new peaks in the distribution. An increase in the diameter of the G2 PAMAM dendrimer or new peaks representing dimers, trimers, or larger aggregates of the PAMAM dendrimer would be evidence of complexation or larger supramolecular interactions such as cross-linking. With a small addition of uranyl ion (0.1:1 UO_2^{2+}:G2 PAMAM dendrimer), the diameter of the dendrimer increases. The sample was left to equilibrate overnight before measurements were carried out on the DLS instrument (**Figure 37**).

.

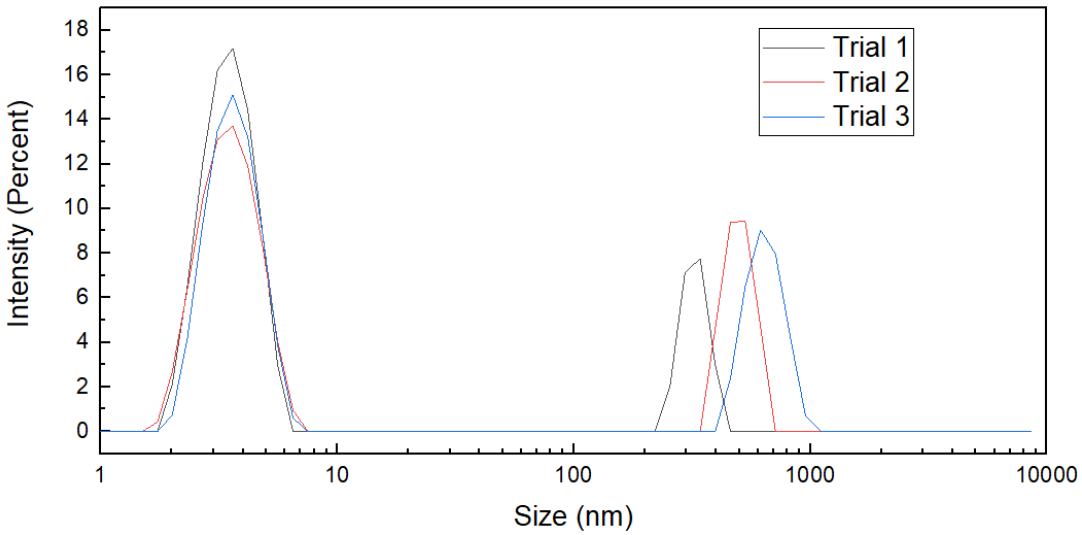

Figure 37. Size distribution of 0.1:1 uranyl:PAMAM dendrimer after equilibrating overnight.

The average size over three trials shifted from 3.014 ± 0.618 nm to 3.611 ± 0.923 nm. A two sample t-test gives a p-value less than 0.05 and indicates we must reject the null hypothesis that the size distributions of 1 mM G2 Dendrimer (M = 3.014, SD = 0.081) and the size distributions of the 0.01:1 uranyl:G2 PAMAM dendrimer sample (M = 3.611, SD = 0.0348) are the same population. Therefore, we can assume the difference between the two sizes are significant enough for them to be considered two separate populations, and the average size has shifted from approximately 3 nm to approximately 3.6 nm.

The size increase of 0.6 nm can be interpreted two ways based on the principles of DLS. DLS is based on the interpretation of scattered light from random, Brownian motion of spherical particles in solution. The uranyl ion is long along the axial axis, with each U=O bond being approximately 0.180 nm, however the equatorial diameter is only as large as twice the U(VI) radius, which is 0.087 – 0.100 nm depending on the geometry.[113,96] Therefore, the hydrodynamic diameter would only approach an increase 0.6 nm at the

maximum if two uranyl ions were oriented such that the axial portion of the uranyl ion was oriented with one oxygen toward the nucleus and one toward the exterior in all the dendrimers present in solution, which is unlikely. So, the increase in hydrodynamic diameter from the addition of the uranyl ion can be an additive effect from the physical size as well as the mass of the uranyl ion. The uranyl ion is one of the heavier polyatomic ions at approximately 270 g/mol. One or more of these ions can slow down the Brownian motion of the dendrimer, making the dendrimer appear larger by moving slower through the incident beam. In general, the mass of spherical particles is proportional to size according to the Rayleigh approximation, part of the Mie theory that the DLS software uses to determine the intensity-weighted distribution.[114]

The second interpretation is that there are non-spherical aggregates of PAMAM dendrimers. If a uranyl ion is complexed to a terminal amine group from one dendrimer and an amine group of another dendrimer, this could link two or more dendrimers together. This is a phenomenon called cross-linking, seen between polymer functional groups and metal ions, and has been utilized for applications like crosslinked hydrogels.[115] If the resultant grouped particles are not spherical, the diameter will be an average of the sizes in all three dimensions of the aggregate. The apparent hydrodynamic radius in this case lies between 3 and 6 nm, meaning the DLS could be interpreting some dimers as simply one particle with increased radius.

A sample with a molar ratio to 0.5:1 UO_2^{2+}:G2 PAMAM Dendrimer, the point where precipitate becomes visible to the eye, was also analyzed with DLS. Samples with higher concentrations of uranium were both too opaque and too unstable with the precipitate to

produce meaningful and replicable samples. When the sample is first pipetted into the cuvette, an unstable third peak can be observed and the apparent size of the dendrimer varies (**Figure 38**).

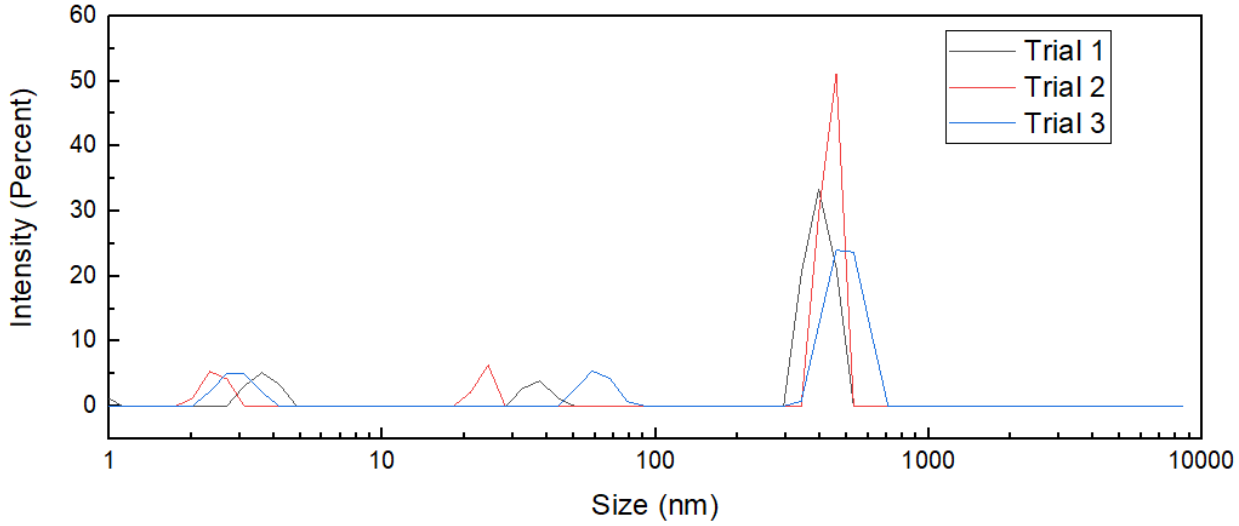

Figure 38. Size distribution of 0.5:1 uranyl:PAMAM dendrimer upon agitation.

This third peak may be transient aggregates of uranyl-dendrimer complexes or potentially even a metal ion cross-linked aggregate. The size variation (~20 to 70 nm) indicates that these are likely different particles moving in and out of the path of the incident beam, rather than a single aggregate observed in different spatial orientations. However, when the sample was allowed to settle in the cuvette, the third peak disappears, and the dendrimer size stabilizes (**Figure 39**).

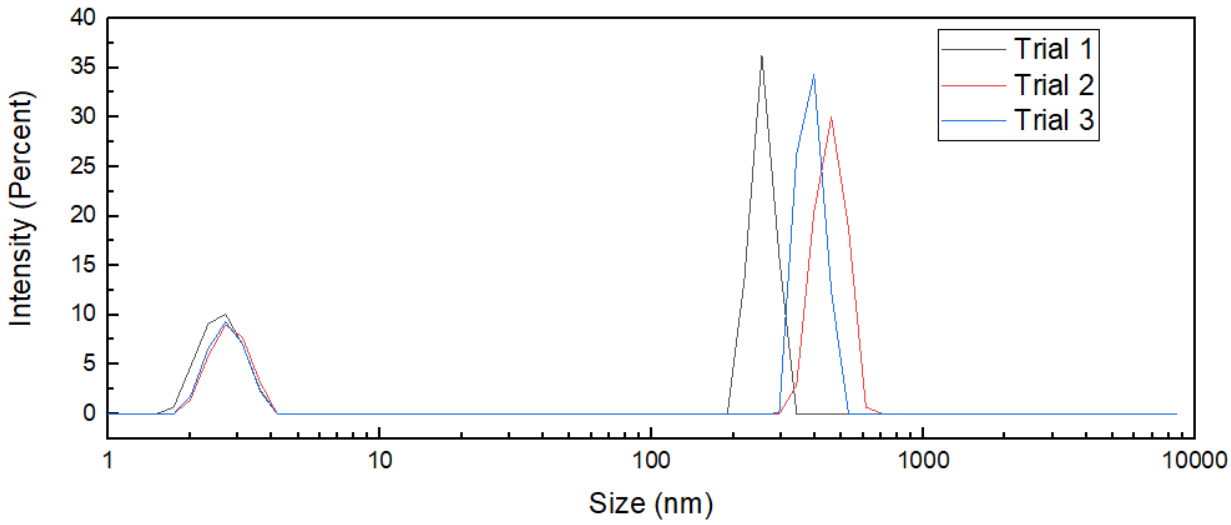

Figure 39. Size distribution of 0.5:1 uranyl ion:G2 PAMAM dendrimer after settling in cuvette.

Noticeably, the size of the dendrimer has not increased, but the intensity of the peak in both **Figure 38** and **Figure 39** has decreased compared to **Figure 37.** It is logical that this indicates the particles making up the precipitate have settled to the bottom of the cuvette, and the remaining signal is from free, uncomplexed dendrimer. This is consistent with earlier discussed fluorescence data which showed there was fluorescence signal from the PAMAM dendrimers at molar ratios of 0.5:1 that had not been quenched via complexation with the uranyl ion. Additionally, by observing the origin and evolution of this third peak over time, the kinetics of the formation of precipitate can be studied.

An aliquot of uranyl nitrate stock solution in 1 M $NaNO_3$ was added to a solution of G2 PAMAM dendrimer in 1 M $NaNO_3$ such that the final ratio would be 0.5:1 uranyl:G2 PAMAM dendrimer, with the PAMAM dendrimer having a concentration of 1 mM. The G2 PAMAM dendrimer stock solution was already in a disposable cuvette within the DLS apparatus. Size distributions were collected immediately upon addition of the uranyl stock solution and approximately every two and a half minutes thereafter. The cuvette was not

moved during the experiment, nor was the sample physically mixed. Immediately after the stock solution was added, the signal was highly irregular and trended toward very large particles (>1000 nm). After 2.5 minutes, the distribution began to stabilize with one large particle at about 2930 ± 1 nm and one smaller particle at approximately 282.4 ± 0.1 nm (**Figure 40**).

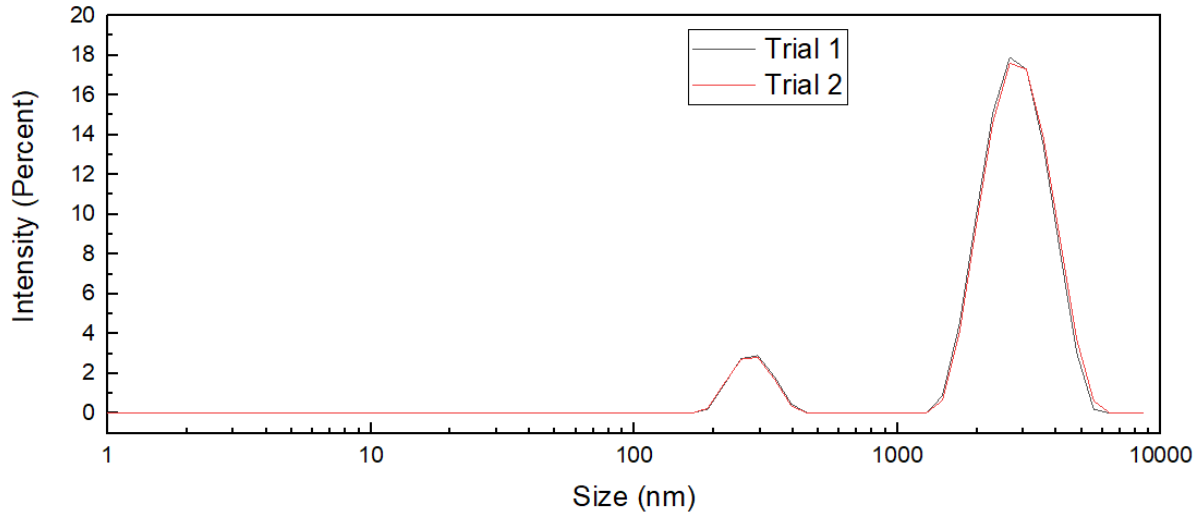

Figure 40. Size distribution 2.5 minutes after addition of the uranyl nitrate stock solution.

The nature of these two peaks are not immediately clear, however, it does appear that the addition of the uranyl ion does not slowly cause the increase of the dendrimer's hydrodynamic radius, nor does it slowly catalyze aggregation over time. Rather, it appears that there is some massive cluster that initially forms when the uranyl ion is added.

PAMAM dendrimers are technically charged on the interior at neutral pH, for example, a G1 PAMAM dendrimer has a calculated bare charge of +8.[116] However, nearly all the terminal groups are deprotonated and thus can still have an attractive interaction with positively charged uranyl ions. And because of the interior protonation, at neutral to high pH, PAMAM dendrimers are considered to have a "dense core" and therefore initial

interactions most likely take place on the surface before the system establishes equilibrium.[117] One of the observed particles could actually be a mass of electrostatically attracted ions and dendrimers initially created within the solution, whereas the other is likely an artifact of the contamination in the solution. Due to the size of the dendrimer, it is likely that the smaller particle represents this aggregate.

As time passes, the largest unstable particle begins to decrease in size and smaller, transient peaks in the tens to hundreds of nanometer size range are observed temporarily before disappearing or changing in size from one measurement to the next (**Figure 41**).

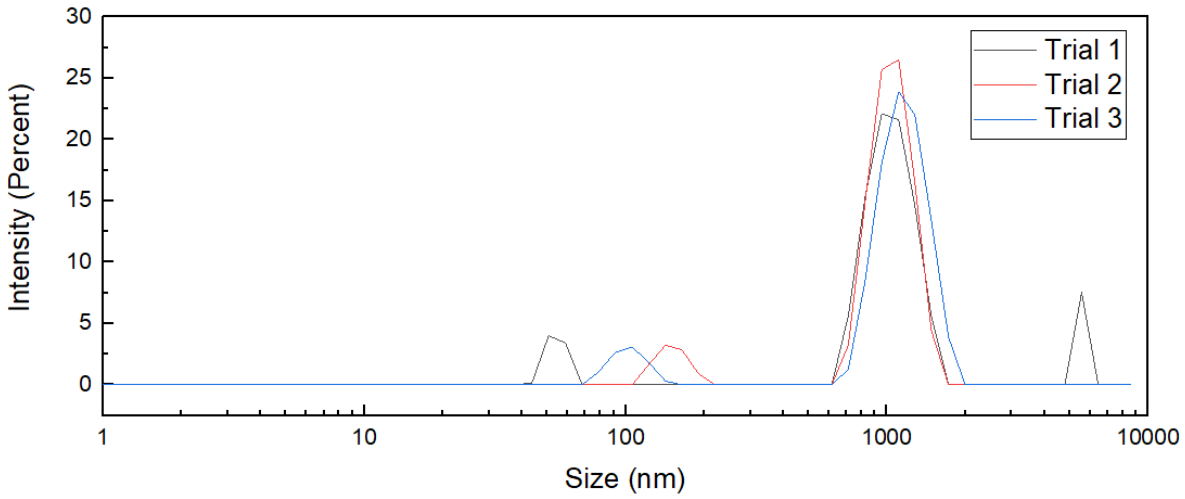

Figure 41. Size distributions at approximately 73 minutes showing the presence of unstable peaks in the tens to hundreds of nanometers range.

After about 1 hour and 45 minutes, particles with sizes in the single nanometer range begin to consistently appear, representing the G2 PAMAM dendrimer or multiples thereof, however, the larger unstable peaks representing the aggregates are still observed sporadically in some measurements (**Figure 42**).

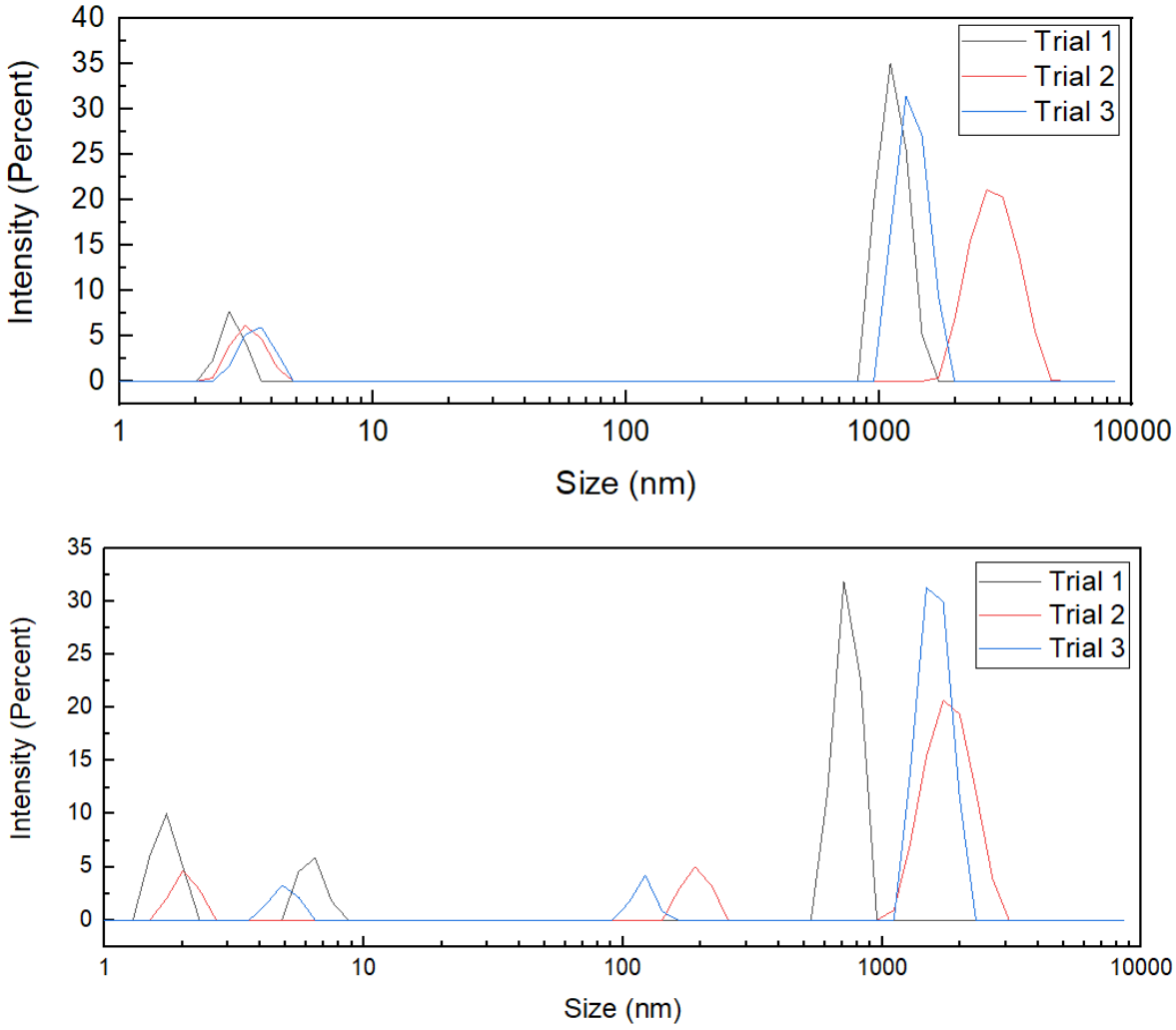

Figure 42. Comparison between the size distribution at 1 hour and 45 minutes (*top*) which includes the dendrimer peak, and the next measurement at 1 hour and 48 minutes (*bottom*).

Once again, it is important to note that intensity is related to the size of a particle to the sixth power, so at this point, a large portion of the particles in the solution are the small and intermediately sized particles. This pattern of stability remains consistent until about 6 hours and 38 minutes, when the size of the G2 PAMAM dendrimer begins to stabilize and intermediately sized peaks are no longer observed. By the next day, the size distribution

resembles that of **Figure 39**, which is an undisturbed 0.5:1 UO_2^{2+}:G2 PAMAM dendrimer sample (**Figure 44**).

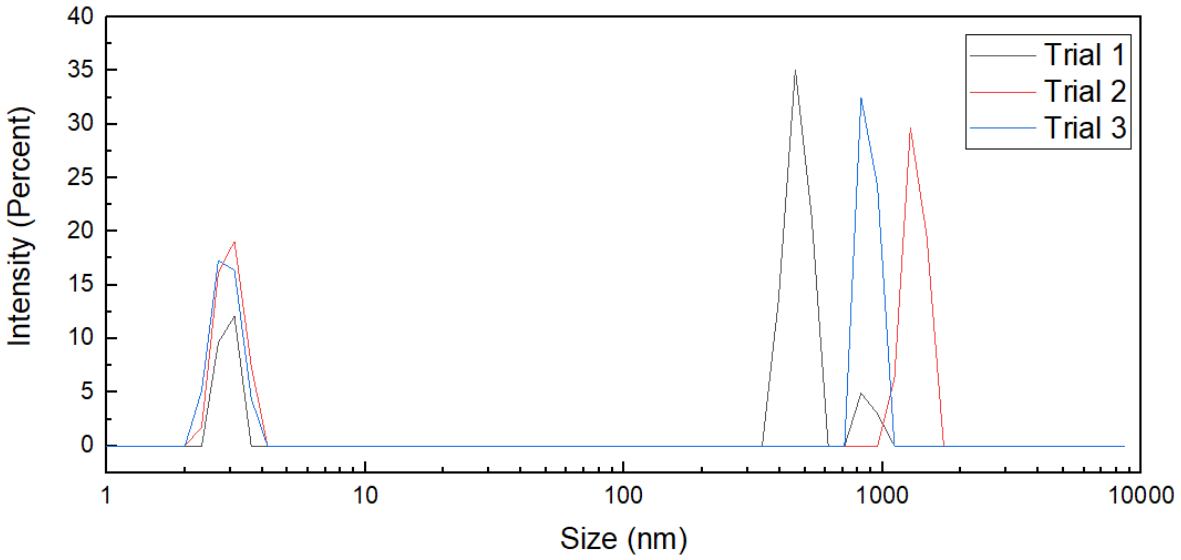

Figure 43. Size distribution the following day.

A two sample t-test gives a p-value greater than 0.05 and indicates we can accept the null hypothesis that the size distributions of 1 mM G2 Dendrimer (M = 3.014, SD = 0.0348) and the size distributions of the 0.05:1 uranyl:G2 PAMAM dendrimer sample (M = 2.853, SD = 0.0581) are the same population. We can also confirm the inherent assumption that the large, higher intensity particles that have been observed throughout the experiment are some artifact from solution contamination, as it is still present in the final, equilibrated solution.

The amalgamation of the data qualitatively shows an initial electrostatic aggregate of G2 PAMAM dendrimers and associated ions, particularly the uranyl ion, to neutralize the charge of the substances. Over time, these unstable aggregates move in and out of the incident beam, leading to inconsistent size distributions over time. The sizes either vary

among different aggregate or the constituent molecules and ion are rearranging and reassembling into different aggregates over time. Eventually, as more of the heavier aggregates settle to the bottom, the optimal amount of dendrimer has complexed with uranyl ions and the remaining, free dendrimer in solution can be seen in the size distribution.

This mechanism of precipitation is consistent with coagulation, in which addition of an ion or other electrolyte to a colloidal solution causes precipitation, particularly through aggregation of particles by interactions of electrostatic surface charges. A cloud of counterions can form around added particles, neutralizing charge and removing the net charge that aids in dissolution. Eventually, as the mass of the aggregates increases, a second molecule is added to combine them into larger particles that settle in the container in an often-coupled process called flocculation. Coagulation and flocculation typically require two different molecules: one to neutralize the charge and a second to aid in precipitation, typically a long-chained dendrimer.

In this case, the uranium would be analogous to the coagulant which neutralizes the charge and likely initiates some initial aggregation and precipitation upon binding with the dendrimer, which acts as a ligand. However, the dendrimer also behaves as a flocculant because it is a polymer. It has the potential for crosslinking utilizing multiple binding sites along its chain or utilizing multiple binding sites from different arms to coordinate uranyl. Along the uranyl equatorial plane, multiple dendrimer binding sites from one or more dendrimers create a hyperlinked, organized supramolecular structure. This eliminates the

need for multiple different molecules to perform both the coagulation and flocculation steps because the dendrimer serves multiple purposes (**Figure 45**).

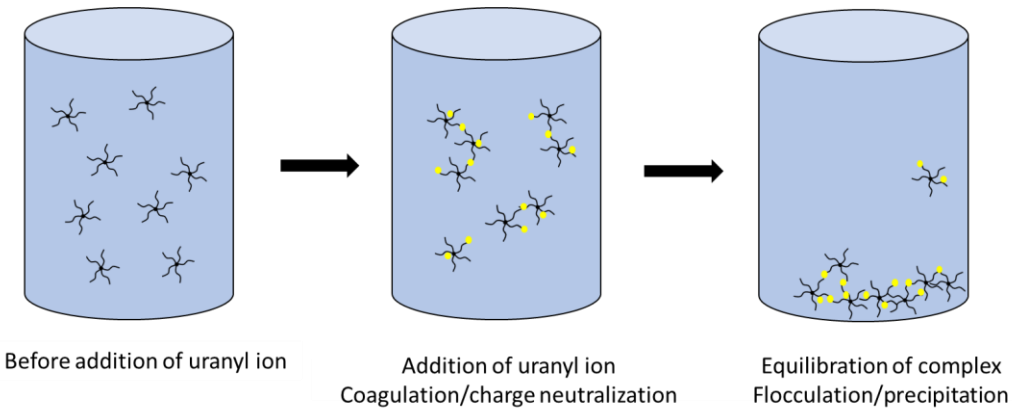

Figure 44. Simplified representation of uranyl-PAMAM dendrimer precipitation analogous to coagulation and flocculation.

5.5 Neptunyl-PAMAM Dendrimer Complexes

The coordination chemistry is challenging to elucidate for uranyl-PAMAM dendrimer complexes due to the many binding sites and presence of a second phase. Therefore, although thus far it is know that the PAMAM dendrimers appear highly selective for the uranyl ion, especially compared to lanthanides such as neodymium, it cannot be definitely determined whether this is due to the size of the uranyl ion, the chemical properties of the uranyl ion, geometry of binding, cooperative coprecipitation or postprecipitation, dendritic effects, or some other phenomenon. One of the simpler techniques to examine if this is due to the structure and chemical properties of the uranyl ion itself is to examine another actinyl ion such as neptunium or plutonium.

For UV-Visible experiments, the absorbance of the metal ion is measured when titrated with the G*X* PAMAM dendrimer to directly monitor the change in the metal ion

when complexed with the dendrimer, which was not possible to do directly with the uranyl ion for the reasons previously described **3.1.2.**1. Due to the radioactive nature of neptunium, fluorescence spectroscopy in a shared facility was also not feasible at the time of experimentation. Regardless, a clear difference was seen when even small molar equivalents of dendrimer were present in the neptunyl solution. Without dendrimer present, addition of the NpO_2 to a solution of 1 M $NaNO_3$ at a pH of 7 turned the green-blue neptunyl stock into a slightly brown solution (**Figure 46**). The brown color is characteristic of NpO_2^+ speciation in a neutral to alkaline solution, whereas the ion normally forms a blue-green solution in acidic conditions.

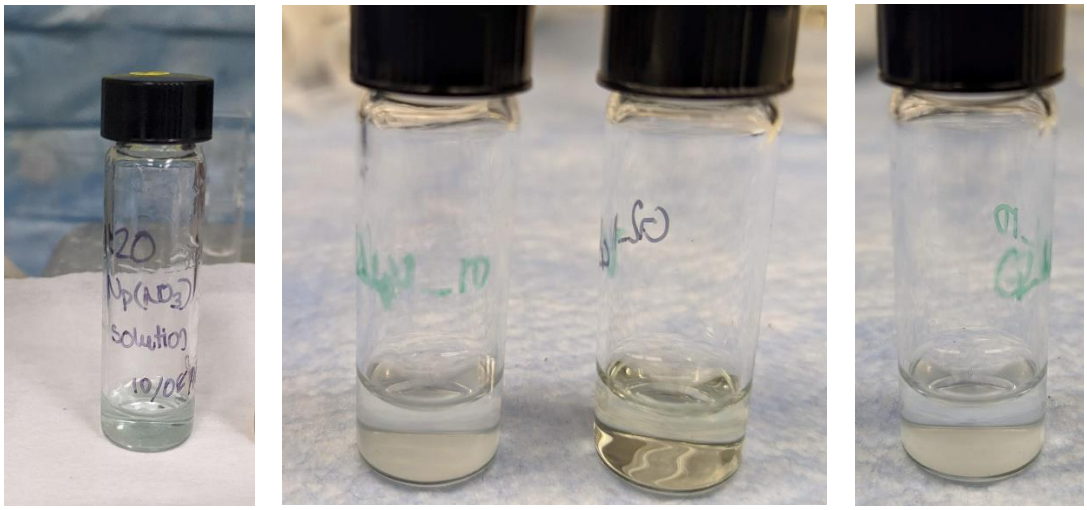

Figure 45. The light blue colored stock solution (*left*), color comparison of samples with (left vial) and without (right vial) dendrimer (*center*), and a thin film of white precipitate seen at the bottom of the vials containing PAMAM dendrimer (*right*).

a) b)

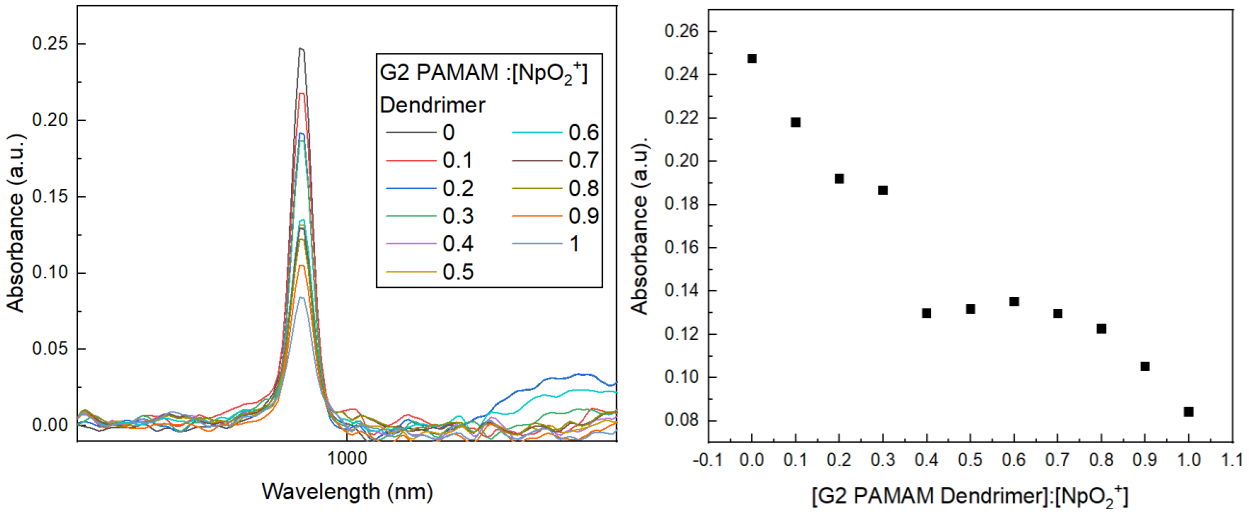

Figure 46. NIR absorbance as a function of [G2 PAMAM Dendrimer]:[NpO_2^+] ratio.

Analysis of the liquid phase in the NIR region reveals that the absorbance signal of the NpO_2^+ at approximately 980 nm, proportional to the concentration, decreases with no introduction of a red-shifted or blue-shifted complexation peak. This is expected, as it is likely that a majority of the neptunyl that has been removed has been separated into the solid phase. There is an unusual discontinuity between a ratio of 0.3 to 0.4, followed by a plateau until about a ratio of 0.7. The data points above and below this point with the exclusion of 0.4 – 0.6 are mainly linear.

This transitional period of nonlinear signal is likely where precipitate begins to form in appreciable quantities. The discontinuity could represent the solid precipitating immediately after some critical concentration is reached. Following that, addition of more dendrimer could simply aggregate with the bulk solid until some concentration is reached

(at about a ratio of 0.6) when additional dendrimer molecules with available binding sites begin complexing the neptunyl ion once again.

Measurements of the solid phase, redissolved into 0.01 M nitric acid, confirms separation of some quantity of the neptunyl into a solid phase, with irregular signal (**Figure 48**). Spectra were corrected for the relative absorbance increase due to the difference in pH using two NpO_2^+ standards in the more acidic and less acidic conditions.

a) b)

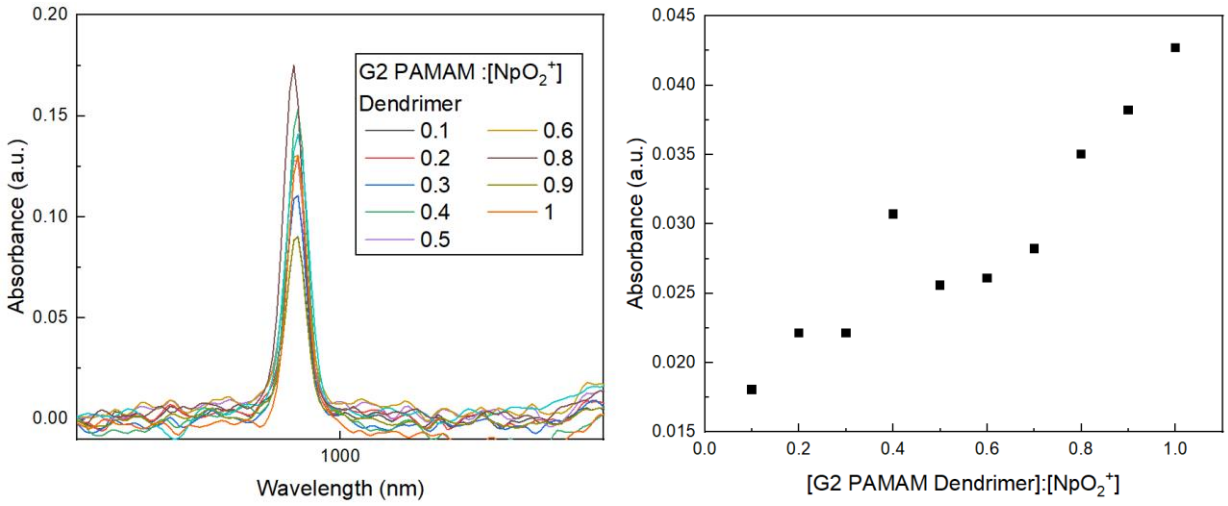

Figure 47. NIR absorbance of the redissolved precipitate as a function of [G2 PAMAM Dendrimer]:[NpO_2^+] ratio.

The concentration of NpO_2^+ does increase with higher relative concentration of the G2 PAMAM dendrimer added, with the exception of the sample with the 0.4 molar ratio. This could possibly be an outlier but the experiment was not repeated due to the scarcity of the neptunium and the conclusions that can be drawn regardless of this outlier. The rapid decrease in neptunyl concentration at this molar ratio followed by a plateau in the liquid

phase indicates this may be an interesting and important point to keep in as a transitional point in the complexation chemistry from the liquid to the solid phase.

Overall, although the concentration in the solid phase (c_s) does increase, relative to the theoretical total concentration (c_{tot}), it is still a small percentage compared to the non-complexed neptunyl in the liquid phase (c_{free}), as well as the neptunyl that has been calculated to be complexed in the liquid phase (c_l) (**Figure 49**).

$$c_{tot} = c_{free} + c_l + c_s$$

$$c_l = c_{free} + c_{tot} + c_s$$

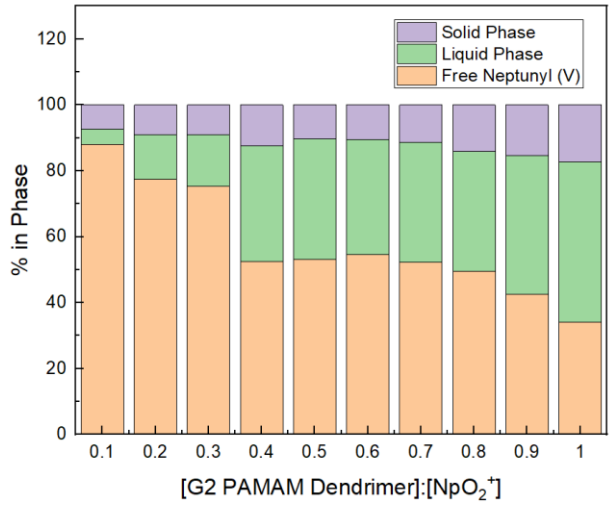

Figure 48. Phase distribution of neptunyl (V) with addition of small molar amounts of G2 PAMAM dendrimer.

In comparison with the uranyl experiments, it must be noted that the free uranyl ions in solution and uranyl-PAMAM dendrimer complexes in the liquid phase could not be differentiated. This was a result of the careful experimental design to examine PAMAM dendrimer fluorescence without interference from uranyl fluorescence. Regardless, it is

evident in comparison with **Figure 26** that the uranyl ion tends to have higher precipitation while approaching the 1:1 metal ion:G2 PAMAM dendrimer ratio, a trend that should continue with increased metal ion loading.

The experiment was repeated similarly with NpO_2^{2+}, also known as neptunyl (VI). Although this has a similar structure as neptunyl (V) and uranyl (VI), it has the same oxidation state and subsequently the same charge as the uranyl (VI) ion, UO_2^{2+}. With addition of a small (0.1:1 [G2 PAMAM dendrimer]:[NpO_2^{2+}]) amount of dendrimer, a large portion of the neptunyl (VI) was instantaneously reduced to neptunyl (V). It also significantly blue-shifts the neptunyl (VI) from about 1226 nm to 1100 nm (**Figure 50**). This could be evidence of complexation in the liquid phase that is less stable (higher energy complex) than the ground state of neptunium alone. This could be consistent with either of two NIR peaks (1080 and 1120 nm) that have previously reported with neptunyl dinitrate complexes in highly (4 M HNO_3) acidic media, resulting from two nitrate ions replacing water molecules in the inner coordination sphere.[118] At a neutral pH such as the experiments completed in this work and with the addition of an N-donor ligand, there is equal likelihood that the Np-N bond could be between neptunyl (VI) and a nitrate ion or an amine-based nitrogen from the PAMAM dendrimer.

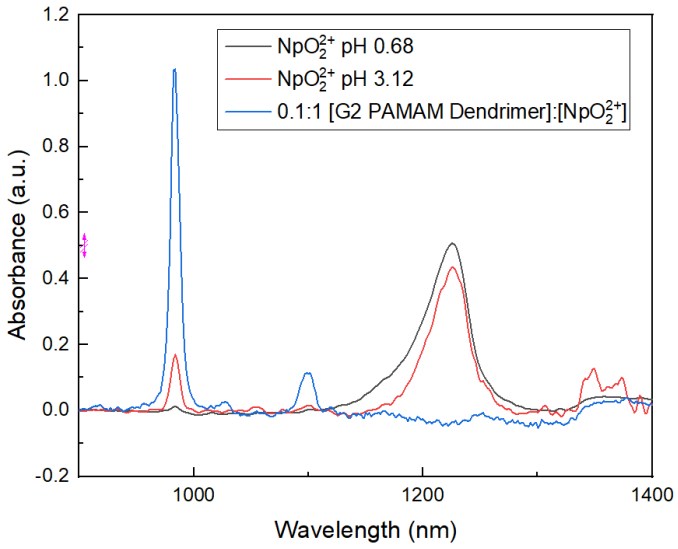

Figure 49. NIR spectrum of neptunyl (VI) before and after pH adjustment, and after a small aliquot of G2 PAMAM Dendrimer is added.

Most likely, this is due to the neutral pH conditions and not necessarily due to the presence of the G2 PAMAM dendrimer beyond the fact that the G2 PAMAM dendrimer tends to hold the pH at a relatively constant value due to its numerous amine sites, which can be protonated or deprotonated. The absorbance remains stable, with only a slight increase in the 1100 nm peak when measured the next day (**Figure 51**).

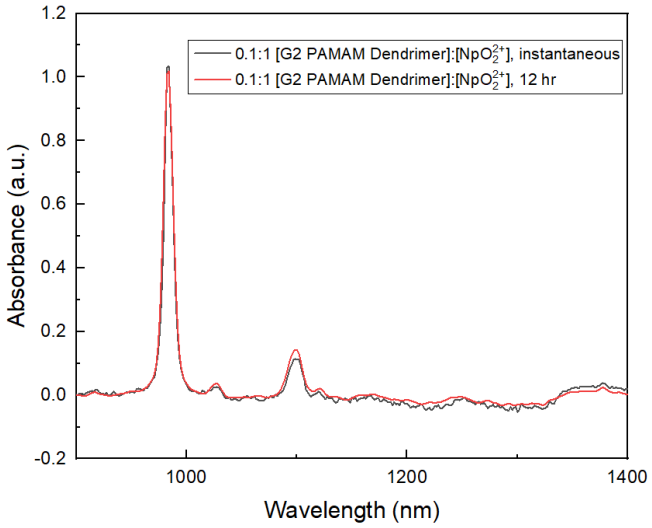

Figure 50. Comparison of NIR absorbance signal of a 0.1:1 [G2 PAMAM Dendrimer]: [NpO22+] sample immediately after the addition of dendrimer.

This indicates that the dendrimer can effectively stabilize some portion of the neptunyl in the Np(VI) state, whereas without the dendrimer, Np(VI) will typically reduce within several hours in solutions that are not highly acidic. This pattern remains consistent through several samples with varying concentrations of G2 PAMAM dendrimer, varying only in a slight variation in the absorbance of 1100 nm peak (**Figure 52**).

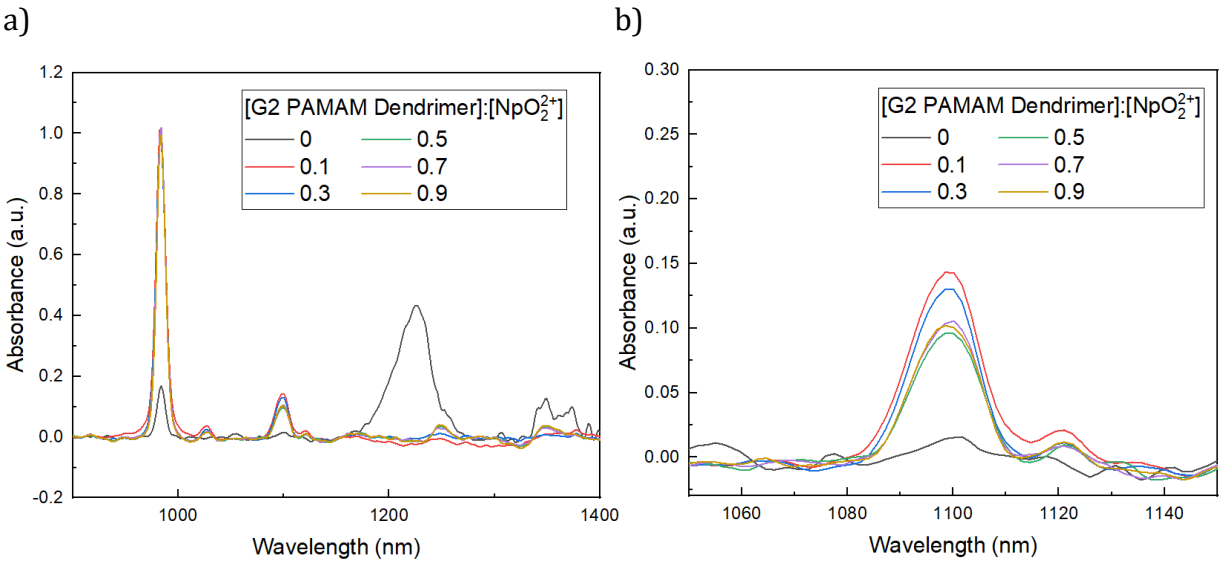

Figure 51. NIR absorbance as a function of [G2 PAMAM Dendrimer]:[NpO_2^{2+}] ratio.

At a molar ratio of 1:1 [G2 PAMAM Dendrimer]:[NpO_2^{2+}], the solution looks significantly different from the preceding samples and when left to equilibrate, a brown precipitate forms, a characteristic color of neptunyl (VI) solids (**Figure 53**).

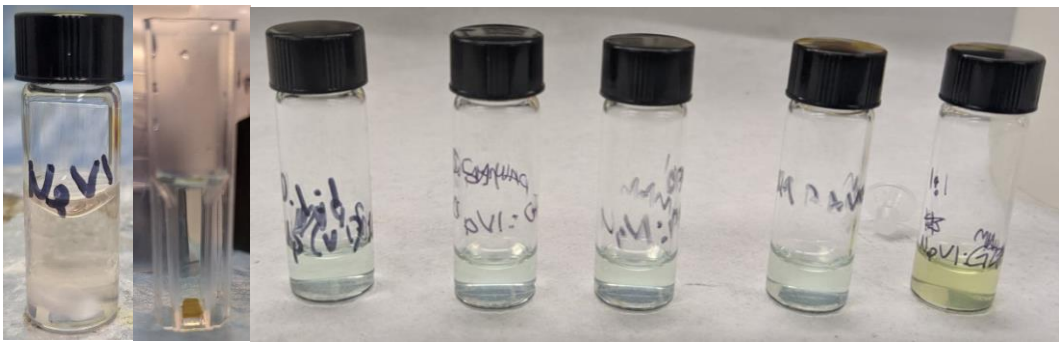

Figure 52. Neptunyl (VI) stock solution (*left*), a 1:1 [G2 PAMAM Dendrimer]:[NpO_2^{2+}] solution with brown precipitate formation (*second from left*), and neptunyl (VI) solutions after a day of equilibration and after 15 minutes of agitation on a vortex mixer, with the 1:1 sample on the far right (*right*).

Evidence of precipitate formation can be seen in a very high baseline when the G2 PAMAM dendrimer was added, however, this stabilized within 10 minutes. After leaving

the sample in a cuvette overnight, the precipitate settled to the bottom and the supernatant was measured (**Figure 54**).

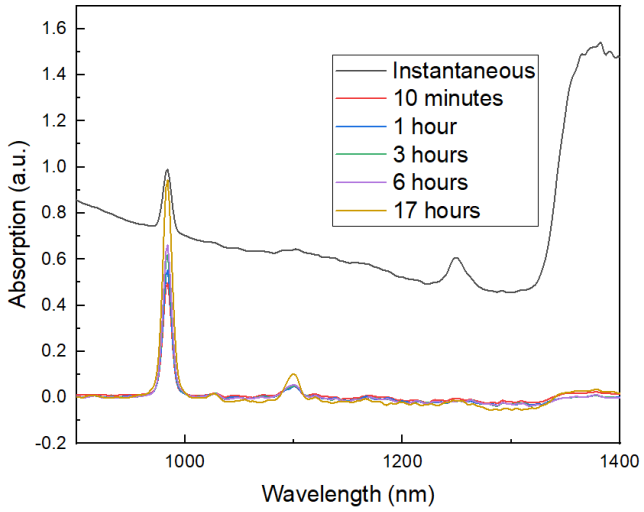

Figure 53. NIR absorbance of a 1:1 [G2 PAMAM Dendrimer]:[NpO_2^{2+}] sample over time. Note: Background subtraction was performed only on the 17 hour measurement.

Interestingly, it appears that over time the characteristic neptunyl (V) peak at 980 nm begins to increase. The molar absorptivity of neptunyl (V) is nearly ten times higher than that of neptunyl (VI), so this could be a result of the neptunyl (VI) reducing over several hours. However, when compared with a sample with a lower concentration of dendrimer (**Figure 51**), the spectrum looks nearly the same measured immediately after the precipitate and measured the following day. This means there is some intermediate step that the 1:1 sample is undergoing that the other samples do not. Because there are more dendrimer molecules in this sample, more interaction and precipitate forms initially (at about 10 minutes). However, over time as the neptunyl (VI) reduces, it appears to have a lower affinity for the neptunyl (V) ion and releases it into solution as a free ion, leading to increased absorbance in the characteristic 980 nm region. The peak at 1100 nm also

increases over time, indicating some of the complexed NpO_2^{2+}-G2 PAMAM dendrimer complexes equilibrate back into the liquid phase. It appears the dendrimer is more stable with divalent cations than monovalent cations.

In summary, although neptunyl in the +5 and the +6 oxidation state appears to complex and partially precipitate, the precipitation percentage is low compared to uranium and it mostly remains either as a non-complexed ion or in a liquid-phase complex. The one noticeable exception is NpO_2^{2+}, which at a ratio of 1:1 [G2 PAMAM Dendrimer]:[NpO_2^{2+}] has a significantly observable precipitate especially compared to the other samples at lower ratios. This appears to be because the absolute concentration of neptunyl (VI) was ten times higher in comparison to the neptunyl (V) and uranyl (VI) samples to obtain a better NIR signal with a lower molar absorptivity. In addition, this may indicate a slightly higher affinity for a +2 cation, such as uranyl (VI) and neptunyl (VI). Both NpO_2^{+} and NpO_2^{2+} appear to have rapid precipitate transitions, though the NpO_2^{+} transition is both unstable, inconsistent following the transition, and most importantly does not appear to cause significant precipitation at a concentration of 1 mM. Although this research could use more in-depth analysis in certain areas, these preliminary results indicate that PAMAM dendrimers can coordinate neptunium to cause bulk precipitation of the actinyls, including the potential for plutonyl precipitation if the plutonium is oxidized to the hexavalent state. This would be highly useful for generation of MOX fuel, although the amount of neptunyl precipitated must be carefully controlled to avoid a positive void coefficient during reactor operation.[119] In addition, the high variability of precipitation observed in the neptunyl and uranyl studies indicate the oxidation state of the actinyl, the absolute concentration of the

metal ion, and the pH of solutions can be manipulated to selectively precipitate some actinyls or potentially hold some metal ions back in the liquid phase while other actinyls are extracted, depending on the conditions.

Chapter 6: Conclusions and Future Work

Highly efficient separatory schemes are essential for reprocessing to close the nuclear fuel cycle, increasing the efficiency of the fuel cycle and for general nuclear safety and security, including environmental remediation. The goal of this research was to investigate the overall complexation of four metal ions with the PAMAM dendrimer which are important for the nuclear fuel cycle: neodymium (III) (a representative for the lanthanides), uranyl (VI), neptunyl (V) and neptunyl (VI). In particular, although it is known that dendrimers with nitrogen donors have a high affinity for uranyl (VI), the reason behind this affinity had not yet been elucidated. Characterization of the extent of binding, the extent of separation, the nature of the coordination and subsequent separation of the complexes, the selectivity of the dendrimer, the solubility of the complexes and the conditions of the separation are all relevant not only to understanding the coordination chemistry of PAMAM dendrimers, but also to pave the way for data-driven design of future separatory systems that can use customized dendrimers.

Fluorescence spectroscopy determined that PAMAM dendrimers in neutral solutions were virtually unreactive with the neodymium (III) ion at neutral pH but bound numerous uranyl (VI) ions exceedingly well, resulting in the formation of a uranium-containing solid phase, reported here for the first time. This can provide high selectivity between the trivalent lanthanides and the actinyls at neutral pH with high metal ion loading, because lanthanides have similar chemical properties and therefore are expected to have similar non-binding behavior with PAMAM dendrimers. In comparison, UV-Vis-NIR confirmed that neptunyl (V) and (VI) both formed complexes with PAMAM dendrimers,

also resulting in the formation of precipitate. This indicates part of the affinity for these types of elements is due to their dioxocation structural (AnO_2^+/AnO_2^{2+}), and suggests plutonyl should follow similar binding behavior. The PAMAM dendrimers appear to have a slightly higher affinity for the AnO_2^{2+} (hexavalent U(VI) and Np(VI) ions versus the AnO_2^+ (pentavalent Np(V)) ions, which is expected because the hexavalent actinyl ions are expected to act similarly in solution.

Besides the overall PAMAM dendrimer affinity for uranyl (VI), there appears to be the advantageous formation of precipitate which allows for liquid-to-solid separation. DLS measurements support a proposed theory of a precipitation process similar to coagulation and flocculation. In this system, uranyl plays the role of the coagulant and the PAMAM dendrimer acts as both the ligand and the flocculant, simplifying the number of species needed for this process to occur. At a concentration above 0.05 mM, NAA analysis indicates nearly all uranium will precipitate out of solution with just a 5:1 uranyl:G2 PAMAM dendrimer molar ratio. NAA reveals that this precipitate begins well before the eye can detect its presence. In addition, a retention capacity can be calculated to determine the optimal generation where the inhibition of binding due to dendritic, steric effects does not proportionally outweigh the number of potential binding sites. For this system, that point was determined to be Generation 2, which follows the proposed model from the literature that Generation 2 is the transitional generation between an open, extended structure and a contracted, globular structure.

This information could be utilized to precipitate the actinyls together in the most efficient manner, in a way that would be useful for further MOX fuel fabrication. The

precipitate can also be washed with acid (<0.01 M HNO_3) to separate the metal ion from the dendrimer for reuse if desired. This proposed system would be a simple, highly effective, and selective way of removing actinyl ions from aqueous streams. However, more research would need to be done on the effect of competing ions. Overall, the simplicity and high efficiency of a liquid-to-solid phase separation system leads to reduced need for materials such as solid phase supports or multiple liquid phase which gives this system an advantage over LLE/SX or SPE.

Beyond a qualitative examination of the nature of the precipitate, further insight to the coordination chemistry of the PAMAM dendrimer continues to remain elusive. The precipitate formation poses a challenge for typically rigorous analytical tools such as EXAFS and TRF. Fluorescence spectroscopy supports the idea that in the liquid phase, uranyl ions will preferentially bind to the tertiary, interior sites when the samples are left to equilibrate in accordance with other proposed models from the literature. But, the formation of precipitate conversely supports the idea of a "dense core" dendritic effect, where the interior of the dendrimer is more dense at neutral to high pH, promoting coordination at the terminal sites and subsequent precipitation. Further carefully designed experiments to examine the liquid phase, such as EXAFS experimental designs for colloid based systems, and the solid phase, such as SAXS, would be instrumental to clarifying the very unique coordination chemistry of this system.

Without this, it is difficult to determine what could be altered to support selectivity of other ions, or improved to support even more efficient separation of the actinyl ions. However, future work could focus on altering different parts of the dendrimer to further

probe the nature of binding. For example, capping a PAMAM dendrimer with a different terminal group and testing complexation with the uranyl ion could determine if the precipitate is indeed due to cross-linking at the terminal sites. Changing the internal branches of the dendrimer and examining the binding efficiency could determine if the high metal ion loading is due to preferential binding in the tertiary amine sites, or if the binding is mainly at the terminal sites.

In addition, PAMAM dendrimer complexes and precipitates were found to be sensitive to pH, the ratio of metal to ligand, absolute concentration of the metal ion, and the oxidation state of the metal ion, but not the ionic strength as long as the ions in solution are not competing. These factors can be tuned to manipulate which ions will complex and/or precipitate out of solution. In particular, lowering the pH can determine which ions will preferentially complex when the dendrimer is more protonated than it is at neutral pH. Future work should also focus on examining solutions with multiple competing ions to determine which of these factors are most important for selectivity, binding and separation. Monitoring mixed ion solutions using flow cells with UV-Vis spectroscopy and/or fluorescence spectroscopy provides rapid, and potentially on-line, analytical techniques that offer multiple ways of examining the spectroscopic changes of both the dendrimer and the metal ions.

References

1. Looney, B. Statistical Review of World Energy, 2020 | 69th Edition. *Bp* **69**, 66 (2020).
2. Canadian Nuclear Association. The Canadian Nuclear Factbook 2019. 1–84 (2019).
3. International Atomic Energy Agency. IAEA Annual Report 2018. *IAEA Annu. Rep.* 128 (2018).
4. Reuters Staff. China Jan-Sept Nuclear Power Generation Up 23% From Year Ago. https://www.reuters.com/article/china-nuclearpower/china-jan-sept-nuclear-power-generation-up-23-from-year-ago-assn-idUSL3N27H03H.
5. Nuclear Engineering International. China to Build Six to Eight New Reactors A Year Between 2020 and 2025. https://www.neimagazine.com/news/newschina-to-build-six-to-eight-new-reactors-a-year-between-2020-and-2025-8022479#:~:text=China led the world in,generated in China in 2019. (2020).
6. Nuclear Energy Instiute. Used Fuel Storage and Nuclear Waste Fund Payments by State. https://www.nei.org/resources/statistics/used-fuel-storage-and-nuclear-waste-fund-payments (2020).
7. Garvey, T. Closing yucca mountain: Litigation associated with attempts to abandon the planned nuclear waste repository. *Nucl. Waste Quest. Propos.* 1–26 (2012).
8. Ewing, R. C. Long-term storage of spent nuclear fuel. *Nat. Mater.* **14**, 252–257 (2015).
9. International Atomic Energy Agency. Development of Advanced Reprocessing Technologies. *Proc. 52nd Gen. Conf. Memb. States* 1–11 (2008).
10. Nash, K. L. & Lumetta, G. J. *Advanced separation techniques for nuclear fuel reprocessing and radioactive waste treatment*. *Advanced Separation Techniques for Nuclear Fuel Reprocessing and Radioactive Waste Treatment* (2011). doi:10.1533/9780857092274.
11. Rydberg, J. *Solvent Extraction Principles and Practice, Revised and Expanded*. *Solvent Extraction Principles and Practice, Revised and Expanded* (Taylor & Francis, 2004). doi:10.1201/9780203021460.
12. Zheng, Y., Wu, H., Cao, L. & Jia, S. Economic Evaluation on the MOX Fuel in the Closed Fuel Cycle. **2012**, (2012).
13. Rodman, M.R.; Gordon, L.I.; Chen, A. C. T. *Extraction of Uranium from Seawater: Evaluation of Uranium Resourcs and Plant Sitting*. *XN-RT-14* vol. 2 (1979).
14. Rao, L. *Recent International R & D Activities in the Extraction of Uranium from Seawater*. (2011).
15. Abney, C. W., Mayes, R. T., Saito, T. & Dai, S. Materials for the Recovery of Uranium

from Seawater. *Chem. Rev.* **117**, 13935–14013 (2017).

16. Kim, J. *et al.* Recovery of Uranium from Seawater: A Review of Current Status and Future Research Needs. *Sep. Sci. Technol.* **48**, 367–387 (2013).

17. Kumar, J. R., Kim, J. S., Lee, J. Y. & Yoon, H. S. A brief review on solvent extraction of uranium from acidic solutions. *Sep. Purif. Rev.* **40**, 77–125 (2011).

18. Veliscek-Carolan, J. Separation of actinides from spent nuclear fuel : A review. *J. Hazard. Mater.* **318**, 266–281 (2016).

19. Jenkins, I. L. Solvent Extraction Chemistry in the Atomic Energy Industry - A Review. *Hydrometallurgy* **4**, 1–20 (1979).

20. Aly, M. M. & Hamza, M. F. A Review: Studies on Uranium Removal Using Different Techniques. Overview. *J. Dispers. Sci. Technol.* **34**, 182–213 (2013).

21. Kumari, I., Kumar, B. V. R. & Khanna, A. A review on UREX processes for nuclear spent fuel reprocessing. *Nucl. Eng. Des.* **358**, 110410 (2020).

22. Manna, D. & Ghanty, T. K. Complexation behavior of trivalent actinides and lanthanides with 1,10-phenanthroline-2,9-dicarboxylic acid based ligands: Insight from density functional theory. *Phys. Chem. Chem. Phys.* **14**, 11060–11069 (2012).

23. Nash, K.L., Lumetta, G.L., Vienna, J. D. Irradiated Nuclear Fuel Management: Resource versus Waste. in *Radioactive Waste Management and Contaminated Site Clean-Up: Processes, Technologies and International Experience* 171–272 (Woodhead Publishing Limited, 2013). doi:10.1533/9780857097446.1.171.

24. Cotton, S. *Lanthanide and Actinide Chemistry*. *Lanthanide and Actinide Chemistry* (2006). doi:10.1002/0470010088.

25. Gill, M., Livens, F. & Peakman, A. Nuclear Fission. in *Future Energy: Improved, Sustainable and Clean Options for our Planet* (2013). doi:10.1016/B978-0-08-099424-6.00009-0.

26. Lovasic, Z. Spent Fuel Reprocessing Options, IAEA-TECDOC-1587. *Nucl. Fuel Cycle Mater. Sect.* 151 (2008).

27. Taylor, R. *Reprocessing and Recycling of Spent Nuclear Fuel*. *Reprocessing and Recycling of Spent Nuclear Fuel* (Woodhead Publishing Limited, 2015). doi:10.1016/C2013-0-16483-5.

28. Tsouris, C. Uranium extraction: Fuel from seawater. *Nat. Energy* **2**, 2–4 (2017).

29. Ansari, S. A. & Mohapatra, P. K. A review on solid phase extraction of actinides and lanthanides with amide based extractants. *J. Chromatogr. A* **1499**, 1–20 (2017).

30. Rao, T. P., Metilda, P. & Gladis, J. M. Preconcentration techniques for uranium(VI) and thorium(IV) prior to analytical determination-an overview. *Talanta* **68**, 1047–1064

(2006).

31. Rosenberg, E., Pinson, G., Tsosie, R., Tutu, H. & Cukrowska, E. Uranium remediation by ion exchange and sorption methods: A critical review. *Johnson Matthey Technol. Rev.* **60**, 59–77 (2016).

32. Tomalia, D. A. Dendritic effects: Dependency of dendritic nano-periodic property patterns on critical nanoscale design parameters (CNDPs). *New J. Chem.* **36**, 264–281 (2012).

33. Chow, H. F., Leung, C. F., Wang, G. X. & Yang, Y. Y. Dendritic effects in functional dendrimer molecules. *Comptes Rendus Chim.* **6**, 735–745 (2003).

34. Boas, U., Christensen, J. B. & Heegaard, P. M. H. Dendrimers: Design, synthesis and chemical properties. *J. Mater. Chem.* 3785–3798 (2006) doi:10.1039/b611813p.

35. Castillo, V. A., Barakat, M. A., Ramadan, M. H., Woodcock, H. L. & Kuhn, J. N. Metal ion remediation by polyamidoamine dendrimers: A comparison of metal ion, oxidation state, and titania immobilization. *Int. J. Environ. Sci. Technol.* **11**, 1497–1502 (2014).

36. Vunain, E., Mishra, A. K. & Mamba, B. B. Dendrimers, mesoporous silicas and chitosan-based nanosorbents for the removal of heavy-metal ions: A review. *Int. J. Biol. Macromol.* **86**, 570–586 (2016).

37. Sadjadi, S. & Sadjadi, S. 13 - Dendritic polymers for environmental remediation. in (eds. Hussain, C. M. & Mishra, A. K. B. T.-N. P. N. for E. R.) 279–335 (Elsevier, 2018). doi:https://doi.org/10.1016/B978-0-12-811033-1.00013-5.

38. Mohseni, M., Akbari, S., Pajootan, E. & Mazaheri, F. Amine-terminated dendritic polymers as a multifunctional chelating agent for heavy metal ion removals. *Environ. Sci. Pollut. Res. Int.* **26**, 12689–12697 (2019).

39. Sajid, M. Dendrimers based sorbents: Promising materials for analytical extractions. *TrAC Trends Anal. Chem.* **98**, 114–127 (2018).

40. Huang, Y. & Feng, X. Polymer-enhanced ultrafiltration: Fundamentals, applications and recent developments. *J. Memb. Sci.* **586**, 53–83 (2019).

41. Priyadarshini, N., Benadict Rakesh, K. & Ilaiyaraja, P. Actinide Speciation in Environment and Their Separation Using Functionalized Nanomaterials and Nanocomposites. in *Handbook of Environmental Materials Management* (2018).

42. Diallo, M. S., Arasho, W., Johnson, J. H. & Goddard III, W. A. Dendritic Chelating Agents. 2. U(VI) Binding to Poly(amidoamine) and Poly(propyleneimine) Dendrimers in Aqueous Solutions. *Environ. Sci. Technol.* **42**, 1572–1579 (2008).

43. Zhang, Q., Wang, N., Zhao, L., Xu, T. & Cheng, Y. Polyamidoamine Dendronized Hollow Fiber Membranes in the Recovery of Heavy Metal Ions. *ACS Appl. Mater. Interfaces* **5**, 1907–1912 (2013).

44. Grüttner, C. *et al.* Dendrimer-coated magnetic particles for radionuclide separation. *J. Magn. Magn. Mater.* **293**, 559–566 (2005).

45. Yuan, D. *et al.* Synthesis of PAMAM dendron functionalized superparamagnetic polymer microspheres for highly efficient sorption of uranium(VI). *J. Radioanal. Nucl. Chem.* **309**, 1227–1240 (2016).

46. Cao, Q., Liu, Y., Wang, C. & Cheng, J. Phosphorus-modified poly(styrene-co-divinylbenzene)-PAMAM chelating resin for the adsorption of uranium(VI) in aqueous. *J. Hazard. Mater.* **263**, 311–321 (2013).

47. Ilaiyaraja, P., Deb, A. K. S., Ponraju, D., Ali, S. M. & Venkatraman, B. Surface Engineering of PAMAM-SDB Chelating Resin with Diglycolamic Acid (DGA) Functional Group for Efficient Sorption of U(VI) and Th(IV) from Aqueous Medium. *J. Hazard. Mater.* **328**, 1–11 (2017).

48. Priyadarshini, N. & Ilaiyaraja, P. Adsorption of U(VI) and Th(IV) from simulated nuclear waste using PAMAM and DGA functionalized PAMAM dendron grafted styrene divinylbenzene chelating resins. *Chem. Pap.* **73**, 2879–2884 (2019).

49. Ilaiyaraja, P., Singha Deb, A. K., Sivasubramanian, K., Ponraju, D. & Venkatraman, B. Adsorption of uranium from aqueous solution by PAMAM dendron functionalized styrene divinylbenzene. *J. Hazard. Mater.* **250–251**, 155–166 (2013).

50. Cong, H. *et al.* Preparation and evaluation of PAMAM dendrimer-based polymer gels physically cross-linked by hydrogen bonding. *Biomater. Sci.* **7**, 3918–3925 (2019).

51. Shaaban, A. F., Khalil, A. A., Lasheen, T. A., Nouh, E. S. A. & Ammar, H. Polyamidoamine dendrimers modified silica gel for uranium(VI) removal from aqueous solution using batch and fixed-bed column methods. *Desalin. Water Treat.* **102**, 197–210 (2018).

52. Ansari, S. A., Mohapatra, P. K., Leoncini, A., Huskens, J. & Verboom, W. Diglycolamide-functionalized dendrimers: Studies on Americium(III) pertraction from radioactive waste. *Sep. Purif. Technol.* **187**, 110–117 (2017).

53. Ottaviani, M. F. *et al.* A TEM and EPR Investigation of the Competitive Binding of Uranyl Ions to Starburst Dendrimers and Liposomes : Potential Use of Dendrimers as Uranyl Ion Sponges. *Langmuir* 7368–7372 (2000) doi:10.1021/la000355w.

54. Appelhans, D. *et al.* Dense-shell glycodendrimers: UV/Vis and electron paramagnetic resonance study of metal ion complexation. *Proc. R. Soc. A Math. Phys. Eng. Sci.* **466**, 1489–1513 (2010).

55. Diallo, M. S. *et al.* Dendritic chelating agents. 1. Cu(II) binding to ethylene diamine core poly(amidoamine) dendrimers in aqueous solutions. *Langmuir* **20**, 2640–2651 (2004).

56. Likos, C. N. *et al.* Star Polymers Viewed as Ultrasoft Colloidal Particles. *Phys. Rev. Lett.*

80, 4450–4453 (1998).

57. Rathgeber, S., Monkenbusch, M., Kreitschmann, M., Urban, V. & Brulet, A. Dynamics of star-burst dendrimers in solution in relation to their structural properties. *J. Chem. Phys.* **117**, 4047–4062 (2002).

58. Stellbrink, J. *et al.* Neither Gaussian chains nor hard spheres - Star polymers seen as ultrasoft colloids. *Prog. Colloid Polym. Sci.* **115**, 88–92 (2000).

59. Carbone, P. & Müller-Plathe, F. Molecular dynamics simulations of polyaminoamide (PAMAM) dendrimer aggregates: Molecular shape, hydrogen bonds and local dynamics. *Soft Matter* **5**, 2638–2647 (2009).

60. Blasini, D. R., Flores-Torres, S., Smilgies, D. M. & Abruña, H. D. Stepwise self-assembly of ordered supramolecular assemblies based on coordination chemistry. *Langmuir* **22**, 2082–2089 (2006).

61. Lakowicz, J. R. *Principles of fluorescence spectroscopy*. (Springer, 2006). doi:10.1007/978-0-387-46312-4.

62. An Introduction to Fluorescence Spectroscopy. 15 (2000).

63. Fluorescence Quenching Studies. *Phys. Prakt. I* 1–14 (2016).

64. Chu, C. C. & Imae, T. Fluorescence investigations of oxygen-doped simple amine compared with fluorescent PAMAM dendrimer. *Macromol. Rapid Commun.* **30**, 89–93 (2009).

65. Wang, D., Imae, T. & Miki, M. Fluorescence emission from PAMAM and PPI dendrimers. *J. Colloid Interface Sci.* **306**, 222–227 (2007).

66. Wang, D. & Imae, T. Fluorescence emission from dendrimers and its pH dependence. *J. Am. Chem. Soc.* **126**, 13204–13205 (2004).

67. Bünzli, J. C. G. Lanthanide Luminescence: From a Mystery to Rationalization, Understanding, and Applications. *Handb. Phys. Chem. Rare Earths* **50**, 141–176 (2016).

68. Misra, S. N. & Sommerer, S. O. Absorption Spectra of Lanthanide Complexes in Solution. *Appl. Spectrosc. Rev.* **26**, 151–202 (1991).

69. Hughes, I. D. *et al.* Lanthanide contraction and magnetism in the heavy rare earth elements. *Nature* **446**, 650–653 (2007).

70. Karraker, D. G. The Hypersensitive Transitions of Hydrated Nd(III), Ho(III), and Er(III)Ions. *Inorg. Chem.* **7**, 473 (1968).

71. Ofelt, G. S. Intensities of crystal spectra of rare-earth ions. *J. Chem. Phys.* **37**, 511–520 (1962).

72. Billard, I. & Geipel, G. Standardization and Quality Assurance in Fluorescence Measurements I. in *Springer Series on Fluorescence* (ed. Resch-Genger, U.) vol. 5 465–493 (Springer, 2008).

73. Natrajan, L. S. Developments in the photophysics and photochemistry of actinide ions and their coordination compounds. *Coord. Chem. Rev.* **256**, 1583–1603 (2012).

74. Wilkerson, M. P., Berg, J. M., Hopkins, T. A. & Dewey, H. J. First observation of intra-5f fluorescence from an actinyl center: Np(VI) near-IR emission in Cs2U(Np)O2Cl4. *J. Solid State Chem.* **178**, 584–588 (2005).

75. Williams, M. Uranium(VI) uptake by geological materials, characterisation by luminescence spectroscopy. (The University of Manchester, 2017).

76. Denning, R. G. Electronic structure and bonding in actinyl ions and their analogs. *J. Phys. Chem. A* **111**, 4125–4143 (2007).

77. Sampson, T. Plutonium Isotopic Composition by Gamma-Ray Spectroscopy. *Passiv. Nondestruct. Assay Nucl. Mater.* 221–272 (1991).

78. Wahl, M. *Time-correlated single-photon counting*. (2014).

79. Choppin, G., Liljenzin, J. O., Rydberg, J. & Ekberg, C. *Radiochemistry and Nuclear Chemistry: Fourth Edition*. *Radiochemistry and Nuclear Chemistry: Fourth Edition* (Academic Press, 2013). doi:10.1016/C2011-0-07260-5.

80. Ravel, B. Introduction to x-ray absorption spectroscopy. in *Introduction to X-Ray Absorption Spectroscopy* 1–63 (2015). doi:10.1007/978-3-642-55315-8_6.

81. Newville, M. Fundamentals of XAFS. *Rev. Mineral. Geochemistry* **78**, 33–74 (2014).

82. Bunker, G. *Introduction to XAFS*. *Introduction to XAFS* (2010). doi:10.1017/cbo9780511809194.

83. Ravel, B. & Kelly, S. D. The difficult chore of measuring coordination by EXAFS. in *AIP Conference Proceedings* vol. 882 (2007).

84. *X-Ray Absorption: Principles, Applications, Techniques of EXAFS, SEXAFS and XANES*. (Wiley, 1988).

85. Malvern Instruments Ltd. Dynamic Light Scattering : An Introduction in 30 Minutes. 1–8.

86. Malvern Instruments Ltd. Zetasizer Nano Series User Manual. 1–270 (2004).

87. Stetefeld, J., McKenna, S. A. & Patel, T. R. Dynamic light scattering: a practical guide and applications in biomedical sciences. *Biophys. Rev.* **8**, 409–427 (2016).

88. Tian, G. & Rao, L. Optical Absorption, Stability and Structure of NpO2+ Complexes with Dicarboxylic Acids. (2006).

89. Fishman, D. Laser Spectroscopy Labs. https://www.chem.uci.edu/~dmitryf/Labs/Ultrafast/femto.html.

90. Xu, J. & Knutson, J. R. Ultrafast fluorescence spectroscopy via upconversion applications to biophysics. *Methods Enzymol.* **450**, 159—183 (2008).

91. Eilers, P. H. C. A perfect smoother. *Anal. Chem.* **75**, 3631–3636 (2003).

92. Chow, H., Leung, C., Wang, G. & Yang, Y. Dendritic effects in functional dendrimer molecules. **6**, 735–745 (2003).

93. Krot, K. A., De Namor, A. F. D., Aguilar-Cornejo, A. & Nolan, K. B. Speciation, stability constants and structures of complexes of copper(II), nickel(II), silver(I) and mercury(II) with PAMAM dendrimer and related tetraamide ligands. *Inorganica Chim. Acta* **358**, 3497–3505 (2005).

94. Devarakonda, B., Hill, R. A. & De Villiers, M. M. The effect of PAMAM dendrimer generation size and surface functional group on the aqueous solubility of nifedipine. *Int. J. Pharm.* **284**, 133–140 (2004).

95. Brown, P. L. & Eckberg, C. *Hydrolysis of Metal Ions*. *Hydrolysis of Metal Ions* (Wiley-VCH, 2016). doi:10.1002/9783527656189.

96. Winter, M. Uranium: radii of atoms and ions. https://www.webelements.com/uranium/atom_sizes.html (2020).

97. Larson, C. L. & Tucker, S. A. Intrinsic fluorescence of carboxylate-terminated polyamido amine dendrimers. *Appl. Spectrosc.* **55**, 679–683 (2001).

98. Konopka, M., Janaszewska, A. & Klajnert-Maculewicz, B. Intrinsic fluorescence of PAMAM dendrimers-quenching studies. *Polymers (Basel).* **10**, (2018).

99. Reynolds, J. G. Salt Solubilities in Aqueous Solutions of NaNO3, NaNO2, NaCl, and NaOH: A Hofmeister-like Series for Understanding Alkaline Nuclear Waste. *ACS Omega* **3**, 15149–15157 (2018).

100. Szilagyi, I. Tuning particle aggregation in suspensions : from monovalent ions to polyelectrolytes. (Université de Genève, 2017).

101. Dent, A. J., Ramsay, J. D. F. & Swanton, S. W. An EXAFS study of uranyl ion in solution and sorbed onto silica and montmorillonite clay colloids. *J. Colloid Interface Sci.* **150**, 45–60 (1992).

102. Wang, Y. *et al.* Mobile uranium(IV)-bearing colloids in a mining-impacted wetland. *Nat. Commun.* **4**, 1–9 (2013).

103. Kreibig, U., Bönnemann, H. & Hormes, J. Nanostructured Metal Clusters and Colloids. in *Handbook of Surfaces and Interfaces of Materials* (ed. Nalwa, H. S. B. T.-H. of S. and I. of M.) 1–85 (Academic Press, 2001). doi:https://doi.org/10.1016/B978-012513910-

6/50034-7.

104. Stern, E. A., Ma, Y., Hanske-Petitpierre, O. & Bouldin, C. E. Radial distribution function in x-ray-absorption fine structure. *Phys. Rev. B* **46**, 687–694 (1992).

105. Bühl, M., Diss, R. & Wipff, G. Coordination environment of aqueous uranyl(VI) ion. *J. Am. Chem. Soc.* **127**, 13506–13507 (2005).

106. Evans, H. T. Uranyl Ion Coordination. *Science (80-.).* **141**, 154–158 (1963).

107. Neuefeind, J., Soderholm, L. & Skanthakumar, S. Experimental Coordination Environment of Uranyl(VI) in Aqueous Solution. *J. Phys. Chem. A* **108**, 2733–2739 (2004).

108. Berthet, J. C., Thuéry, P., Dognon, J. P., Guillaneux, D. & Ephritikhine, M. Sterically congested uranyl complexes with seven-coordination of the UO2 unit: The peculiar ligation mode of nitrate in [UO 2(NO3)2(Rbtp)] complexes. *Inorg. Chem.* **47**, 6850–6862 (2008).

109. Kannan, S., Moody, M. A., Barnes, C. L. & Duval, P. B. Lanthanum(III) and uranyl(VI) diglycolamide complexes: Synthetic precursors and structural studies involving nitrate complexation. *Inorg. Chem.* **47**, 4691–4695 (2008).

110. Dendritech Inc. PAMAM Dendrimers. http://www.dendritech.com/pamam.html.

111. Malvern Instruments Ltd. Size theory. *Zetasizer Nano User Man.* **MAN0485**, 250 (2013).

112. Malvern. Whitepaper: Mie theory the first 100 years. 10 (2010).

113. Oda, Y. & Aoshima, A. Ab initio quantum chemical study on charge distribution and molecular structure of uranyl (vi) species with raman frequency. *J. Nucl. Sci. Technol.* **39**, 647–654 (2002).

114. Stetefeld, J., McKenna, S. A. & Patel, T. R. Dynamic light scattering: a practical guide and applications in biomedical sciences. *Biophys. Rev.* **8**, 409–427 (2016).

115. Li, H., Yang, P., Pageni, P. & Tang, C. Recent Advances in Metal-Containing Polymer Hydrogels. *Macromol. Rapid Commun.* **38**, 1700109 (2017).

116. Asandei, A. *et al.* Nanoscale Investigation of Generation 1 PAMAM Dendrimers Interaction with a Protein Nanopore. *Sci. Rep.* **7**, 1–13 (2017).

117. Liu, Y., Bryantsev, V. S., Diallo, M. S. & Goddard, W. A. PAMAM dendrimers undergo pH responsive conformational changes withoutswelling. *J. Am. Chem. Soc.* **131**, 2798–2799 (2009).

118. Lindqvist-Reis, P. *et al.* Structure and spectroscopy of hydrated neptunyl(vi) nitrate complexes. *Dalt. Trans.* **42**, 15275–15279 (2013).

119. Ng, S. *et al.* Neptunium in the fuel cycle: Nonproliferation benefits versus industrial drawbacks. *Nucl. Technol.* **164**, 13–19 (2008).